

Springer Theses

Recognizing Outstanding Ph.D. Research

Weijia Yuan

Second-Generation High-Temperature Superconducting Coils and Their Applications for Energy Storage

 Springer

Springer Theses

Recognizing Outstanding Ph.D. Research

For further volumes:

<http://www.springer.com/series/8790>

Aims and Scope

The series “Springer Theses” brings together a selection of the very best Ph.D. theses from around the world and across the physical sciences. Nominated and endorsed by two recognized specialists, each published volume has been selected for its scientific excellence and the high impact of its contents for the pertinent field of research. For greater accessibility to non-specialists, the published versions include an extended introduction, as well as a foreword by the student’s supervisor explaining the special relevance of the work for the field. As a whole, the series will provide a valuable resource both for newcomers to the research fields described, and for other scientists seeking detailed background information on special questions. Finally, it provides an accredited documentation of the valuable contributions made by today’s younger generation of scientists.

Theses are accepted into the series by invited nomination only and must fulfill all of the following criteria

- They must be written in good English.
- The topic should fall within the confines of Chemistry, Physics and related interdisciplinary fields such as Materials, Nanoscience, Chemical Engineering, Complex Systems and Biophysics.
- The work reported in the thesis must represent a significant scientific advance.
- If the thesis includes previously published material, permission to reproduce this must be gained from the respective copyright holder.
- They must have been examined and passed during the 12 months prior to nomination.
- Each thesis should include a foreword by the supervisor outlining the significance of its content.
- The theses should have a clearly defined structure including an introduction accessible to scientists not expert in that particular field.

Weijia Yuan

Second-Generation High-Temperature Superconducting Coils and Their Applications for Energy Storage

Doctoral Thesis accepted by the
University of Cambridge, Cambridge, UK

Author

Dr. Weijia Yuan
Wolfson College
University of Cambridge
Cambridge Cambridgeshire
UK
e-mail: wy215@cam.ac.uk

Supervisor

Dr. T. A. Coombs
Engineering Department
University of Cambridge
Cambridge
CB3 0FA
UK
e-mail: tac1000@cam.ac.uk

ISSN 2190-5053

ISBN 978-0-85729-741-9

DOI 10.1007/978-0-85729-742-6

Springer London Dordrecht Heidelberg New York

e-ISSN 2190-5061

e-ISBN 978-0-85729-742-6

British Library Cataloguing in Publication Data

A catalogue record for this book is available from the British Library

© Springer-Verlag London Limited 2011

Apart from any fair dealing for the purposes of research or private study, or criticism or review, as permitted under the Copyright, Designs and Patents Act 1988, this publication may only be reproduced, stored or transmitted, in any form or by any means, with the prior permission in writing of the publishers, or in the case of reprographic reproduction in accordance with the terms of licenses issued by the Copyright Licensing Agency. Enquiries concerning reproduction outside those terms should be sent to the publishers.

The use of registered names, trademarks, etc., in this publication does not imply, even in the absence of a specific statement, that such names are exempt from the relevant laws and regulations and therefore free for general use.

The publisher makes no representation, express or implied, with regard to the accuracy of the information contained in this book and cannot accept any legal responsibility or liability for any errors or omissions that may be made.

Cover design: eStudio Calamar, Berlin/Figueres

Printed on acid-free paper

Springer is part of Springer Science+Business Media (www.springer.com)

Parts of this thesis have been published in the following journal articles

1. Weijia Yuan, A. M. Campbell, Z. Hong, M. D. Ainslie and T. A. Coombs, *Comparison of AC losses, magnetic field/current density distribution and critical currents of superconducting circular pancake coils and infinitely long stacks using coated conductors*, Superconductors Science and Technology, **23**(8):085011, 2010
2. Weijia Yuan, A. M. Campbell and T. A. Coombs, *AC losses and field and current density distribution during a full cycle of a stack of superconducting tapes*, Journal of Applied Physics, **107**(9):093909, 2010
3. Weijia Yuan, W. Xian, M. Ainslie, Z. Hong, Y. Yan, R. Pei, Y. Jiang and T. A. Coombs, *Design and test of a Superconducting Magnetic Energy Storage (SMES) coil*, IEEE transaction on applied superconductivity, **20**(3):1379–1382, 2010
4. Weijia Yuan, A. M. Campbell and T. A. Coombs, *A model to calculate the AC loss of second-generation high temperature superconductor pancake coils*, Superconductor Science and Technology, **22**(7):075028, 2009
5. J. Zhu, W. Yuan, T. A. Coombs and Q. Ming, *Simulation and experiment of a YBCO SMES prototype in voltage sag compensation*, Physica C, **471**(3): 199–204, 2011

Supervisor's Foreword

This thesis has introduced a detailed programme of research into optimization and development of Superconducting Magnetic Energy Storage (SMES) using second-generation (2G) high-temperature superconducting tapes. This is a complex, interesting and important area of research.

The first part of the thesis provides an appropriate summary of existing knowledge about magnetic field penetration in superconductors (including the important finite size effects), the techniques for modelling the magnetic properties of superconducting structures of increasing complexity (including stacks and coils), and the performances of SMES technology compared to other forms of energy storage. Next, an efficient algorithm is provided in order to design the geometric parameters of the superconducting coil in view of maximizing the stored energy for a given length of available superconducting tapes.

The main part of the thesis presents an original model for determining the electrical characteristics of the system (losses, amount of energy and critical current) as a function of the parameters of the superconductors. Weijia has developed analytical expressions that extend those developed by Clem et al. An advanced numerical model also allows him to determine the distribution of magnetic flux density and current density over a full AC cycle and to determine the losses therefrom, even for a field-dependent critical current density. Significantly, the results obtained by this model show that the knowledge of the maximum values of the alternating excitation are enough to determine the AC losses of the coil, which reduces considerably the calculation time. The current and magnetic field profiles are presented for various values of the superconducting parameters, and the discussion reflects an excellent understanding of the physics of the system. A detailed comparison of the “infinite stack” and the circular pancake geometries is also carried out. He clearly shows that the infinitely long stack approximation of a pancake coil is adequate in most practical situations.

Next three prototype SMES are built and tested at the liquid nitrogen temperature. The superconducting properties of the coils are measured. A specific cryogenic system based on a cryocooler is then designed in order to operate the pancake coil at lower temperatures.

Finally, Weijia studies an electronic converter for the control of the SMES; this system is tested successfully and demonstrates, both by modelling and by experiment, that the superconducting coil can be used for compensating a voltage sag. In the final chapter, Weijia draws a number of practical conclusions for his investigations. These include a summary of how the performances of a superconducting coil can be optimized. Weijia finally gives an outlook of the research topics that could be developed for a further improvement of the use of SMES with 2G YBCO tapes. The results of this study are particularly relevant to power engineering applications, and a number of key issues are highlighted.

In summary, the research work carried out by Weijia represents a significant contribution to the understanding of 2G superconductors for magnetic energy storage. In his work, Weijia demonstrates the evident knowledge of the engineering and physics skills required for the theoretical and experimental investigation of HTS systems. This research is novel and important for the development of coated conductors for magnetic energy storage applications.

Cambridge, March 2011

Dr. T. A. Coombs

Preface

Since a superconductor has no resistance below a certain temperature and can therefore save a large amount of energy dissipated, it is a “green” material by saving energy loss and hence reducing carbon emissions. Recently the massive manufacture of high-temperature superconducting (HTS) materials has enabled superconductivity to become a preferred candidate to help generate and transport cleaner energy.

One of the most promising applications of superconductors is Superconducting Magnetic Energy Storage (SMES) systems, which are becoming the enabling engine for improving the capacity, efficiency and reliability of the electric system. SMES systems store energy in the magnetic field created by the flow of direct current in a superconducting coil. SMES systems have many advantages compared to other energy storage systems: high cyclic efficiency, fast response time, deep discharge and recharge ability, and a good balance between power density and energy density. Based on these advantages, SMES systems will play an indispensable role in improving power qualities, integrating renewable energy sources and energizing transportation systems.

This thesis describes an intensive study of superconducting pancake coils wound using second-generation (2G) HTS materials and their application in SMES systems. The specific contribution of this thesis includes an innovative design of the SMES system, an easily calculated, but theoretically advanced numerical model to analyse the system, extensive experiments to validate the design and model, and a complete demonstration experiment of the prototype SMES system.

This thesis begins with literature review which includes the introduction of the background theory of superconductivity and development of SMES systems.

Following the literature review is the theoretical work. A prototype SMES system design, which provides the maximum stored energy for a particular length of conductors, has been investigated. Furthermore, a new numerical model, which can predict all necessary operation parameters, including the critical current and AC losses of the system, is presented. This model has been extended to analyse superconducting coils in different situations as well.

To validate the theoretical design and model, several superconducting coils, which are essential parts of the prototype SMES system, together with an experimental measurement setup have been built. The coils have been energized to test their energy storage capability. The operation parameters including the critical current and AC losses have been measured. The results are consistent with the theoretical predictions.

Finally the control system is developed and studied. A power electronics control circuit of the prototype SMES system has been designed and simulated. This control circuit can energize or discharge the SMES system dynamically and robustly. During a voltage sag compensation experiment, this SMES prototype monitored the power system and successfully compensated the voltage sag when required.

By investigating the process of building a complete system from the initial design to the final experiment, the concept of a prototype SMES system using newly available 2G HTS tapes was validated. This prototype SMES system is the first step towards the implementation of future industrial SMES systems with bigger capacities, and the knowledge obtained through this research provides a comprehensive overview of the design of complete SMES systems.

Cambridge, October 2010

Dr. Weijia Yuan

Acknowledgments

It was impossible for me to accomplish this Ph.D. study without the numerous help I received from all kind people around me. I would like to take this opportunity to thank you all, even if you are not personally mentioned here.

First of all, I would like to express my utmost gratitude to my supervisor, Dr. Tim Coombs, for his guidance, suggestions and criticism throughout my study in Cambridge. I learned a lot from his knowledge on superconductivity, presentation skills, innovative ideas and humorous personality. Special thanks to Prof. Archie Campbell for his generous and invaluable help during my study. Without his support I could not imagine finishing my Ph.D. project. I would also like to thank Dr. Mark Husband from Rolls Royce for his great support and advice throughout the project.

I would also like to thank Dr. Ming Qiu, Dr. Jiahui Zhu, Dr. Hongjie Zhang and Dr. Bin Wei from the China Electric Power Research Institute and Dr. Jin Fang and Panpan Chen from Beijing Jiaotong University. Thank you all for your help with the experimental tests. My appreciation also goes to Dr. Darko Bracanovic and Dr. Jeremy Good from Cryogenic Ltd. for providing the test equipment. Special thanks to Prof. John Clem from Ames Laboratory for the very helpful communications on his original simulation model.

I could not finish this dissertation without the help from my colleagues at Cambridge University. I would like to thank my laboratory colleagues, in no particular order, Dr. Anton Velichko, Dr. Roman Viznichenko, Dr. Zhiyong Hong, Dr. Iskandar Samad, Dr. Richard Marchant, Dr. Karthik Tadinada, Dr. Probir Ghoshal, Dr. Jiayi Cao, Dr. Yudong Jiang, Ruilin Pei, Wei Xian, Yu Yan, Quan Li, Paul Bickford, Mark Ainslie, Chia-hao Hsu, Yiran Chen and Min Zhang. I must also thank John Grundy, Antony Dennis, Dr. Yunhua Shi and Zhihan Xu for their help in experimental tests and knowledge on superconductivity.

My gratitude to my very close and kind friends here from my undergraduate university, Tsinghua University and my homeland China. Thank you for sharing your intelligence in general scientific research and very warm and friendly accompany through my Ph.D. study.

Last but definitely not least, the biggest thanks go to my parents who always love me unconditionally, and to all my family members who always support me.

Contents

1	Introduction	1
1.1	Background	1
1.2	Thesis Purpose and Structure	2
	References	4
2	Background of Superconductors	5
2.1	Development of Superconducting Materials and Theory	5
2.2	Modelling of Superconductors	8
2.2.1	Type I and Type II Superconductors	8
2.2.2	Critical State Models	10
2.2.3	Finite Element Method Modelling	15
2.2.4	Modelling of Superconducting Stacks and Coils	18
	References	21
3	Development of SMES Systems	25
3.1	Structure of SMES Systems	25
3.2	History of SMES Technology	27
3.3	Comparison of SMES with Other Energy Storage Systems	30
3.4	Application of SMES Technology	32
3.4.1	Application of SMES Technology in Power Grids	32
3.4.2	Application of SMES Technology in Distributed Power Systems	34
3.4.3	SMES Application for Aircraft Taxiing	34
3.5	Current Problems with SMES Projects	35
	References	36
4	Coil Design	39
4.1	Second Generation High-Temperature Superconductors Tape	39
4.2	Coil Design	43
4.2.1	Optimisation with 12-mm-Width Tape	44
4.2.2	Further Optimisation with 12-mm-Width Tape	45

4.2.3	Optimisation with 4-mm-Width Tape	48
4.2.4	Final SMES Coil Design	50
	Reference	51
5	Modelling of Superconducting Pancake Coil	53
5.1	Clem Model	54
5.2	An Infinitely Long Stack of 2G HTS Tapes	54
5.2.1	Model Assumptions.	54
5.2.2	Solution Methodology for Transport Current Only	56
5.2.3	Extension of Model to Stack in Only Magnetic Field	61
5.2.4	Calculation Examples	62
5.2.5	Discussion	71
5.3	Magnetic Field and Current Density Distribution Over Full AC Cycle.	73
5.3.1	Stack Over Full Cycle With Only AC Transport Current	73
5.3.2	Stack Over Full Cycle With Only AC Applied Fields	78
5.3.3	Configuration of the Pancake Coil	79
5.3.4	Stack With AC Transport Current Only.	79
5.3.5	Stack With AC Applied Field Only.	86
5.3.6	Discussion	89
5.4	Comparison of Infinitely Long Stack and Circular Pancake Coil.	90
5.4.1	Assumptions of the Model	90
5.4.2	Solution Methodology	92
5.4.3	Configuration of the Pancake Coil	93
5.4.4	Solution for Fixed Transport Current.	94
5.4.5	Solution with Different Transport Currents.	96
5.4.6	Effect of Coil Radius.	96
5.5	Conclusions	102
	References	103
6	Coil Tests and Applications for SMES	105
6.1	Superconducting Coils	106
6.1.1	Coil Configurations.	106
6.1.2	Coil Windings	106
6.2	Experimental Rigs and Critical Current Measurements.	109
6.2.1	Experimental Rig	109
6.2.2	Experimental Tests of Coil 1	110
6.2.3	Experimental Tests of Coils 2 and 3	115
6.2.4	Experimental Rig Using a Cryocooler	118
6.3	AC Losses of the Coil	120
6.3.1	Theory and Experiment of AC Losses in Literature	120
6.3.2	Experimental Rig of AC Losses Measurement at 77 K.	124
6.3.3	Measurement Results and Analysis	125

6.4	Control Circuit for SMES Applications	126
6.4.1	Chopper Circuit to Charge and Discharge the Coil	127
6.4.2	Power Electronics Converter	128
6.5	Experiment of Chopper Circuit	128
6.6	Simulation and Experiment of Voltage Sag Compensation	131
6.6.1	System Circuit and Control Strategy	131
6.6.2	Simulation Results	135
6.6.3	Experiment Results	135
	References	137
7	Conclusions	139
7.1	Summary	139
7.2	Possible Improvements	140
7.3	Future Look of SMES	140
	Reference	141
	Appendix A.	143

Chapter 1

Introduction

1.1 Background

The shortage of energy in the world is becoming a bigger and bigger challenge. Nearly 8% of total electricity energy is dissipated during transportation process [1]. Saving electricity and hence energy, as well as reducing carbon emissions, are key priorities for the future.

The introduction of electricity to the public started over one century ago and since then electrical devices and systems have been widely used. However, due to the deterioration and ageing of electrical devices in existing systems, generation and transportation of clean energy is becoming a challenge.

Since superconductors have no resistance below a certain temperature and can therefore save a large amount of energy dissipated in comparison to conventional materials, they are becoming the enabling engine for improving the capacity, efficiency, and reliability of the future electric system. They have the potential for bringing a more fundamental change to electric power technologies than has occurred since the inception of power systems.

The application of superconductors in electrical devices can be divided into two categories. The first group is to replace copper with superconductors in conventional electrical devices, such as superconducting cable, superconducting transformers and superconducting machines; the second group consists of two emerging devices which have no counterparts in conventional electrical devices and have been enabled by superconductors: Superconducting Magnetic Energy Storage (SMES) systems and Superconducting Fault Current Limiters (SFCL).

Compared to conventional electrical devices, the most important advantage of superconducting devices is the significant amount of saved energy. Moreover, they can reduce device dimensions and are more green and safe. For instance, superconducting cables act as ‘energy superhighways’ with a higher capacity while eliminating resistive losses. Thus, the superconducting transmission and distribution system would allow more electricity to reach consumers with no increase in

fossil fuel-related CO₂ emissions, using smaller sized equipment. It is estimated that 40% of USs total grid energy losses are from aging conventional transformers and that the use of superconducting transformers could reduce energy losses on the grid by one-third—equivalent to eliminating about 15 million tons of CO₂ annually [2]. Furthermore, they are cooled by liquid nitrogen as opposed to flammable and toxic oil coolants used in conventional transformers. Superconducting machines are more compact and efficient than conventional ones since superconductors can carry a large current or produce a large magnetic field with only a small device dimension. An SFCL is able to protect electric grid equipment from damage and thus reduce the cost for utilities.

SMES systems are efficient devices of storing large electrical energy. The superconducting coil in a SMES device has an almost completely lossless current path and is very compact. Compared to other equivalent energy storage systems, SMES systems have the following advantages:

- More environmentally friendly since they do not have any toxic chemical materials
- A higher cyclic efficiency since they have no resistance during DC conditions
- Respond more quickly since the energy conversion only involve with electrical but no mechanical or hydraulic devices
- A deeper discharge and recharge ability since the superconductors can be completely discharged and recharged
- A better balance between power density and energy density

SMES devices are playing an important role in the expansion and modernization of the transmission system infrastructure, as well as the integration of renewable energy sources. With its stored energy and fast response capability, a SMES system can protect the electrical grid from faults, which might include voltage fluctuations that crash digital electronics, brownouts that disable industrial processes and harm electrical equipment, and power failures like the North American blackout in 2003 that affected 50 million people and caused approximately \$6 billion in economic damage which lasted for 4 days [3]. Furthermore, renewable energy sources, such as wind power, solar plant and tidal generators, have very unstable output power. By connecting with renewable energy sources, SMES systems will smooth their output power and ensure a safe and reliable flow of power for consumers.

1.2 Thesis Purpose and Structure

The biggest difficulty in achieving the widespread application of superconductivity is the extremely low temperature. However, the discovery of high-temperature superconductivity in 1986 has brought superconductor much closer to real industry application. High-temperature superconductors (HTS) materials are superconducting at 77 K using easily-accessible liquid nitrogen as the coolant, whereas

low-temperature superconductors (LTS) material usually work at 4.2 K and requires liquid helium which is much more difficult and expensive to obtain.

More than 20 years have past since then, and now long lengths of second-generation high-temperature superconductors (2G HTS) have become commercially available. Researchers are using them to wind superconducting pancake coils which can be used in a large range of applications, such as superconducting machines, SFCLs, Magnetic Resonance Imaging (MRI), SMES and so on.

However, before the real application of 2G superconducting coils, several problems need to be investigated. A comprehensive simulation model has to be created to simulate the superconducting coils. This model would accurately predict how much current can be put into the superconducting coils, and this is one of the priorities. Using this model to calculate AC losses during the charge and discharge process is also very important. Although a superconductor has no losses during DC conditions, it does have a certain amount of loss during AC conditions. More fundamentally, how the magnetic field and current density distribution within the coil changes during an AC cycle need to be understood.

When superconducting coils are used in a SMES system, some additional factors need to be considered. The coils need to be designed in an efficient way to give the maximum stored energy possible. Methods to control the input and output of the coil energy also need to be studied.

Finally, the coils need to be experimentally tested. All the crucial parameters for operations of the coils including the critical current, AC losses, magnetic field distribution need to be measured to validate the theoretical model. The coils will also be charged and discharged in an voltage sag compensation experiment thus the control strategy can be validated.

This thesis will investigate all the aforementioned problems in superconducting coils, aiming to discover an engineering application for them in a SMES system. The detailed structure of this thesis is as follows:

Chapter 2 introduces the development of superconductors and their background theories, followed by previous modelling work on superconductors.

Chapter 3 provides an introduction to SMES applications and its developmental history. It also itemises the difficulties in 2G HTS SMES systems and introduces how they are investigated in this thesis.

Chapter 4 presents the characteristics of the superconducting tape performance in background fields with different angles. Studies of different designs are presented and the best design, which can give the maximum stored energy of the system based on a certain length of conductor, is selected.

Chapter 5 introduces a new numerical model. This model is easier to calculate and faster to compute compared with other models, and it maintains consistency with superconductivity theory. This numerical model can calculate the critical current and AC losses of a superconducting coil, which is the essential component of a SMES system.

Chapter 6 provides experimental test data for the superconducting coils. An experiment rig and data acquisition system was built. The tests, including the critical current measurement and the AC losses measurement, validate the model

in Chap. 5. A control circuit design for a SMES unit is also presented. This circuit can put the SMES unit into two different modes: charge and discharge modes. The superconducting coil has been tested with the control circuit and it successfully compensated a voltage sag in a power system.

Chapter 7 summarises the work and discusses the problems to be solved and potential applications of SMES systems for industrial use in future.

References

1. Hassenzahl WV, Hazelton DW, Johnson BK, Komarek P, Noe M, Reis CT (2004) Electric power applications of superconductivity. *Proc IEEE* 92(10):1655–1674
2. Superpower Inc. Energy efficiency in the power grid. online, <http://www.superpower-inc.com/content/superpower-partners-waukesha-build-sfcl-transformer-u-s-doe-energy-smart-grid-demonstration->
3. Lynne K (2004) The north American blackout and electricity policy: alternatives to transmission construction. *Econ Aff* 24(1)

Chapter 2

Background of Superconductors

2.1 Development of Superconducting Materials and Theory

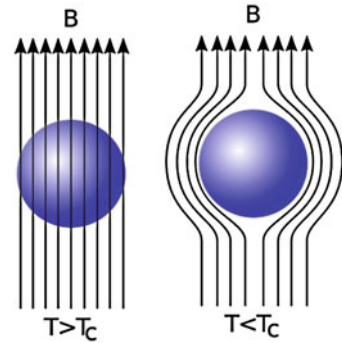
Superconductivity was discovered in 1911 by Kamerlingh Onnes. It was observed that the resistance of the solid mercury abruptly disappeared at the temperature of 4.2 K [1]. In subsequent decades, superconductivity was found in several other materials, most of which are metals. Lead was found to be superconducting at 7 K in 1913, and niobium nitride was found to be superconducting at 16 K in 1941.

Ever since its discovery, scientists have been working to find physical theories explaining this superconductivity phenomenon. A milestone in understanding superconductivity came in 1933 when Meissner and Ochsenfeld discovered that superconductors completely expelled applied magnetic fields, a phenomenon known as the Meissner effect [2]. Figure 2.1 gives the diagram of Meissner effect [3]. When the temperature is below the critical temperature T_c , the superconductor will expel all magnetic field from within it.

The London model was proposed in 1935, which showed that the Meissner effect was a consequence of the minimization of the electromagnetic free energy carried by superconducting current. To maintain the superconductor in the Meissner effect, there is a superconducting current flowing within very small penetration depth, which is negligible to the superconductor thickness [4].

Landau and Ginzburg suggested a mathematical theory to model superconductivity. It describes some of the phenomena of superconductivity without explaining the underlying microscopic mechanism with the help of general thermodynamic arguments [5]. Using this so-called Ginzburg-Landau theory, Abrikosov successfully predicted the division of superconductors into the two categories now referred to as Type I and Type II superconductors which are introduced in Sect. 2.2.1 [6].

The first complete microscopic theory of superconductivity was proposed by Bardeen, Cooper and Schrieffer. According to BCS theory, the superconducting current is carried by a pair of electrons known as Cooper pairs. The Cooper pair is

Fig. 2.1 Meissner effect

more stable than a single electron within the lattice, since the Cooper pair is more resistant to vibrations within the lattice as the attraction to its partner will keep it stable among the lattice it experiences less resistance. Therefore, Cooper pairs move through the lattice relatively unaffected by thermal vibrations (electron-phonon interactions) below the critical temperature [7, 8, 9]. BCS theory turned out to be of great success as it correctly predicted the dependence of the value of the energy gap E at temperature T on the critical temperature T_c and Meissner effect.

Although superconductors were found in 1911, it is until fifty years later that the superconducting wires were successfully manufactured for a large scale application. All the early superconductors are metals, which means they are all Type I superconductors. The reason why Type I superconductor cannot be used for a large scale application is that it immediately loses superconductivity when carrying a small current or exposed to a small magnetic field. In contrast, Type II superconductor can be used on a large scale application since it still maintains superconductivity with a bigger transport current or in a bigger magnetic field. In 1960s, the first commercial superconducting wire, a niobium-titanium (NbTi) alloy and niobium-tin (Nb_3Sn) alloy, was developed by researchers, allowing the construction of the first practical superconducting magnets [10]. The critical temperature of NbTi is 10 K and can remain superconducting until about 15 T. Nb_3Sn is more expensive than NbTi, but can withstand magnetic field intensity values up to 30 T. Its critical temperature is 18.3 K which is also higher than NbTi. However, Nb_3Sn is much more expensive and hard to use than NbTi.

Everything seemed to be settled in the superconductivity area. BCS theory explains the mechanism of superconductivity, whereas NbTi and Nb_3Sn is manufactured for engineering application. According to BCS theory, 30 K was thought to be the highest theoretically possible critical temperature. However, the appearance of high-temperature superconductivity (HTS) breaks up the harmony. The first high-temperature superconductor were discovered to become superconducting at 35 K in 1986 by IBM Researchers Karl Müller and Johannes Bednorz [11]. Then Yttrium barium copper oxide (YBCO) and Bismuth strontium calcium copper oxide BSCCO was found to become superconducting at 93 K and 105 K, respectively [11, 12, 13]. The family of high-temperature superconductors are all

cuprate superconductors. Cuprate indicates a copper compound involved in a larger coordination complex has an overall negative charge. Cuprate superconductors are generally considered to be quasi-two-dimensional materials with their superconducting properties determined by electrons moving within weakly coupled copper-oxide (CuO_2) layers.

The discovery of HTS materials has brought the superconductivity much closer to industrial applications. One benefit is that the higher critical temperature of HTS materials is above the boiling point of liquid nitrogen, which is much more accessible and cheaper as opposed to liquid helium for LTS materials. The other advantage is that they also have a higher critical magnetic field (and critical current density) at which superconductivity is destroyed. In large scale applications the high critical magnetic field and upper critical temperature are very valuable.

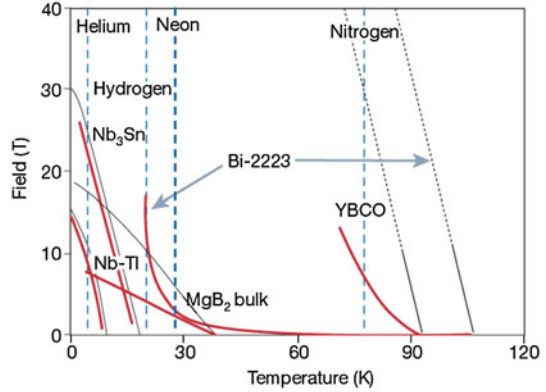
BSCCO was the first high-temperature superconductor to be used for making superconducting wires. These materials have come to be known as first generation high-temperature superconductors (1G HTS). It has two different types, BSCCO-2212 ($\text{Bi}_2\text{Sr}_2\text{Ca}_1\text{Cu}_2\text{O}_8$) and BSCCO-2223 ($\text{Bi}_2\text{Sr}_2\text{Ca}_2\text{Cu}_3\text{O}_{10}$), very often they are referred to simply Bi2212 and Bi2223. BSCCO needs to be hole doped by cation substitution or an excess of oxygen atoms in order to become superconducting. This is usually done by adding interstitial oxygen atoms to the copper oxide plane. Both Bi2212 and Bi2223 can be made into wires via the powder-in-tube process.

More recently, rare earth-based HTS material ((RE)BCO) have been developed. Rare earth elements include, but are not limited to, Yttrium, Samarium and Gadolinium. These materials are known as second-generation high-temperature superconductors. Among the all 2G HTS materials, the most famous and already industrially manufactured one is Yttrium barium copper oxide (YBCO), which is a crystalline chemical compound with the formula $\text{YBa}_2\text{Cu}_3\text{O}_7$ [14, 15]. A problem limiting the use of this material is the difficulty in making it into wires. Oxide materials such as this are brittle, and forming them into wires by any conventional process does not produce a strong enough superconductor. Unlike BSCCO, the powder-in-tube process does not give good results with YBCO. The most popular method developed to utilize this material involves deposition of YBCO on flexible metal tapes coated with buffering metal oxides which is known as coated conductor. There are now two commonly used process, Rolling Assisted Biaxially Textured Substrates (RABITs) process and the Ion-Beam-Assisted Deposition (IBAD) process. Companies such as American Superconductor, Superpower, Sumitomo, Fujikura, Nexans Superconductors, and European Advanced Superconductors, are now routinely manufacturing these 2G HTS tapes.

More than twenty years have passed since the discovery of the first HTS material, there are intensive experimental and theoretical research on these materials; however, there is still no convincing theory to explain their properties.

In 2001 Nagamatsu et al found the superconductivity in Magnesium diboride (MgB_2) at 39 K [16]. This is the highest temperature amongst conventional superconductors. This discovery caused great excitement since MgB_2 is a simple ionic binary compound that has proven to be an inexpensive material.

Fig. 2.2 Comparison of critical magnetic fields of different superconducting materials at different temperatures. The upper critical field H_{c2} at which bulk superconductivity is destroyed is indicated in black, while the irreversibility field H^* at which the bulk critical current density goes to zero is indicated in red [3]



In 2008 iron-based superconductors were found to have superconducting properties [17, 18]. This is currently the material with the second highest critical temperature, behind the cuprates. Much of the interest is because the new compounds are very different from the cuprates and may help lead to a theory of non-BCS-theory superconductivity.

Figure 2.2 gives the comparison of the critical magnetic fields of different superconducting materials at different temperatures [3]. The blue dashed lines are the boiling points. We can find that HTS materials have significantly larger critical magnetic fields and temperatures than LTS materials.

2.2 Modelling of Superconductors

2.2.1 Type I and Type II Superconductors

Superconductor will lose its superconductivity when the applied field is too large, i.e. Meissner effect breaks down. According to how this breakdown occurs, superconductors can be divided into two classes, Type I and Type II. In Type I superconductors, superconductivity is abruptly destroyed when the strength of the applied field rises above a critical value H_c . All the early found metal superconductors are typical Type I superconductors, such as aluminium and lead.

Equation 2.1 links the magnetic field H , magnetic flux density B , the magnetisation of the material M , and the permeability of free space μ_0 .

$$B = \mu_0(H + M) \quad (2.1)$$

Figure 2.3 illustrates the magnetisation process of a type I superconductor [50]. When the applied field H is smaller than H_c , M is equal to $-H$, thus the total magnetic field in the superconductor B is zero. However, immediately after H is bigger than H_c , M drops to zero and the superconductor is in the normal state.

Fig. 2.3 Magnetisation of Type I superconductors

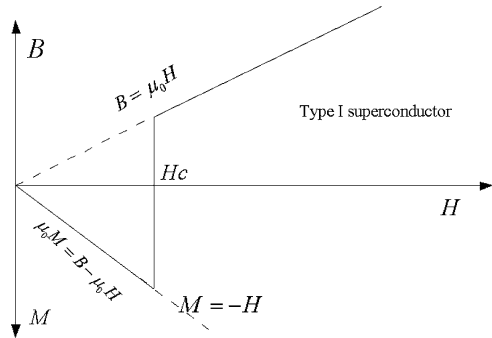
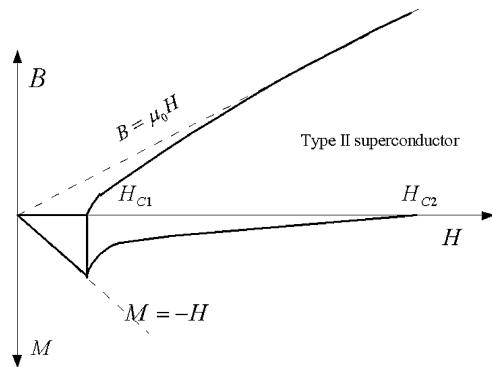


Fig. 2.4 Magnetisation of Type II superconductors

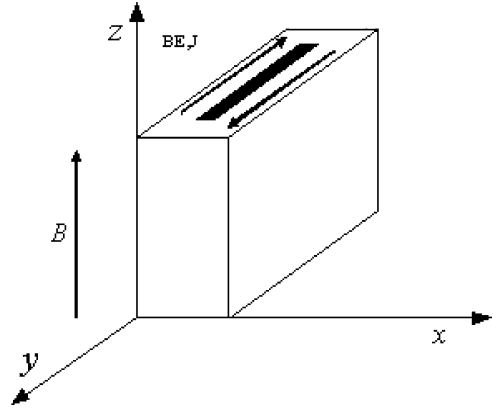


A Type II superconductor will gradually lose its superconductivity when the applied field increase, this is featured by a gradual transition from the superconducting to the normal state within an increasing magnetic field. In comparison to a Type I superconductor, a Type II superconductor has two critical magnetic fields, the lower critical magnetic field H_{c1} and the higher critical magnetic field H_{c2} . When the external field is larger than H_{c1} , it is no longer completely expelled from the superconductor but exists in a mixed state. Only when the applied field is larger than H_{c2} , the superconductivity will be completely destroyed and the material will exist in a normal state. Also there are two critical temperatures, T_{c1} and T_{c2} . The superconductor will gradually lose its superconductivity between critical temperatures T_{c1} and T_{c2} .

Figure 2.4 shows the graduate transition from the superconducting state to the normal state. When the applied field H is smaller than H_{c1} , the magnetic field is completely expelled from the superconductor with $M = -H$; when the applied field is between H_{c1} and H_{c2} , the superconductor will partly expel the magnetic field with M gradually dropping to zero. Only when the applied field is larger than H_{c2} , the superconductor exists in the normal state.

Typically Type II superconductors have higher critical temperatures and critical magnetic fields than Type-I superconductors. This allows them to conduct higher currents and makes them useful for large scale applications.

Fig. 2.5 Infinite slab in a uniform field parallel to surface



2.2.2 Critical State Models

The critical state model for superconductors are concentrated on macroscopic properties of the material. They are based on the experimental observations of the relationship between the current density and the magnetic field. For the large scale applications of superconductivity, engineers are more interested in the macroscopic properties such as the current and the magnetic field, rather than the microscopic behaviour inside the superconductor. Therefore the critical state models are very important in the large scale application of superconductors.

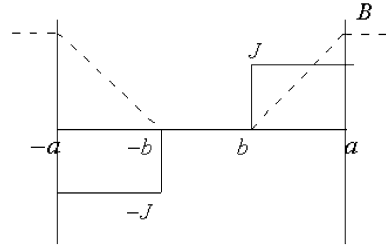
The critical state model suggests when a superconductor carries a small current or is exposed to a small applied field, the outer layer of the superconductor is in a critical state, which means the current density is defined by a critical value. The interior of the superconductor is shielded from the applied field or current.

For a type II superconductor, the applied field begins to penetrate into the superconductor when it is larger than H_{c1} . When entering into the superconductor, the magnetic field becomes superconducting electron current vortices. Each of these vortices carries the same amount of magnetic flux. The Lorentz force pushes the vortices to move, whereas they are also trapped at defects in the crystal lattice of the material. This is known as flux pinning. As a result, the distribution of the vortices is determined by the balance of Lorentz force and pinning force. The depth where the vortices can penetrate depends on the magnitude of the applied field. The surface layer that the vortices occupy is in the so-called critical state. The interior of the superconductor is left without flux and current.

2.2.2.1 Bean Model

Bean model is a widely used critical state model [19]. To simplify the problem, Bean considers an infinitely long slab as shown in Fig. 2.5. Since this slab is very

Fig. 2.6 Current density and magnetic field distribution of a slab exposed to a field by Bean model



thin, only the magnetic field component which is parallel to the slab surface needs to be considered. Since there is only z -direction field, the induced current flows in a circular path along the surface of the slab as shown in Fig. 2.6 and 2.7. The assumption of Bean model is that the change of electric field will induce a constant current density J_c . Therefore we can use the following equations to describe the slab,

$$J(x) = \pm J_c \quad \text{if } |E(x)| \neq 0 \quad (2.2)$$

$$J(x) = 0 \quad \text{if } |E(x)| = 0 \quad (2.3)$$

The Faraday law will simplify to Equation (2.4) below in this slab case,

$$dB/dx = \mu_0 J(x) \quad (2.4)$$

This equation tells us that the magnetic field will linearly decrease to zero until the critical current disappears along the slab width direction. Figure 2.6 illustrates this.

When the external field starts to change in the other direction, there will be an opposite induced current from the surface. With the external field decreasing further, the opposite induced current penetrates further until the slab is fully penetrated.

2.2.2.2 Kim Model

Kim et al proposed a model which allowed the current density in the critical state vary with the local magnetic field [20, 21],

$$\alpha/J = B_0 + B \quad (2.5)$$

The empirical relation describing α is,

$$\alpha = (1/d)(a - bT) \quad (2.6)$$

The constants a and b appear to satisfy $a/b \leq T_c$, while d will depend strongly on the physical micro-structure of the material.

When T is constant, Equation 2.5 reduces to,

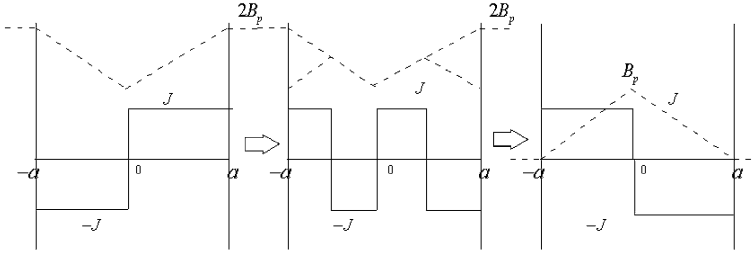


Fig. 2.7 Current density and magnetic field distribution of a slab exposed to a decreasing field by Bean model

$$J_c(B) = J_{c0}(T) \frac{1}{1 + B/B_0} \quad (2.7)$$

where B_0 is a constant depending on the material and $J_{c0}(T) = \alpha(T)/B_0$.

Kim model is quite useful in engineering applications since the magnetic field varies a lot from the surface to the centre of a superconductor, especially for the 2G HTS tapes which has a thin-strip configuration.

2.2.2.3 $E - J$ Power Law

Bean model assumes there is a step relation between the current and the electric field in the superconductor. in 1962 Anderson introduced the flux creep theory indicating that this relation is continuous [22]. Rhyner proposed a formula describing the relation between the current density and the electric field qualitatively [23],

$$E = E_0 \left(\frac{J}{J_0} \right)^n \quad (2.8)$$

where n is one of the material properties and $E_0 = 1 \mu\text{V cm}^{-1}$. J_0 is the critical current density at $E = E_0$.

For LTS type II superconductors n is usually larger than 40, whereas for HTS materials n is usually between 20–30. When n is infinite, $E - J$ power law becomes equivalent to Bean model. Figure 2.8 gives the comparison of different n values. n value is an important parameter for the HTS materials performance.

2.2.2.4 Superconducting Strip Model

A thin strip is a common configuration for HTS coated conductors, thus it received great interest in theoretical and experimental studies. 2G HTS tapes have this typical thin strip configuration. Both Brandt et al. and Zeldov et al. have

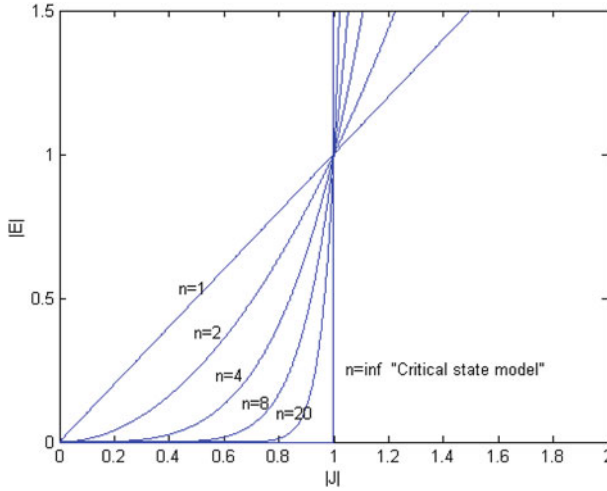


Fig. 2.8 $E - J$ power law with different n values

theoretically analysed the critical state behavior of an infinitely long type II superconducting thin strip [24, 25]. There are significant differences between the thin strip and the aforementioned Bean slab.

In the thin strip exposed to an applied field H_a perpendicular to the wide face (y -direction), a constant critical current density J_c is assumed. When the applied field is not too large the strip is in the Meissner state. The perpendicular magnetic field is completely shielded from the strip by the screening current $J(y)$ which exists in $b < |y| < a$, where a is the half strip width. The part where $|y| \leq b$ remains in Meissner state. Flux penetrates from the edges such that $H(y) = 0$ for $|y| \leq b$, $|J(y)| < J_c$ for $|y| < b$ (shielding currents), and $|J(y)| = J_c$ for $b < |y| < a$. This leads to the following solution,

$$\begin{aligned} J(y) &= \frac{2J_c}{\pi} \arctan \frac{cy}{\sqrt{b^2 - y^2}} \quad \text{for } |y| < b \\ &= J_c y / |y| \quad \text{for } b < |y| < a \end{aligned} \quad (2.9)$$

where b is the penetration depth and is given by

$$b = \frac{a}{\cosh(H_a/H_c)} \quad (2.10)$$

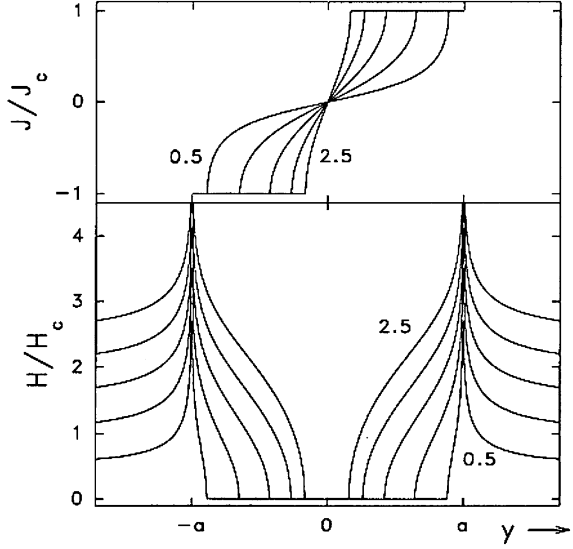
c is defined as

$$c = (a^2 - b^2)^{1/2} / a = \tanh(H_a/H_c) \quad (2.11)$$

H_c is defined as

$$H_c = J_c / \pi \quad (2.12)$$

Fig. 2.9 Current density and magnetic field in a superconducting strip of width $2a$ in a perpendicular field H_a increasing from zero. The depicted profiles are for $H_a/H_c = 0.5, 1, 1.5, 2$ and 2.5



The magnetic field strength along the tape is

$$\begin{aligned}
 H(y) &= 0 & \text{for } |y| < b \\
 &= H_c \operatorname{arctanh} \frac{\sqrt{y^2 - b^2}}{c|y|} & \text{for } b < |y| < a \\
 &= H_c \operatorname{arctanh} \frac{c|y|}{\sqrt{y^2 - b^2}} & \text{for } |y| > a
 \end{aligned} \tag{2.13}$$

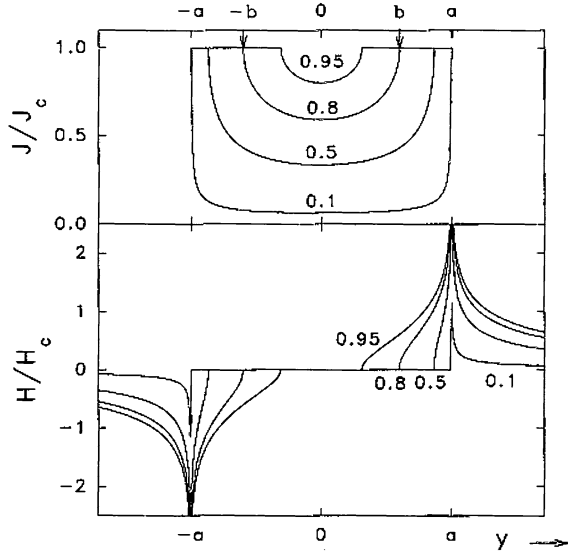
where H_c is the characteristic field, given by $H_c = J_c d / \pi$.

These results are significantly different from the Bean model for a slab: The flux penetration initially is quadratic in H but in Bean model it is linear; the penetrating flux front has vertical slope but in Bean model it has a constant finite; when the flux has partly penetrated and a critical state with $J = J_c$ is established near the edges of the strip, the current flow over the entire width of the strip to shield the central flux-free region, but in Bean model the flux-free region is also current free; the screening current density is a continuous function with a vertical slope at the flux front where it reaches J_c , but in Bean model it is a piecewise constant. Figure 2.9 shows the magnetic field and current density distribution [24, 25].

When a superconducting strip is carrying a transport current. The equations for J and H would be

$$\begin{aligned}
 J(y) &= \frac{2J_c}{\pi} \arctan \left(\frac{a^2 - b^2}{b^2 - y^2} \right)^{1/2} & \text{for } |y| < b \\
 &= J_c & \text{for } b < |y| < a
 \end{aligned} \tag{2.14}$$

Fig. 2.10 Current density and magnetic field in a superconducting strip of width $2a$ carrying a transport current increasing from zero. The depicted profiles are for $I/I_{max} = 0.1, 0.5, 0.8$ and 0.95



where

$$I = 2J_c(a^2 - b^2)^{1/2} \quad (2.15)$$

$$b = a(1 - I^2/I_{max}^2)^{1/2} \quad (2.16)$$

$I_{max} = 2aJ_c$ is the maximum total current occurring at full penetration $b = 0$. Then we can get the magnetic field component perpendicular to the strip,

$$\begin{aligned} H(y) &= 0 & \text{for } |y| < b \\ &= \frac{H_c y}{|y|} \operatorname{arctanh} \left[\frac{y^2 - b^2}{a^2 - b^2} \right]^{1/2} & \text{for } b < |y| < a \\ &= \frac{H_c y}{|y|} \operatorname{arctanh} \left[\frac{a^2 - b^2}{y^2 - b^2} \right]^{1/2} & \text{for } |y| > a \end{aligned}$$

where H_c is the characteristic field, given by $H_c = J_c d / \pi$.

Figure 2.10 gives the current density and magnetic field in a superconducting strip of width $2a$ carrying a transport current I which is increased from zero to $0.95I_c$.

There are also a number modelling of small numbers of superconducting tapes placed either in a stack or parallel [26, 27].

2.2.3 Finite Element Method Modelling

The finite element method (FEM) is a numerical technique for finding approximate solutions of partial differential equations (PDE) as well as of integral equations.

The solution approach is either rendering the PDE into an approximating system of ordinary differential equations, which are then numerically integrated using standard techniques, or eliminating the differential equation completely.

The FEM method originated from the needs of solving complex elastic, structural analysis problems in civil and aeronautical engineering. It was first developed by Hrennikoff and Courant [28].

The FEM method can also be used to solve Maxwell equations for superconducting materials. After solving Maxwell equations, the magnetic field and current density distribution in the superconducting material can be obtained. The FEM methods solving superconductors can be classified into three categories by the equations: $A - V$ formulations, $T - \Omega$ formulations and H formulations.

$A - V$ formulations are derived from Maxwell's equation by introducing magnetic vector potential A as the state variable, which is coupled with $E - J$ power law [29, 30]. After derivation, the final equations are,

$$E = -\frac{\partial A}{\partial t} - \nabla V \quad (2.17)$$

$$-\frac{1}{\mu_0} \nabla^2 A = J \quad (2.18)$$

$$E = E_0 \times \left(\frac{J}{J_0} \right)^n \quad (2.19)$$

In this model the sample starts with no current flowing. Elements carrying J_c are then inserted at the point of maximum vector potential and the field recalculated. The process is continued until the external field is screened from the interior.

$T - \Omega$ formulations use the electric current vector potential T and magnetic scalar potential Ω . Amemiya et al. proposed to use $E - J$ power law to link the equations [31, 32],

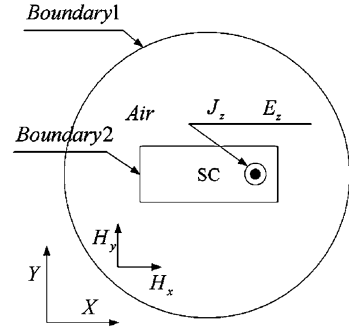
$$\nabla \times \left(\frac{1}{\sigma} \nabla \times T \right) = -\mu \frac{\partial}{\partial t} (H_0 + T - \nabla \Omega) \quad (2.20)$$

$$\nabla \cdot \mu \frac{\partial}{\partial t} (H_0 + T - \nabla \Omega) = 0 \quad (2.21)$$

$$\sigma = \frac{J_0^n}{E_0} (\nabla \times T)^{1-n} \quad (2.22)$$

In Amemiya's papers, he calculated the current distributions in non-twisted and twisted superconducting tapes carrying their transport current and/or exposed to the external magnetic field. The current distribution in a short piece of superconducting tape exposed to AC magnetic field is also calculated. An experimental set-up was built to the measurement of transport loss, magnetisation loss, and the total loss in Bi-2223 tape carrying AC transport current in AC magnetic field were calculated numerically. The measured transport and magnetisation losses almost agree with the theoretical predictions by $T - \Omega$ model.

Fig. 2.11 Subdomains and boundaries in a two-dimensional infinite superconductor



H formulations are to couple the magnetic field equations with $E - J$ power law [33, 34, 35, 36]. Figure 2.11 presents the cross section view in $x-y$ plane of a infinite superconductor. Since the rectangle superconductor is infinite in z direction, this model can be simplified to a two dimensional problem.

According to Faraday's law, we have,

$$\nabla \times \mathbf{E} = -\frac{\partial \mathbf{B}}{\partial t} = -\mu_0 \mu_r \frac{\partial \mathbf{H}}{\partial t} \quad (2.23)$$

Ampere's law gives,

$$\nabla \times \mathbf{H} = \mathbf{J} \quad (2.24)$$

In this two dimensional problem, Equation 2.25 reduces to,

$$J_z = \frac{\partial H_y}{\partial x} - \frac{\partial H_x}{\partial y} \quad (2.25)$$

In the superconductor region, the $E - J$ power law is expressed as,

$$E_{sc_z} = E_0 \left(\frac{J_{sc_z}}{J_c} \right)^n \quad (2.26)$$

where J_{sc_z} and E_{sc_z} is the current density and electric field in the superconductor, respectively. J_c is defined as a standard criterion, which is $1 \mu\text{V} \cdot \text{cm}^{-1}$.

By combining Equation 2.25 and 2.8, we can get two coupled equations to describe the superconductor region:

Thus in the superconductor region,

$$d \left(E_0 \left(\frac{\frac{dH_y}{dx} - \frac{dH_x}{dy}}{J_c} \right)^n \right) / dy = -\mu_0 \mu_r \frac{dH_x}{dt} \quad (2.27)$$

$$-d \left(E_0 \left(\frac{\frac{dH_y}{dx} - \frac{dH_x}{dy}}{J_c} \right)^n \right) / dx = -\mu_0 \mu_r \frac{dH_y}{dt} \quad (2.28)$$

In the non-superconducting region, a linear ohm's law, $E = \rho J$, is used instead of the nonlinear E – J power law, where ρ is the resistivity of air. The coupled equations for the non-superconducting region are,

$$d \left(\rho \left(\frac{dH_y}{dx} - \frac{dH_x}{dy} \right) \right) / dy = -\mu_0 \mu_r \frac{dH_x}{dt} \quad (2.29)$$

$$-d \left(\rho \left(\frac{dH_y}{dx} - \frac{dH_x}{dy} \right) \right) / dx = -\mu_0 \mu_r \frac{dH_y}{dt} \quad (2.30)$$

By solving Equation 2.27 to 2.30, we can calculate the magnetic field and current density distribution in the whole space.

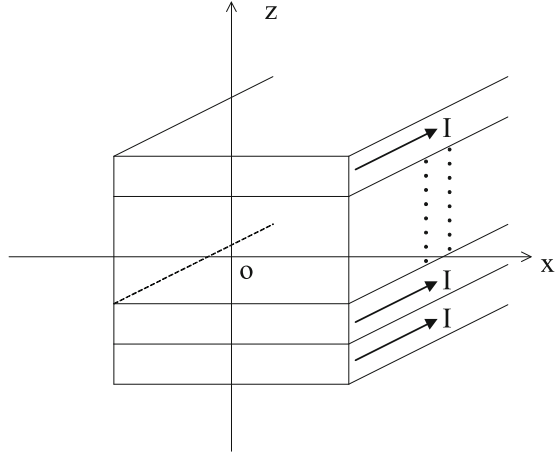
2.2.4 Modelling of Superconducting Stacks and Coils

Only in recent years have long-length coated conductors become commercially available. This makes it possible to wind pancake coils for large scale applications, e.g. Superconducting Magnetic Energy Storage (SMES), Superconducting Fault Current Limiter (SFCL), MRI, etc [37, 38]. Therefore an understanding of magnetic field and current density distribution, and the ability to predict AC losses and critical currents of the coated conductor coils are necessary before designing these devices. Since superconducting pancake coils are only recently available, there are limited research papers on this topic to date. However, analysing superconducting pancake coils is becoming a popular topic due to its importance in application of 2G HTS tapes.

If the coil radius is much larger than the tape width, the coil can be approximated as a stack of superconducting tapes, which will be much easier to compute. Thus in many models, a finite stack of superconducting tapes are used to replace a superconducting coil.

Clem et al. has proposed to use an anisotropic homogeneous-medium approximation to model the pancake coils [39]. In his model Clem has assumed the current density is distributed all across the conductor area such as the engineering current density. The pancake coil is approximated as an infinitely long stack of tapes. These tapes are electrically insulated from each other and each tape carries the same transport current. This differs from a solid with the mean properties of the stack in that firstly there is a significant field penetrating parallel to the tapes, and secondly that the mean current density is uniform in the direction normal to the tapes if averaged across the tapes. In these circumstances we can define two regions. The outer edges will be penetrated by the field and carry the critical current density. The central region will carry a lower current density. In this central region the tapes have not been penetrated by the magnetic field. The critical state and constant critical current density are assumed in the model. Figure 2.12 shows how this approximation is made.

Fig. 2.12 Infinitely long stack of tapes carrying the same current



By searching for the critical boundaries which can minimise the perpendicular magnetic field in the sub-critical region, a solution is obtained. After a solution is obtained, a simple equation 2.31 is used to calculate the AC losses. This equation based on the force on the flux lines as they move in was firstly proposed by Claassen [40].

$$Q_0 = 2J_c \int_{c(z)}^a \int_{-b}^b |B_{z-peak}|(a-x)dx dz \quad (2.31)$$

Claassen's paper shows that when J_c is constant Equation 2.31 is equivalent to the integration of $E \cdot J_c$ [39, 40].

FEM modelling has also been used in studying superconducting pancake coils [41, 42, 43]. These models compute the electromagnetic quantities by coupling the non-linear $E - J$ power law equation with Maxwell equations. Grilli et al. are using an edge-element method to model the superconducting coil by FEM methods. An axis-symmetric model is used to reduce the number of mesh nodes and, consequently, the computation time. The superconducting film in the tapes is very thin (a few micrometres) and its aspect ratio (width/thickness) is very high, typically between 1000 and 10000. This increases the number of nodes and the computation time considerably. As far as the aspect ratio is concerned, they utilized a thickness of 100 μm , with reduced J_c such that the critical current of the tape (330 A) is preserved. They found that this does not significantly affect the AC loss computation in a single tape, because the physics is governed by the sheet transport capacity, i.e. the critical current per unit width, and not much by the actual thickness of the tape. Figure 2.13 shows the the configuration of the coil modelling.

Brambilla et al. are applying the integral equation method to stacks and windings [43, 44]. Due to the high aspect ratio of HTS tapes and the large number of mesh nodes in the geometry, an unacceptably long computation time is needed

Fig. 2.13 FEM modelling of a superconducting coil

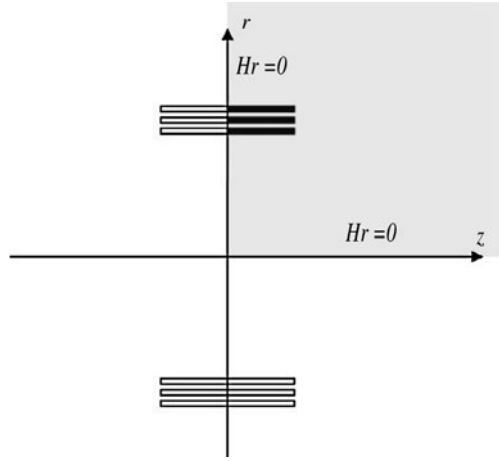
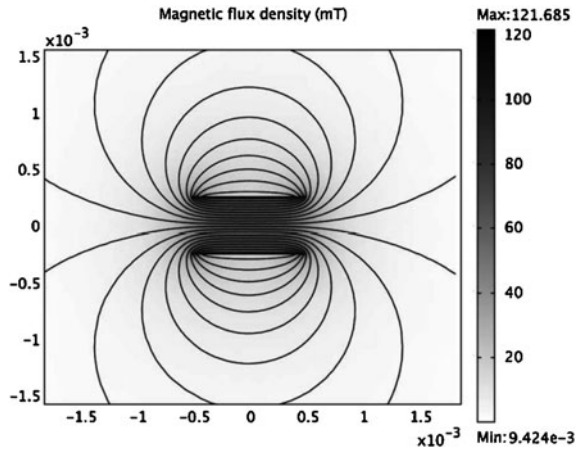


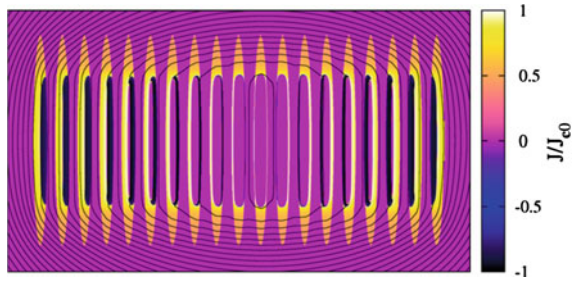
Fig. 2.14 1D FEM modelling of a superconducting coil



if multiple tapes and coils are considered. They developed an integral equation (IE) model that considers the sections of the conductors as 1D objects, in this way eliminating the problem of meshing their interior. The power law is used in the integral equation to link the electric field E and current density J . This method is much faster than the traditional 2D FEM method. Figure 2.14 presents one solution example of the model.

Pardo et al. presented another numerical model to analyse superconducting pancake coils [45, 46]. This model assumes the critical state model with a constant critical current density. The current distribution is calculated by means of the minimum magnetic energy variation (MMEV) method. The real thickness of the conductor and the magnetic interaction between the turns has been taken into account. Figure 2.15 shows the current distribution in his coil.

Fig. 2.15 Model of a superconducting coil using MMEV method



There are also a number of researchers trying to tackle this problem analytically [47, 48, 49]. Although the practical problem needs to be simplified to be adapted for analytical calculations, the analytical methods can usually calculate much faster than the other techniques and provide a good comparison to both numerical methods and experimental results.

References

1. Onnes HK (1911) The resistance of pure mercury at helium temperatures. *Commun Phys Lab Univ. Leiden* 12
2. Ochsenfeld R, Meissner W (1933) Ein neuer effekt bei eintritt der supraleitfähigkeit. *Naturwissenschaften* 21:787–788, 1933-11-01
3. Larbalestier D, Gurevich A, Feldmann DM, Polyanskii A (2001) High- T_c superconducting materials for electric power applications. *Nature* 414(6861):368–377
4. London F, London H (1935) The electromagnetic equations of the supraconductor. *Proc Royal Soc Lond Series A—Math Phys Sci* 149(866):71–88
5. Ginzburg VL, Landau LD (1950) On the theory of superconductivity. *Zh Eksp Teor Fiz*
6. Ginzburg VL, Landau LD (1957) *Sov Phys JETP*
7. Bardeen J, Cooper LN, Schrieffer JR (1957) Microscopic theory of superconductivity. *Phys Rev* 106(1):162–164
8. Bardeen J, Cooper LN, Schrieffer JR (1957) Theory of superconductivity. *Phys Rev* 108(5):1175–1204
9. Leon N, Cooper (1956) Bound electron pairs in a degenerate fermi gas. *Phys Rev* 104(4):1189–1190
10. Matthias BT, Geballe TH, Geller S, Corenzwit E (1954) Superconductivity of Nb_3Sn . *Phys Rev* 95(6):1435
11. Bednorz JG, Müller KA (1986) Possible high T_c superconductivity in the balacuo system. *Zeitschrift fr Physik B Condensed Matter* 64
12. Wu MK, Ashburn JR, Torng CJ, Hor PH, Meng RL, Gao L, Huang ZJ, Wang YQ, Chu CW (1987) Superconductivity at 93 k in a new mixed-phase y-ba-cu-o compound system at ambient pressure. *Phys Rev Lett* 58(9):908–910
13. Maeda H, Tanaka Y, Fukutomi M, T Asano (1988) A new high- T_c oxide superconductor without a rare earth element. *Jpn J Appl Phys*, 27(Part 2, No. 2):L209–L210
14. Vanderbemden P, Dorbolo S, Hari-Babu N, Ntatsis A, Cardwell DA, Campbell AM (2003) Behavior of bulk melt-textured YBCO single domains subjected to crossed magnetic fields. *IEEE Trans Appl Supercond* 13(2):3746–3749
15. Superconducting properties of natural and artificial grain boundaries in bulk melt-textured YBCO. *Phys C: Supercond* 302(4):257–270, 1998.

16. Nagamatsu J, Nakagawa N, Muranaka T, Zenitani Y, Akimitsu J (2001) Superconductivity at 39k in Magnesium diboride. *Nature* 410(6824):63–64
17. Ozawa TC, Kauzlarich SM (2008) Chemistry of layered d-metal pnictide oxides and their potential as candidates for new superconductors. *Sci Technol Adv Mater* 9(3):033003 (11pp)
18. Wu G, Xie YL, Chen H, Zhong M, Liu RH, Shi BC, Li QJ, Wang XF, Wu T, Yan YJ, Ying JJ, Chen XH (2009) Superconductivity at 56 K in Samarium-doped SrFeAsF. *Condens Matt* 21:142203
19. Bean CP (1964) Magnetization of high-field superconductors. *Rev Mod Phys* 36(1):31–39
20. Kim YB, Hempstead CF, Strnad A (1963) Magnetization and critical supercurrents. *Phys Rev* 129(2):528–535
21. Kim YB, Hempstead CF, Strnad AR (1962) Critical persistent currents in hard superconductors. *Phys Rev Lett* 9(7):306–309
22. Anderson PW (1962) Theory of flux creep in hard superconductors. *Phys Rev Lett* 9(7):309–311
23. Rhyner J (1993) Magnetic properties and AC-losses of superconductors with power law current–voltage characteristics. *Phys C: Supercond* 212(3–4):292–300
24. Brandt EH, Indenbom M (1993) Type-II-superconductor strip with current in a perpendicular magnetic field. *Phys Rev B* 48(17):12893–12906
25. Zeldov E, John R. Clem, McElfresh M, Darwin M (1994) Magnetization and transport currents in thin superconducting films. *Phys Rev B* 49(14):9802–9822
26. Majoros M, Ye L, Campbell AM, Coombs TA, Sumption MD, Collings EW (2007) Modeling of transport ac losses in superconducting arrays carrying anti-parallel currents. *IEEE Trans Appl Supercond* 17(2):1803–1806
27. Majoros M, Ye L, Velichko AV, Coombs TA, Sumption MD, Collings EW (2007) Transport ac losses in ybco coated conductors. *Supercond Sci Technol* 20(9):S299
28. Methods of mathematical physics (1953). Interscience Publishers, New York and London
29. Coombs TA, Campbell AM, Murphy A, Emmens M (2001) A fast algorithm for calculating the critical state in superconductors. *Int J Comput Math Electr Electron Eng* 20(1):240–252
30. Barnes G, McCulloch M, Dew-Hughes D (1999) Computer modelling of type ii superconductors in applications. *Supercond Sci Technol* 12(8):518–522
31. Amemiya N, Murasawa S -i, Banno N, Miyamoto K (1998) Numerical modelings of superconducting wires for AC loss calculations. *Phys C: Supercond* 310(1-4):16 – 29
32. Amemiya N, Miyamoto K, S -i Murasawa, Mukai H, Ohmatsu K (1998) Finite element analysis of AC loss in non-twisted B-i-2223 tape carrying AC transport current and/or exposed to DC or AC external magnetic field. *Phys C: Supercond* 310(1-4):30–35
33. Hong Z, Campbell AM, Coombs TA (2006) Numerical solution of critical state in superconductivity by finite element software. *Supercond Sci Technol* 19(12):1246–1252
34. Hong Z, Campbell AM, Coombs TA (2007) Computer modeling of magnetisation in high temperature bulk superconductors. *IEEE Trans Appl Supercond* 17(2):3761–3764
35. Vanderbemden Ph, Hong Z, Coombs TA, Denis S, Ausloos M, Schwartz J, Rutel IB, Hari Babu N, Cardwell DA, Campbell AM (2007) Behavior of bulk high-temperature superconductors of finite thickness subjected to crossed magnetic fields: experiment and model. *Phys Rev B* 75(17):174515
36. Vanderbemden P, Hong Z, Coombs TA, Ausloos M, Hari Babu N, Cardwell DA, Campbell AM (2007) Remagnetization of bulk high-temperature superconductors subjected to crossed and rotating magnetic fields. *Supercond Sci Technol* 20(9):S174–S183
37. Yuan W, Xian W, Ainslie MD, Hong Z, Yan Y, Pei R, Jiang Y, Coombs TA (2010) Design and test of a superconducting magnetic energy storage (SMES) coil. *IEEE Trans Appl Supercond* 20(3):1379–1382
38. Noe M, Steurer M (2007) High-temperature superconductor fault current limiters: concepts, applications, and development status. *Supercond Sci Technol* 20(3):R15
39. Clem JR, Claassen JH, Mawatari Y (2007) AC losses in a finite z stack using an anisotropic homogeneous-medium approximation. *Supercond Sci Technol* 20(12):1130–1139
40. Claassen JH (2006) An approximate method to estimate AC loss in tape-wound superconducting coils. *Appl Phys Lett* 88(12):122512

41. Grilli F, Ashworth SP (2007) Measuring transport AC losses in YBCO-coated conductor coils. *Supercond Sci Technol* 20(8):794–799
42. Grilli F, Ashworth SP (2007) Quantifying AC losses in YBCO coated conductor coils. *IEEE Trans Appl Supercond* 17(2):3187–3190
43. Brambilla R, Grilli F, Nguyen DN, Martini L, Sirois F (2009) AC losses in thin superconductors: the integral equation method applied to stacks and windings. *Supercond Sci Technol* 22(7):075018 (10pp)
44. Brambilla R, Grilli F, Martini L, Sirois F (2008) Integral equations for the current density in thin conductors and their solution by the finite-element method. *Supercond Sci Technol* 21(10):105008
45. Pardo E (2008) Modeling of coated conductor pancake coils with a large number of turns. *Supercond Sci Technol* 21(6):065014 (8pp)
46. Souc J, Pardo E, Vojenciak M, Gomory F (2009) Theoretical and experimental study of AC loss in high temperature superconductor single pancake coils. *Supercond Sci Technol* 22(1):015006 (11pp)
47. Muller K-H (1997) Self-field hysteresis loss in periodically arranged superconducting strips. *Phys C: Supercond* 289(1-2):123–130
48. Muller K-H (1999) AC losses in stacks and arrays of YBCO/hastelloy and monofilamentary Bi-2223/Ag tapes. *Phys C: Supercond* 312(1-2):149–167
49. Mawatari Y, Kajikawa K (2007) Hysteretic ac loss of superconducting strips simultaneously exposed to ac transport current and phase-different ac magnetic field. *Appl Phys Lett* 90(2):022506
50. Zhiyong Hong (2007) PhD Thesis, University of Cambridge

Chapter 3

Development of SMES Systems

3.1 Structure of SMES Systems

As energy storage devices, superconducting magnetic energy storage (SMES) systems utilise a relatively simple concept; it stores energy in the magnetic field created by the flow of direct current in a superconducting coil which has been cryogenically cooled to a temperature below its superconducting critical temperature.

The stored energy can be released back to a connected power system by discharging the coil. The power conditioning system uses a converter to transform alternating current (AC) power to direct current or convert DC back to AC power. Thus a typical SMES system includes four parts: a superconducting coil, a power conditioning system (PCS), a cryogenically cooled refrigerator and a protection device. Figure 3.1 gives the structure and devices of a SMES system.

Previously before the discovery of HTS materials, all SMES projects are using low-temperature superconductors, which require liquid helium as the cryogen. However, HTS-SMES system can use a dry-cooling cryocooler or liquid nitrogen to cool down as well. Using liquid nitrogen to cool down SMES is relatively easier, whereas a cryocooler can cool down to around 20 K at which the SMES can carry a much larger current. Figure 3.2 shows the SMES system using a cryocooler as the refrigerator.

A SMES device also needs a control system and power conditioning system to transfer energy in and out. It can be connected with an integrated power system, or distributed power system, such as propulsion systems for transportation. Figure 3.3 presents a complete SMES system including the control circuit, refrigerator and the protection circuit.

Once the superconducting coil is charged, the current will decay at a very small-rate which is determined by the resistance of the persistent switch. Usually the resistance of the persistent switch made of low-temperature superconductors is

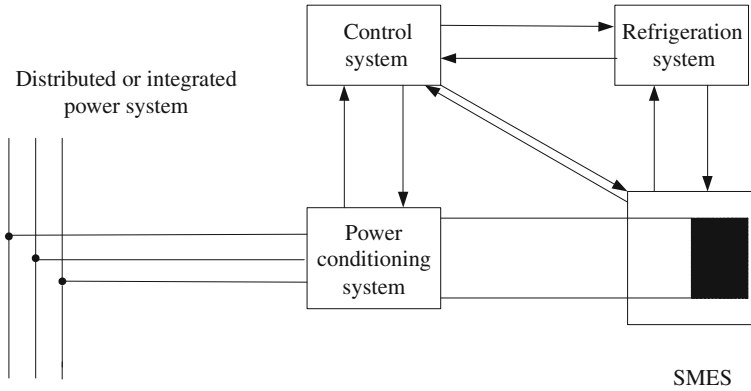


Fig. 3.1 SMES system connected to power system

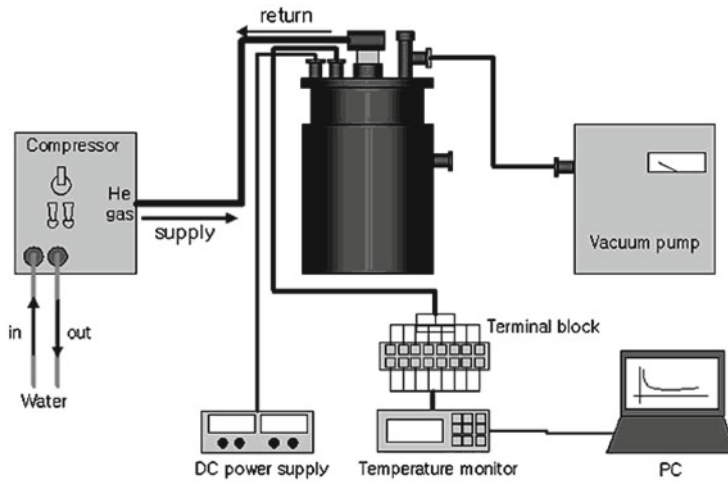


Fig. 3.2 SMES system using cryocooler as refrigerator [8]

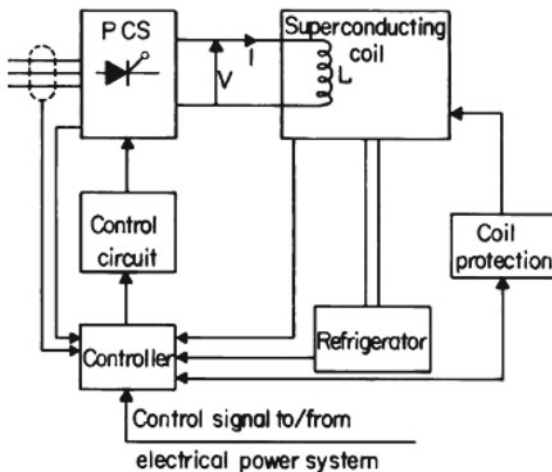
below $10^{-10} \Omega$ and the magnetic energy can be stored for a long time. If the coil were wound using a conventional wire, the magnetic energy would be dissipated as heat due to the wire's relatively large resistance to the flow of current. However, if the wire is superconducting which means there is very little resistance of it, then energy can be stored for a long time up to several years.

The magnetic energy stored by a coil carrying a current is given by one half of the inductance of the coil times the square of the current.

$$E = \frac{1}{2} L I^2 \quad (3.1)$$

where E is the coil energy, L is the coil inductance and I is the coil current.

Fig. 3.3 Complete SMES system components [8]



3.2 History of SMES Technology

Although the phenomenon of superconductivity was discovered in 1911 by Heike Kamerlingh Onnes, it was not used in industrial applications until decades later due to its extreme operating conditions and high cost. It was not until 1969 that the application of a SMES system was first proposed [1, 2]. That idea is to charge the superconducting magnet with the surplus generation of the basic load units during off-peak time, and to discharge to the power system during peak time.

Before HTS was discovered or even a long time after the discovery, the primary research interest in SMES was focused on LTS conductors. In Japan a 5000 MW/1000 MW SMES system was designed for utility load levelling (Masuda and Shintomi 1987). In the USA, a team headed by Bechtel, developed a 5000 MW/1000 MW SMES concept for the same application. The results of this baseline study led to two design-improvement and cost-reduction studies, also performed by Bechtel. Shortly after the birth of the Strategic Defense Initiative (SDI) the Engineering Test Model (ETM) project to build a 20 MW/400 MW SMES system for military applications was launched. The cryocooler for LTS SMES is too expensive and the cooling down process usually takes a long time, which makes it very difficult to start operating a LTS SMES.

At the early stage of SMES research, it was almost exclusively considered as a potential solution for utility application. Researchers usually spend many years building a large SMES with the stored energy of several hundred Mega Joules or even more than 1000 MJ, in order to damp system oscillations, to enhance voltage stability, to reduce area-control error (ACE), to provide load levelling and to provide spinning reserve [3].

Since the discovery of HTS, almost all HTS-SMES systems have been proposed or built using BSCCO wire. This is because BSCCO wire is the first commercially available HTS conductor. The cost of cryogen is greatly reduced due to the HTS conductor's higher critical temperature than LTS wires. These two factors make HTS conductors popular in winding SMES coils.

As early as 1993, a conceptual design of HTS-SMES was published by the researchers in the US [4]. The proposed SMES unit has been investigated over the mid-size energy range of 2 to 200 MW (7.2–720 GJ), using the Bismuth-based superconductor-BSCCO. This research project was supported by US Department of Energy. Many effects have been considered including the critical current density on feasible configurations, mass of conductor, cost and magnetic field and strain limits. In the end the paper noted several developments needed for HTS-SMES to exceed LTS SMES. These suggestions are still very valuable today. They are: (1) improving J_c and reducing the cost of HTS material, (2) designing for higher field operation, (3) increasing the strain range, (4) minimizing AC loss.

The researchers in American Superconductor corporation reported their test results of a 5 kJ HTS-SMES in 1997 [5]. Their magnet consisted of a solenoid coil constructed from Bi-2223 conductor, working at the temperature of 25 K. It was built and cryo-integrated by American Superconductor, and then connected to a scaled grid in Germany. Actually it was the first reported significant size HTS-SMES that had been successfully constructed. The successful design and testing of this HTS-SMES proved that HTS conductors could be utilised in commercial products.

Since the first commercial generation of HTS conductor, Bi-2223, became available in the late 1990s, more and more HTS-SMES have been proposed, designed and constructed. Their sizes vary from small-scale (several hundred Joules) to large-scale (several Mega Joules), and they are mainly used in electric power application.

Friedman wrote a paper about HTS-SMES operating at liquid nitrogen temperatures for electric power application in 2003 [6]. This laboratory-scale SMES which could store up to 1.2 kJ energy consisted of BSCCO tapes and operated at 77 or 64 K. Although the stored energy was only 1.2 kJ, the unique ferromagnetic core increased the stored energy by a factor of more than five and, at the same time, decreased the perpendicular field component on the windings. They also developed a cryogenic DC–DC convertor immersed in the LN_2 , which yielded low losses and high operational efficiency. These special improvements have been implemented in this SMES device, to compensate the voltage drops in the standard three phase grid.

Many companies are also actively involved in HTS-SMES projects. Within the frame of the publicly funded German project high temperature superconducting magnetic energy storage the companies ACCEL, AEG SVS, EUS, and the utility company have developed a 150 kJ HTS-SMES for a 20 kVA uninterruptible power supply system [7]. The superconducting coil is composed of twenty double pancakes wound of a high temperature superconductor tape with BSCCO-2223 filaments. A test module composed of two double pancakes has been manufactured.

With a cryostat free of cryogenes, the whole device was cooled down to 77 K and stably operated with a current of 17 A.

Korea is also leading a HTS-SMES project. Researchers have published their papers about their HTS-SMES system, in which they are using BSCCO-2223 wire to wind the coil. Their paper published in 2005 gave us the characteristic test results of HTS pancake coil modules for their small-sized SMES [8]. Another paper in 2007 gave the stress analysis of the HTS magnet. The operating temperature of this 600 kJ SMES was 20 K [9]. Unlike the early researchers, the Korean researchers were using the pancake as the configuration of the coil, with the optimization process based on evolution strategy and FEM. GM cryocoolers and bridge type converters were used to operate this SMES device. The test results were consistent with the calculated results.

The University of Wollongong has developed the design for a 20 kJ SMES device for compensating the voltage sags. They constructed their 2.5 kJ prototype using BSCCO-2223 tape, and operated their device at the temperature of 25 K. Besides the SMES coil, they also developed the Power Control Circuit (PCC) to control the power flow in the SMES system [10, 11]. Their SMES circuit topology was to install the SMES circuit in series with a Voltage Source Inverter (VSI) as the inverter configuration.

An HTS-SMES device has been realised using a 350 m long BSCCO tape wound as a pancake coil in University of Liege in Belgium. The superconducting properties were tested when the coil was cooled down to 17.2 K. This SMES was built up in order to supply a stable voltage of 30 V, and this UPS capability was demonstrated in another experiment [12].

In 2004, a four-year Japanese national project was launched to develop an HTS-SMES coil. The objective was to obtain high energy density via an HTS-LTS hybrid coil system. The HTS coil was composed of 16 double-pancake coils and the coil was wound with a BSCCO-2212 Rutherford-type cable. This SMES system was tested at the temperature of 4.2 K with a maximum magnetic field of 8.9 T in HTS and 3.5 T in LTS. This unit could store up to 6.5 MJ energy. Mechanical compression test, DC operation test and thermal runaway test have been performed on the SMES coil [13].

A SMES system using Bismuth PIT tape with the 2212 stoichiometry (BSCCO-2212) was under research in France [14]. The SMES coil consists in 26 superposed simple pancakes wound and bonded on sliced copper plates coated with epoxy. The rated current is 315 A for an energy of 814 kJ. During operation the SMES is cooled down to 20 K by cryocoolers. One experiment result shows that from a current of 244 A, this SMES delivered 425 kJ to a resistance with a maximum power of 175 kW. This SMES system is designed as a current source in a weapon system.

Some other SMES projects have also been proposed. Although the device has not yet been constructed, the simulation and design have been studied. In High Energy Accelerator Research Organization in Japan, researchers intend to combine the LH₂ cryocooler and HTS conductor to build a SMES system, which is designed as a backup for supplying electricity to hospitals and other high-rise

Table 3.1 Summary of SMES projects

Names	Year	Stored energy	Material	Temperature (K)
Australian SMES	2005	2.48 kJ	BSSCO-2223	25
Korean HTS-SMES	2005	626 kJ	BSSCO-2223	20
Japan FBC coil	2004	270 kJ	NbTi	4.2
Israel SMES	2003	1.5 kJ	BSSCO-2223	64
Japanese UPS SMES	2007	100 kJ	NbTi	4.2
Japanese hybrid SMES	2007	14.9 kJ	BSSCO-2212	4.2
Japanese CIC SMES	2004	2.9 MJ	NbTi	4.2
Japanese SMES	2003	100 kJ	BSSCO-2212	20
Italian SMES	1999	2.6 MJ	NbTi	4.2
ACCEL SMES	2003	2 MJ	NbTi	4.2
French SMES	2008	814 kJ	BSSCO-2212	20

office buildings [15]. In addition, the researchers intend to combine a fuel cell and a SMES. At a power failure, the fast response SMES will immediately supply electric power in the first few seconds, then the fuel cell will substitute SMES for power supply. However, LH_2 is not yet considered as a safe cryogen and safety is always the essential concern with this system.

Table 3.1 gives a summary of some of the aforementioned SMES projects mentioned.

3.3 Comparison of SMES with Other Energy Storage Systems

Energy storage is the storing of some form of energy that can be drawn upon at a later time to perform some useful operation. There are five forms of energy storage methods: chemical (bio-fuels, etc.), electrochemical (batteries, fuel cells, etc.), electrical (capacitor, super-capacitor, SMES), mechanical (compressed air energy storage, flywheel energy storage [16–18], pumped hydro energy storage, etc.) and thermal (molten salt, cryogenic liquid, etc.). A comparison of typical energy storage devices is presented below.

- Cyclic efficiency

Since there is no resistance of superconductors in the critical state, the efficiency of SMES is particularly high compared to other energy storage devices. Table 3.2 gives the comparison of the efficiencies. From Table 3.2 we can see out among the energy storage devices listed, SMES has the highest efficiency.

- Response time

As an electrical device, SMES has the fastest response time since it has purely electrical energy conversion, whilst other energy storage devices involve either

Table 3.2 Comparison of efficiencies of different energy storage devices

Compressed air energy storage	80%
Pumped hydro	75%
Batteries	75%
Flywheels	80%
SMES	90%

Table 3.3 Comparison of response times of energy storage devices

Type of storage	Relative access time (%)
Capacitors	0.1–1
Pumped hydro	100,000
Batteries	100
Flywheels	1–10
SMES	0.1–1

The access time is all normalised to that of batteries

electrical–chemical or electrical–mechanical energy conversion which is much slower [1]. Table 3.3 presents the comparison of response times.

• Energy density and power density

Energy density and power density are two important factors to compare energy storage devices. From Fig. 3.4 [19], we can clearly find out that SMES has achieved a good balance between the energy density and the power density in terms of mass compared to other energy storage devices. Additionally, since the critical current of the commercial 2G HTS tapes improves significantly, the energy density of a 2G HTS-SMES system also achieves a large amount of increase.

Figure 3.5 presents the comparison of discharge time and power rating for different energy storage systems. We can see that SMES is one of the highest power-rating systems, at the same time it does not have a long discharge time. These characteristic have made SMES suitable for particular applications such as power source for propulsion systems, voltage sag compensation devices for power grids and so on. Section 3.4.1 will explain the applications in detail.

• Recharge capability

In theory, a SMES device can be discharged and recharged unlimitedly, and the cyclic efficiency will always be at a high-level 90%. Batteries are not like SMES devices, and they cannot be discharged or recharged unlimitedly. Their cyclic efficiency will also reduce as the using cycles increase. Other energy storage devices that involve with electrical–chemical or electrical–mechanical energy conversion can neither be cycled unlimitedly; they all have a certain amount of loss due to depreciation in every cycle which will reduce the efficiency.

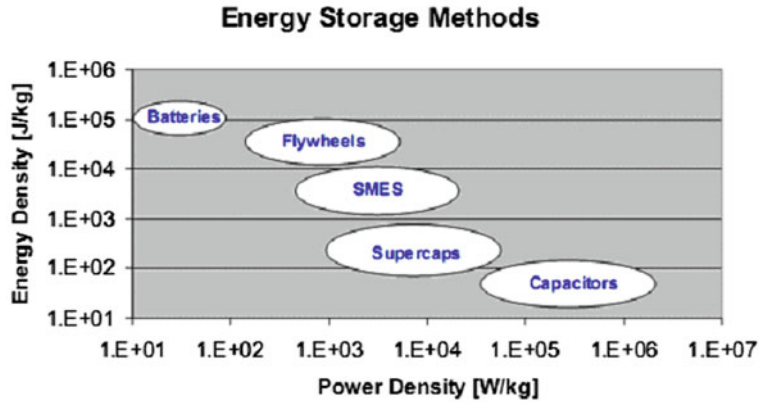


Fig. 3.4 Comparison of energy and power density for different energy storage systems

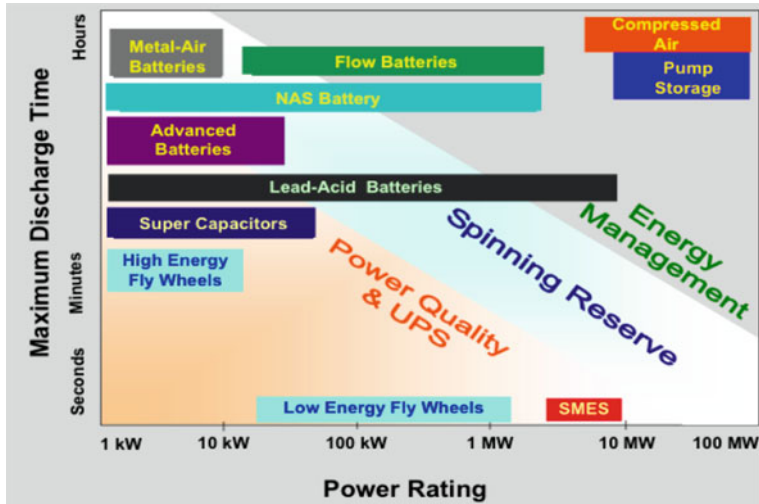


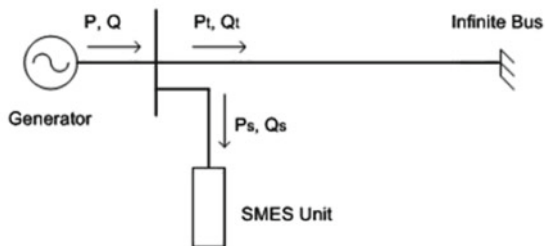
Fig. 3.5 Comparison of discharge time and power ratings for different energy storage systems

3.4 Application of SMES Technology

3.4.1 Application of SMES Technology in Power Grids

SMES systems can convert the AC current from a utility system into the DC current flowing in the superconducting coil and store the energy in the form of magnetic field. Conversely the stored energy can be released to the AC system when necessary. These capabilities of SMES systems offer very desirable benefits

Fig. 3.6 SMES system connected to large power grid providing both active and reactive power. In the diagram active power is represented by P and reactive power is represented by Q



to power system applications. A number of reported studies explored and investigated feasible SMES applications to power systems. These applications can basically be classified into two aspects: one is system stability enhancement and the other is power quality improvement [3].

Referred to enhance system stability enhancement, SMES systems can actively reduce low-frequency oscillations in power systems. Low-frequency oscillations (0.5–1 Hz) following a major system disturbance are usually used to describe power system stability limitations. Power transfers are often limited to prevent growing oscillations from occurring, following the loss of a single major transmission line or generator. When limited by long-term stability the transmission capacity can be increased through actively damping these oscillations. These system oscillations can be reduced by SMES systems through modulation of both real power and reactive power.

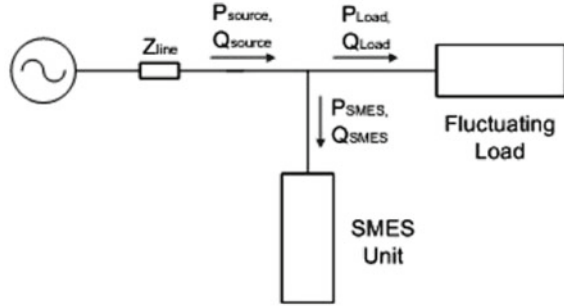
In addition, SMES systems can be used to boost voltage stability. Dynamic voltage instability will occur when there is a major loss of generation or heavily loaded transmission line and there is insufficient dynamic reactive power to maintain voltages. A SMES system is able to stabilise the system long enough to allow generators or other reactive power sources to come on line and thus prevent voltage instability, by providing real power and reactive power simultaneously.

Figure 3.6 presents a schematic diagram of a typical power transmission system with a SMES unit for reducing system oscillations and boosting voltage stability.

With regards to improving power quality, SMES systems can offer energy storage for flexible AC transmission system (FACTS) devices. FACTS inverters and power conditioning systems of SMES systems worked in very similar ways. SMES can enhance FACTS performance by providing more real power in addition to reactive power. A static synchronous compensator (StatCom) can only absorb or inject reactive power, and consequently is limited in the degree of freedom and sustained action in which it can help the power grid. The active energy from SMES permits the StatCom to inject or absorb active and reactive power simultaneously, and therefore offers additional benefits and improvements in the system. In addition, SMES systems can offer spinning reserves, balancing power system asymmetries and decreasing area control error.

When used to improve power quality, a SMES system usually needs an enormous amount of energy. During the early days of SMES research, the superconducting

Fig. 3.7 SMES system connected with distributed power system balancing fluctuating load. In the diagram active power is represented by P and reactive power is represented by Q



coils are using tons of superconductors to be able to store a large amount of energy. However, large coils will bring technical challenges such as safety issues, leakage magnetic field and mechanical stability problems.

3.4.2 Application of SMES Technology in Distributed Power Systems

Besides working in power grids, SMES can also be used in distributed power systems as a back up power supply, balancing fluctuating loads and providing a large pulse power [20–22]. And they also have smaller capacities and different control strategies compared to those used in large power grids.

Since SMES can store a significant amount of energy it is possible that SMES provides enough reserve to satisfy the requirement until other back up generators can be brought online. Offering back up power supply by using SMES is much faster than other energy storage devices.

In addition, a SMES device is promising for balancing fluctuating active and reactive power from various loads such as industrial manufacturing plants, nuclear fusion power plants, and aircraft power system. Figure 3.7 depicts a typical SMES control system to compensate for fluctuating loads, located close to the customer end.

Since a SMES system has a relatively high power density and discharge its power within a very short time, it can also be used to provide a large pulsed power in transportation such as aircraft and ship.

3.4.3 SMES Application for Aircraft Taxiing

Taxiing refers to the movement of an aircraft on the ground under its own power. An aircraft uses taxi ways to taxi from one place on an airport to another; for example, moving from a terminal to the runway is taxiing. Normally taxiing does

not include the accelerating run along a runway prior to take-off, or the decelerating run immediately after landing.

At present the energy source to propel a commercial aircraft forward comes from its propellers or jet engines. When taxiing, aircraft travel slowly. This makes sure that they can be stopped fast and do not risk wheel damage on larger aircraft when accidentally turning off the paved surface. Since aircraft is moving very slowly when taxiing, the efficiency of petrol combustion aero-engines is low due to insufficient combustion of petrol. For every one minute of taxiing time, an airline operating a Boeing 737 consumes almost four gallons of fuel, a Boeing 747 will consume 15 gallons of jet fuel in four minute period [23]. This is not only a waste of money for petrol, but also a waste of energy in an energy-short world.

In addition, the low efficiency of petrol combustion aero-engines would raise environmental problems. The on-airport greenhouse gas emissions take up 12.5% of worldwide emissions produced by aircraft. In many airports passengers and airport personnel must be kept at a sufficient distance from any aircraft having a gas turbine engine in operation due to the noise and the wake created by an operating engine.

Therefore researchers begin to consider using electric power to drive the taxiing of aircraft instead of engines. Although there is auxiliary power unit (APU) in aircraft for on-aircraft electrical needs (lighting, instruments, etc.), the current APU has a limited capacity that it should be twice as big to supply the power and energy needed for electric taxiing of aircraft. Thus an additional energy storage device is needed in this occasion to support electrical taxiing of aircraft, and to reduce emissions and save airlines money through greater fuel efficiency. A SMES system will be a good candidate to supply the power for the taxiing of aircraft.

3.5 Current Problems with SMES Projects

Due to the massive commercial production of 2G HTS conductors, it is now possible to use them winding SMES coils. Compared to 1G HTS conductors, 2G HTS conductors have obvious advantages: they have larger critical currents and can sustain larger magnetic fields. Therefore the project in this thesis is using 2G HTS tapes to wind SMES coils.

However, there are several crucial problems needed to be investigated in SMES systems using 2G HTS tapes.

- Since 2G HTS tapes are relatively more expensive, it is necessary to store the maximum energy in the SMES using a certain length of conductors. This will be investigated in [Chap. 4](#).
- 2G HTS tapes have significantly different configurations with other superconducting conductors including 1G HTS conductors. They have a flat and thin cross-section. Thus we need an efficient and new model to analyse the 2G HTS coils. Based on the design introduced in [Chap. 4](#), modelling and experiment of a numerical model for 2G HTS coils are presented in [Chaps. 5 and 6](#).

- Unlike other SMES systems, there is no persistent mode for 2G HTS SMES systems since a persistent switch with less than $10^{-10} \Omega$ resistance cannot be made. This brought a challenge to the control circuit. Chapter 6 also gives the design of the control circuit, which is both validated by simulation and experiment.

References

1. Seeber B et al (1998) Handbook of applied superconductivity. CRC press, Boca Raton
2. Luongo CA (1996) Superconducting storage systems: an overview. Magn IEEE Trans 32(4):2214–2223
3. Xue XD, Cheng KWE, Sutanto D (2006) A study of the status and future of superconducting magnetic energy storage in power systems. Supercond Sci Technol 19(6):R31–R39
4. Schoenung SM, Meier WR, Hull JR, Fagaly RL, Heiberger M, Stephens RB, Leuer JA, Guzman RA (1993) Design aspects of mid-size SMES using high temperature superconductors. Appl Supercond IEEE Trans 3(1):234–237
5. Kalsi SS, Aized D, Conner B, Snitchier G, Campbell J, Schwall RE, Kellers J, Stephanblome T, Tromm A, Winn P (1997) HTS-SMES magnet design and test results. Appl Supercond IEEE Trans 7(2):971–976
6. Friedman A, Shaked N, Perel E, Gartzman F, Sinvani M, Wolfus Y, Kottick D, Furman J, Yeshurun Y (2003) HT-SMES operating at liquid nitrogen temperatures for electric power quality improvement demonstrating. Appl Supercond IEEE Trans 13(2):1875–1878
7. Kreutz R, Salbert H, Krischel D, Hobl A, Radermacher C, Blacha N, Behrens P, Dutsch K (2003) Design of a 150 kJ high-Tc SMES (HSMES) for a 20 kVA uninterruptible power supply system. Appl Supercond IEEE Trans 13(2):1860–1862
8. Kim JH, Kim W-S, Hahn S-Y, Lee JM, Rue MH, Cho BH, Im CH, Jung HK (2005) Characteristic test of HTS pancake coil modules for small-sized SMES. Appl Supercond IEEE Trans 15(2):1919–1922
9. Park M-J, Kwak S-Y, Kim W-S, Lee S-W, Lee J-K, Han J-H, Choi K-D, Jung H-K, Seong K-C, yop Hahn S (2007) AC loss and thermal stability of HTS model coils for a 600 kJ SMES. Appl Supercond IEEE Trans 17(2):2418–2421
10. Hawley CJ, Gower SA (2005) Design and preliminary results of a prototype HTS-SMES device. Appl Supercond IEEE Trans 15(2):1899–1902
11. Hawley CJ, Cuiuri D, Cook CD, Gower SA, Beales TP (2006) Characterisation and control of a prototype HTS-SMES device. J Phys Conf Ser 43:809–812
12. Fagnard J-F, Crate D, Jamoye J-F, Laurent Ph, Mattivi B, Cloots R, Ausloos M, Genon A, Vanderbemden Ph (2006) Use of a high-temperature superconducting coil for magnetic energy storage. J Phys Conf Ser 43:829–832
13. Tosaka T, Koyanagi K, Ohsemochi K, Takahashi M, Ishii Y, Ono M, Ogata H, Nakamoto K, Takigami H, Nomura S, Kidoguchi K, Onoda H, Hirano N, Nagaya S (2007) Excitation tests of prototype HTS coil with Bi2212 cables for development of high energy density SMES. Appl Supercond IEEE Trans 17(2):2010–2013
14. Tixador P, Deleglise M, Badel A, Berger K, Bellin B, Vallier JC, Allais A, Bruzek CE (2008) First tests of a 800 kJ HTS-SMES. Appl Supercond IEEE Trans 18(2):774–778
15. Makida Y, Hirabayashi H, Shintomi T, Nomura S (2007) Design of SMES system with liquid hydrogen for emergency purpose. Appl Supercond IEEE Trans 17(2):2006–2009
16. Coombs T, Campbell AM, Storey R, Weller R (1999) Superconducting magnetic bearings for energy storage flywheels. Appl Supercond IEEE Trans 9(2):968–971
17. Coombs TA, Campbell AM, Cardwell DA (1995) Development of an active superconducting magnetic bearing. Appl Supercond IEEE Trans 5(2):630–633

18. Coombs TA, Cardwell DA, Campbell AM (1997) Dynamic properties of superconducting magnetic bearings. *Appl Supercond IEEE Trans* 7(2):924–927
19. Schnyder G, Sjoström M (2005) SMES. *HTS Power Syst* 18:1–3
20. Tripathy SC, Kalantar M, Balasubramanian R (1991) Dynamics and stability of wind and diesel turbine generators with superconducting magnetic energy storage unit on an isolated power system. *Energy Convers IEEE Trans* 6(4):579–585
21. Zhou F, Joos G, Abbey C, Jiao L, Ooi BT (2004) Use of large capacity SMES to improve the power quality and stability of wind farms. In: *Power engineering society general meeting, 2004. IEEE*, vol 2, 10-10, pp 2025–2030
22. Nomura S, Ohata Y, Hagita T, Tsutsui H, Tsuji-Iio S, Shimada R (2005) Wind farms linked by SMES systems. *Appl Supercond IEEE Trans* 15(2):1951–1954
23. Cooper P, Greenhouse emissions inventory fact sheet. <http://www.portseattle.org/downloads/community/environment/greenhousefactsheet> et.

Chapter 4

Coil Design

This chapter firstly introduces the characteristics of the second generation high-temperature superconductors (2G HTS) tapes used to wind the Superconducting Magnetic Energy Storage (SMES) coil. The critical current of the tape in external magnetic fields with different angles is presented by graphs. Then it gives the optimisation process of getting the maximum energy out of a certain length of conductor. A few optimisations which do not work as expected are also included and the reason is analysed.

4.1 Second Generation High-Temperature Superconductors Tape

Long length of 2G HTS tapes recently became commercially available. This makes it possible to wind the tapes into coils which could produce a large magnetic field for a large scale application. We are using SuperPower's 2G HTS wires (coated conductors), based on YBCO. This 2G HTS wire is fabricated by an automated, continuous process using thin film deposition techniques, such as those used in the semiconductor industry, to apply the superconducting material on buffered metal substrates. The structure of the superconducting tape is shown in Fig. 4.1 [1]. The superconducting layer in the tape is actually very thin, only about 1 μm . This tape uses high-strength, non magnetic and highly-resistive Hastelloy substrate. Higher resistance leads to lower eddy current AC loss, and non-magnetic property leads to lower ferromagnetic AC loss. Therefore this kind of tape has better mechanical properties and lower AC losses. Surround copper stabilizer (SCS) is

Parts of this chapter are reprinted with permission from Weijia Yuan et al, Design and test of a Superconducting Magnetic Energy Storage (SMES) coil, IEEE transaction on applied superconductivity, 20(3):1379–1382, 2010. copyright©2010 IEEE.

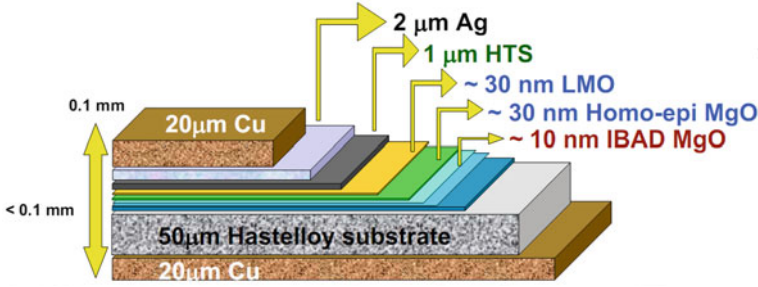


Fig. 4.1 Structure of 2G HTS tapes from superpower

Table 4.1 Characteristics of Superpower's SCS 4050 and SCS 12050 tapes

Characteristic	SCS4050	SCS12050	Comments
Tape width	4 mm	12 mm	
Individual conductor thickness	0.1 mm	0.1 mm	
Insulation + epoxy thickness	0.05 mm	0.05 mm	
Total thickness of the tape	0.15 mm	0.15 mm	
Critical current (self-field, 77 K)	80 A	240 A	
Stabilizer	Copper	Copper	
Substrate thickness	0.05 mm	0.05 mm	Hastelloy C276
Yield strength	1,200 MPa	1,200 MPa	At 76 K
Critical bend diameter in tension	11 mm		room temperature
Critical axial tensile strain	0.45%		76 K
Substrate resistance	125 mΩ · cm	125 mΩ cm	
Substrate magnetic properties	Non-magnetic		
I_c Uniformity	±%10 deviation		

applied to completely encase the wire. There are no sharp corners on this tape and this is valuable for high voltage applications.

Superpower produces two types of tapes with different widths. The detailed specification of the two tapes is listed in Table 4.1 [1].

Figures 4.2 and 4.3 give the angular dependence of Superpower's tapes. All the data of the tape performance is provided by Superpower Inc. [1]. It is clear that the tape's performance mainly depends on the perpendicular field (perpendicular to $a - b$ plane).

Therefore for this thesis, we will only consider the perpendicular field's impact on the tapes. Figures 4.4 and 4.5 show the performance of the superconducting tape in a perpendicular field. We can see how the critical current decreases when the applied field increases at different temperatures.

For our coil, we tested it at liquid nitrogen temperature 77 K. If the coil is cooled down by a cryocooler, it will operate at around 22 K. Therefore we interpolate the data from Figs. 4.4 and 4.5 with Kim model as introduced in Eq. 2.7, and then we get Eqs. 4.1 and 4.2. In the following calculations of this thesis, the current densities in Eqs. 4.1 and 4.2 all indicate the engineering current density.

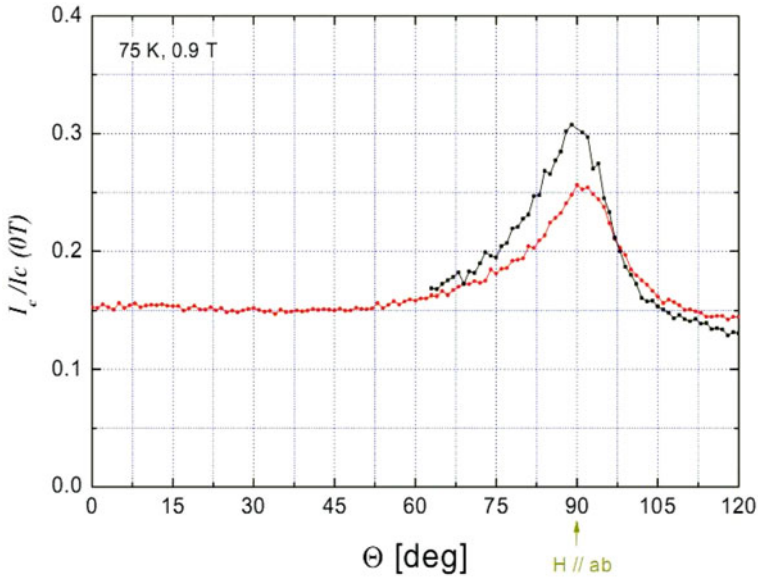


Fig. 4.2 Angular dependence of two representative superpower's tapes

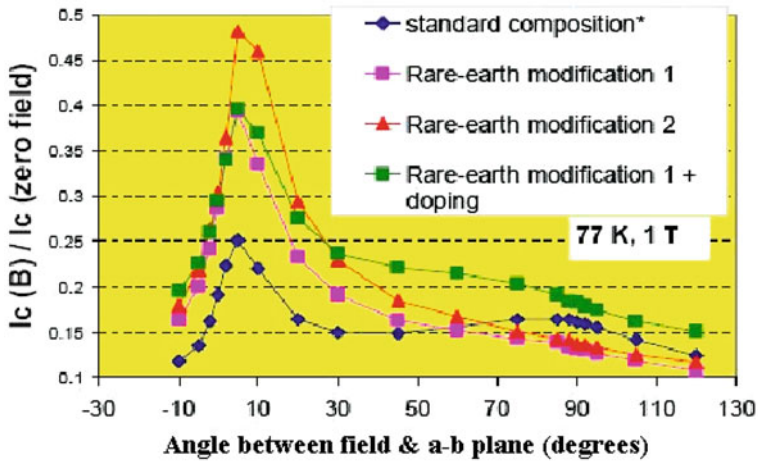


Fig. 4.3 Angular dependence of superpower's tapes with different doping methods

$$J_{c,77K} = J_{0,77K} \times \frac{B_{0,77K}}{B_{0,77K} + |B_z|} \quad (4.1)$$

where $J_{0,77K} = 1.11 \times 10^8 \text{ A/m}^2$, $B_{0,77K} = 0.12 \text{ T}$.

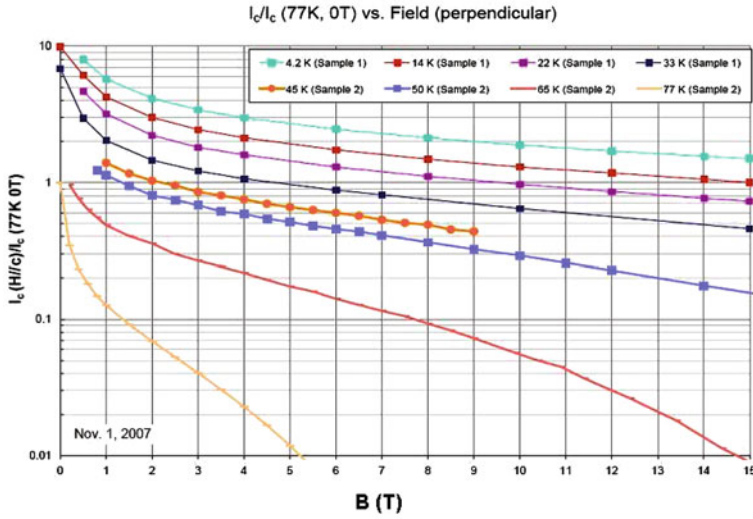


Fig. 4.4 Superpower's 2G HTS tape I_c for different applied fields

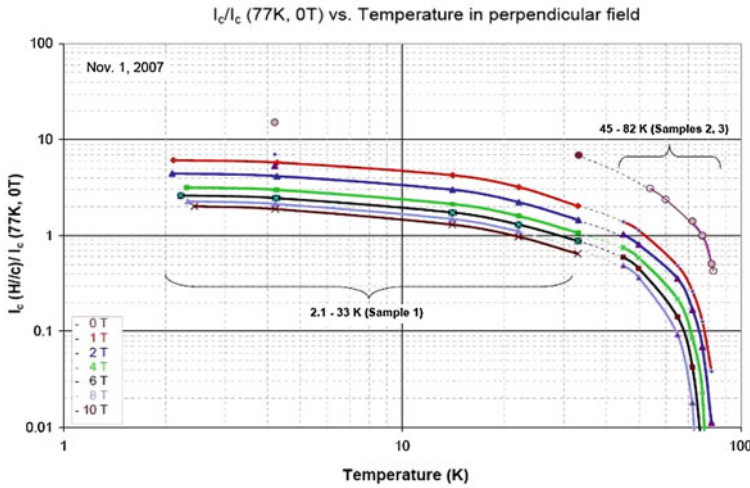


Fig. 4.5 Superpower's 2G HTS tape I_c at different temperatures

$$J_{c,22\text{ K}} = J_{0,22\text{ K}} \times \frac{B_{0,22\text{ K}}}{B_{0,22\text{ K}} + |B_z|} \quad (4.2)$$

where $J_{0,22\text{ K}} = 6.58 \times 10^8 \text{ A/m}^2$, $B_{0,22\text{ K}} = 1.49\text{ T}$.

The SCS4050 tape used to wind our mini double-pancake coils is coming from 185 to 275 m in one spool. The critical current and n values of the tape is given by Fig. 4.6.

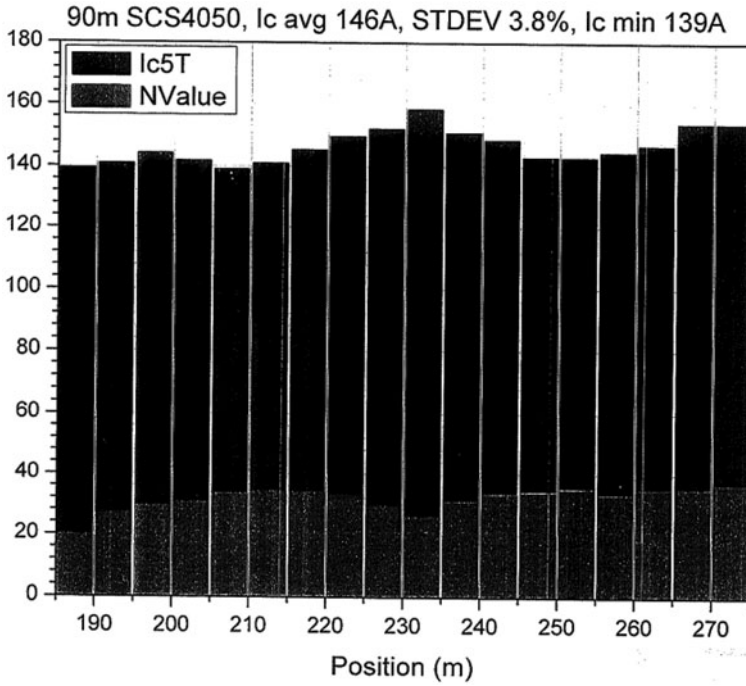


Fig. 4.6 Critical currents and n values of the tape

4.2 Coil Design

Since 2G HTS tapes have a thin strip configuration and their performance decrease rapidly if twisted, they are usually wound into a pancake coil configuration with many turns, rather than the conventional solenoid configuration.

In contrast with the superconducting coil in accelerator or MRI applications, the aim of the SMES coil is to achieve the maximum stored energy rather than the maximum or uniform magnetic field. Another factor considered is the economy factor, the coil cost will be equivalent of 100-m long 12 mm-width tape.

The energy stored in a coil is,

$$E = \frac{1}{2} \times LI^2 \quad (4.3)$$

where E is the total stored energy, L is the inductance of the coil, and I is the current through the coil.

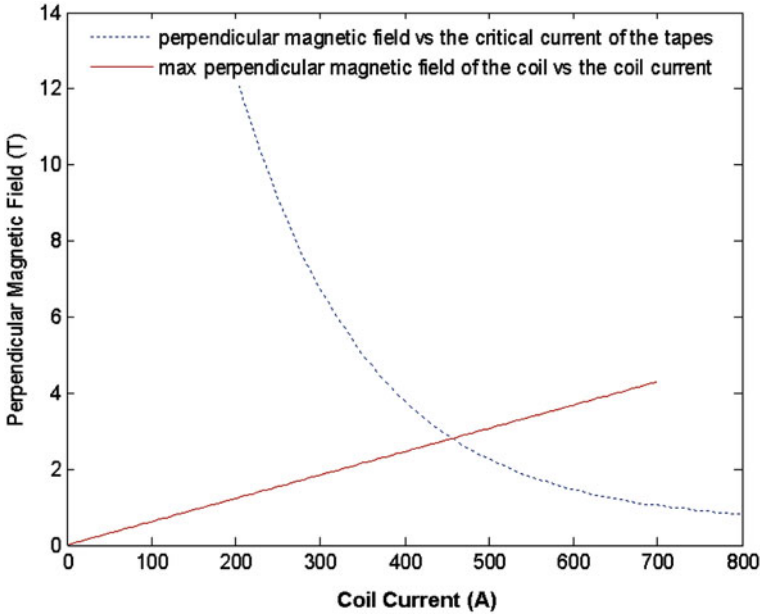


Fig. 4.7 Solution to achieve maximum working point

4.2.1 Optimisation with 12-mm-Width Tape

Firstly we use a 100-m long 12-mm-width tape in the optimisation process.

In order to get the maximum stored energy, we need to increase both L and I and then find the optimum point which makes E maximum. The maximum current will be the critical current of the tape, which is determined by the magnetic field and the temperature. Since the perpendicular magnetic field has a much larger impact on the critical current of the tapes, we only consider the perpendicular magnetic field B_z . It is assumed that the current density is distributed all across the tape but not only in the superconducting layer, i.e. the engineering current density. This SMES coil will finally operate at 22 K, thus we are using Eq. 4.2 to describe the J_c-B relation of the tape. The inductance L will be determined by the configuration of the coil.

To get the maximum energy, we developed the algorithm shown in Fig. 4.8. Since the total length of the conductor is a fixed value, if we choose a set of the inner radius and layer number of the coil, the width of the coil can be calculated and one coil configuration design is then achieved. For each particular configuration, the current in the coil can be increased until it reaches the critical current given by Eq. 4.2 at the maximum field in the coil. Figure 4.7 gives how to calculate the maximum current. This is a conservative consideration. A certain number of the sets of the inner radius and the layer number can be chosen which are practical from an engineering perspective. Therefore a table of the stored

Fig. 4.8 Optimisation algorithm to achieve maximum energy

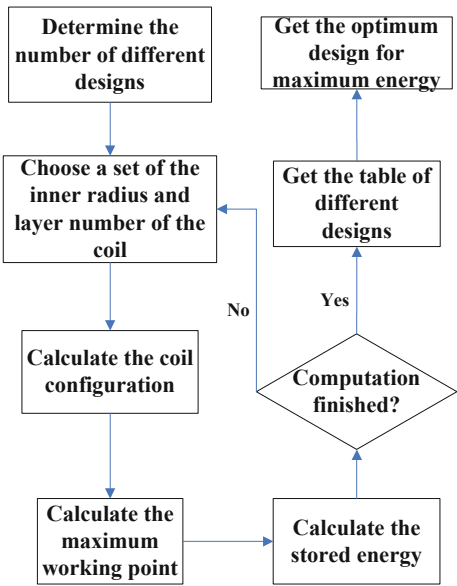


Table 4.2 Pancake coil design using 12-mm-width tape, giving maximum energy

Coil properties	Quantity
Inner radius	40 mm
Outer radius	79.9 mm
Coil height	12 mm
Conductor length	100 m
Turns	266
Inductance	10 mH
Operation temperature	22 K
Operation current	418 A
Stored energy	863 J

energies of the coil can be calculated for different configurations, and the design that gives the maximum stored energy can be selected.

The computation result shows that one-layer pancake design will give the maximum energy. Table 4.2 shows the details of this design.

4.2.2 Further Optimisation with 12-mm-Width Tape

By investigating the magnetic field distribution of the pancake coil, we find that the maximum perpendicular magnetic field exist on the top and bottom surface of the coil. Since the maximum operating current decreases when the maximum perpendicular magnetic field increases, we could potentially increase the maximum

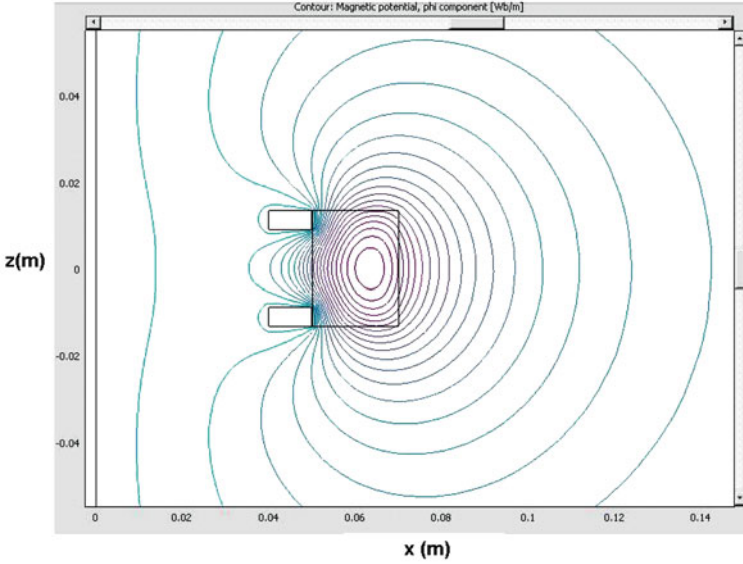


Fig. 4.9 Cross-section view of an axis-symmetric partially diamagnetic shielded SMES coil. The big block represents the coil, and the two small blocks represent the shielding

operation current and eventually the stored energy by decreasing the perpendicular magnetic field (if the coil configuration does not change).

We naturally came up with the idea to use diamagnetic materials to shield the perpendicular magnetic field around the top and bottom surface. Using a commercially FEM software Comsol/Multiphysics, we built up two models to investigate the shielding effect: partially diamagnetic shielding and completely diamagnetic shielding. However, the results show that the shielding method does not work the way we expected. This is because there is always a gap between the shielding material and the coil surface, thus the flux will be pushed into the narrow gap, which results in a even bigger local perpendicular field than that without shielding. Figures 4.9 and 4.10 present the results of two different shielding effects.

The other way to protect the coil from the perpendicular magnetic field is to put separate windings with a opposite-direction current near the top and bottom surface of the SMES coil. These so-called cancellation windings can reduce the maximum perpendicular field and would potentially increase the stored energy.

We modelled two different cancellation windings as shown in Figs. 4.11 and 4.12. The flux distribution shows that the maximum perpendicular field in the coil has been reduced. Then we calculated the maximum operating currents and energies. A comparison of the design with and without cancellation windings is presented in Table 4.3.

From Table 4.3 we find the cancellation windings cannot give the SMES coil a higher store energy. Although the windings do reduce the perpendicular magnetic

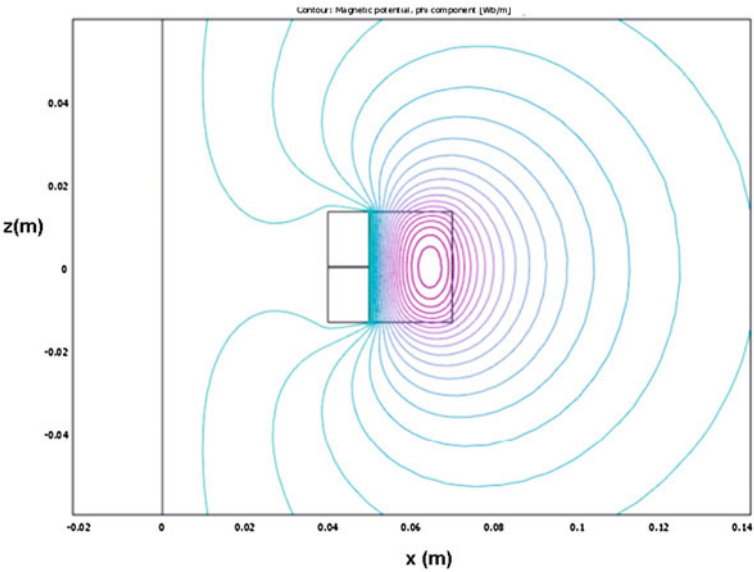


Fig. 4.10 Cross section view of an axis-symmetric completely diamagnetic shielded SMES coil. The big block represents the coil, and the two small blocks represent the shielding

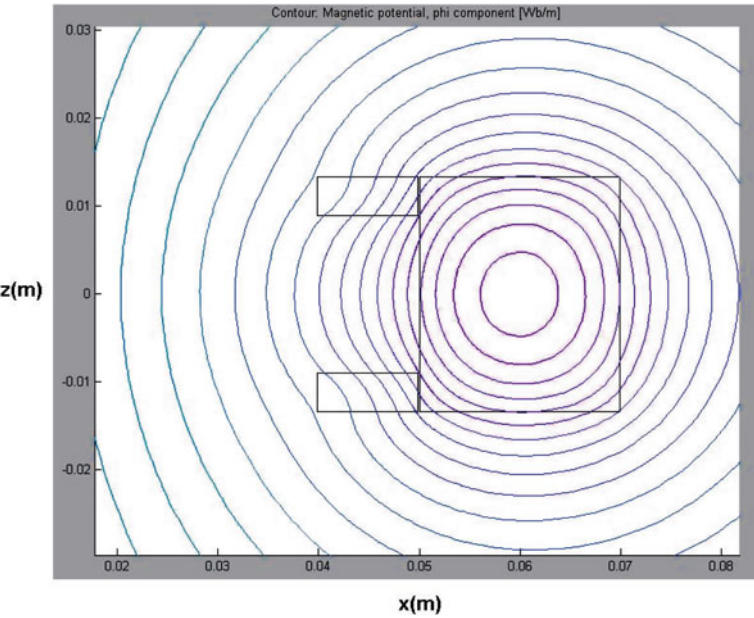


Fig. 4.11 Cross section view of a SMES coil with cancellation winding 1. The big block represents the coil, and the two small blocks represent the cancellation winding 1

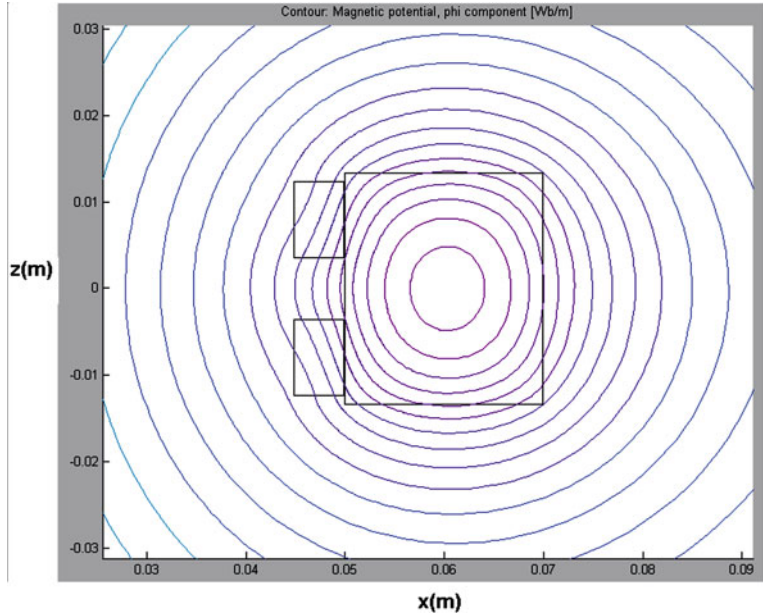


Fig. 4.12 Cross section view of a SMES coil with cancellation winding 2. The big block represents the coil, and the two small blocks represent the cancellation winding 2

Table 4.3 Comparison of coils with and without cancellation windings

	Stored energy (J)	Operation current (A)
No cancellation windings	863	418
Cancellation winding 1	739	423
Cancellation winding 2	719	426

field and increase the operating current, they behave like a ‘negative’ inductance to the SMES coil due to their opposite-direction current, thus the stored energy is reduced.

4.2.3 Optimisation with 4-mm-Width Tape

We can also use the other kind of tape made by Superpower, i.e. 4-mm-width tape. In this case the total length will be three times that of a 12-mm-width tape, since the width is one-third of it. Therefore the length of the 4 mm-width tape is 300-m.

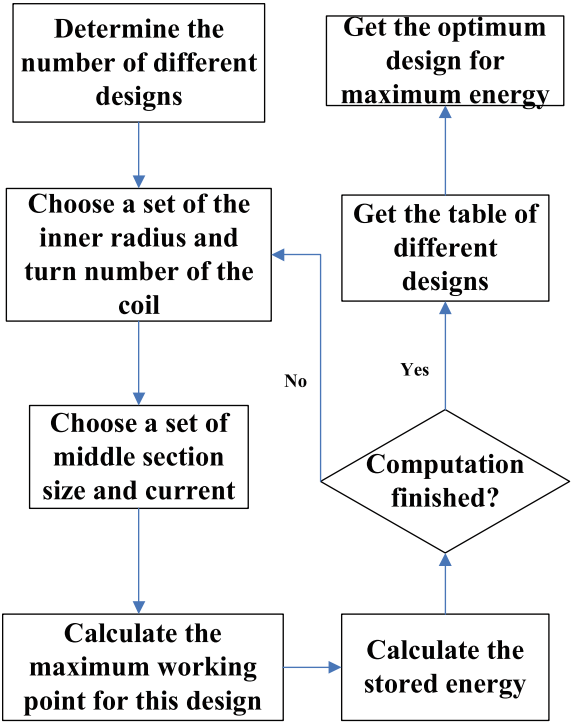
We still follow the optimisation algorithm as in Fig. 4.8. The optimisation result is shown in Table 4.4. Again, one-layer pancake design gives the maximum stored energy possible.

Since the maximum operation current is limited by the maximum perpendicular magnetic field which is located around the top and bottom surface of the coil, we

Table 4.4 Pancake coil design using 4-mm-width tape, giving maximum energy

Coil properties	Quantity
Inner radius	26 mm
Outer radius	122 mm
Coil height	4 mm
Conductor length	300 m
Turns	644
Inductance	72 mH
Operation temperature	22 K
Operation current	160 A
Stored energy	917 J

Fig. 4.13 Optimisation algorithm to achieve maximum energy



can increase the operation current in the middle section of the coil while decrease the operation current in the top/bottom section. This optimisation could potentially increase the stored energy. This will involve a multi-pancake coil design. There are four independent variables in this optimisation process, the coil inner radius, the coil width, the height and the current of the middle section. Firstly we choose a set of these four variables, then we work out the maximum operating current in the top and bottom section and eventually the stored energy. The flow chart of optimisation is shown in Fig. 4.13.

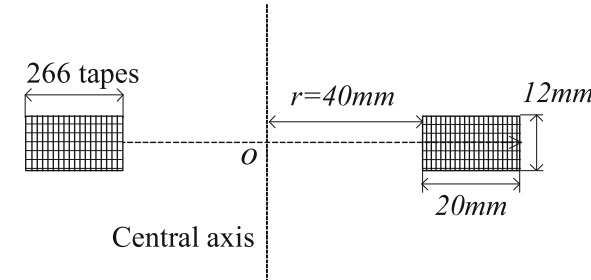
Table 4.5 Multi-pancake coil design giving maximum stored energy

Coil properties	Quantity
Pancake number	4
Inner radius	36 mm
Outer radius	92 mm
Coil height	16 mm
Conductor length	300 m
Turns per pancake	374
Inductance	72 mH
Operation temperature	22 K
I in the middle section	142.5 A
I in the top/bottom section	141.3 A
Stored energy	864 J

Table 4.6 Comparison of 4-mm-width and 12-mm-width tape designs

	12 mm	4 mm
Stored energy	863 J	917 J
Operation current	418 A	159 A
Tape length	100 m	300 m
Cost	\$ 9,500	\$ 195,000
Efficiency	0.091 J/\$	0.047 J/\$

Fig. 4.14 SMES coil final design



The optimisation result is presented in Table 4.5. Although we allow the currents vary in different pancakes, the result shows that the coil tends to need a uniform current to achieve the maximum stored energy.

Therefore, when 4-mm-width tapes is used, Table 4.4 gives the design to get the maximum energy.

4.2.4 Final SMES Coil Design

To compare the two different designs with different width tape, we get Table 4.6, from Table 4.6 we can see that although the 12-mm-width tape design will store energy 6% less than 4-mm-width tape design, its efficiency (energy/cost) is twice

the latter one. Therefore we will choose 12-mm-width tape design, which is shown in Table 4.2, to wind our SMES coil. Figure 4.14 shows the cross-section view of this design.

Reference

1. Superpower Inc. Technical documents. <http://www.superpower-inc.com>.46

Chapter 5

Modelling of Superconducting Pancake Coil

Superconducting¹ pancake coils can be used in a range of large scale applications—for example, Superconducting Magnetic Energy Storage (SMES), Superconducting Fault Current Limiter (SFCL), MRI, and so on [1–3]. Predicting AC losses are also very important for the applications of superconducting coils in machines [4–8]. Therefore an understanding of the electromagnetic behaviour of the superconducting pancake coils are important before using them in real applications. The magnetic field and current density distribution needs to be investigated thoroughly. The critical current of the coil needs to be predicted as well. Moreover, superconducting coils have a resistance in AC conditions, although they do not have any in DC conditions. Therefore calculating AC losses is necessary designing applications.

Since superconducting pancake coils are only recently available for research due to the development of commercial 2G HTS tapes, they have not yet been fully studied yet. Recently there are some research papers studying this topic [9–14]. One major difficulty in modelling these pancake coils is the significant computation resource needed. 2G HTS tapes all have a very high aspect ratio (around 0.01–0.2), moreover the pancake coils usually have a large number of turns (usually ≤ 100).

Clem et al has proposed to use an anisotropic homogeneous-medium approximation to model the pancake coils [15]. Starting from his original model, which

¹ Parts of this chapter are reprinted with permission from Weijia Yuan et al. (2010) AC losses and field and current density distribution during a full cycle of a stack of superconducting tapes. J Appl Phys 107(9):093909. ©2010 American Institute of Physics. Parts of this chapter are reprinted with permission from Weijia Yuan et al. (2010) Comparison of AC losses, magnetic field/current density distribution and critical currents of superconducting circular pancake coils and infinitely long stacks using coated conductors. Supercond Sci Tech 23(8):085011. ©2010 IOP Publishing Ltd. Parts of this chapter are reprinted with permission from Weijia Yuan et al. (2009) A model to calculate the AC loss of second-generation high temperature superconductor pancake coils. Supercond Sci Techn 22(7):075028. ©2009 IOP Publishing Ltd.

makes a number of simplifying assumptions, we have adapted it to a more precise model to describe the electromagnetic behaviour of the SMES coil.

5.1 Clem Model

The pancake coil is approximated as an infinitely long stack of tapes. These tapes are electrically insulated from each other and each tape carries the same transport current. This differs from a solid with the mean properties of the stack in that firstly there is a significant field penetrating parallel to the tapes, and secondly that the mean current density is uniform in the direction normal to the tapes if averaged across the tapes. In these circumstances we can define two regions. The outer edges will be penetrated by the field and carry the critical current density. The central region will carry a lower current density. In this central region the tapes have not been penetrated by the magnetic field and therefore the field must be parallel to the surface of the tapes [15]. Other numerical models have also proved this result [13, 14, 16]. Since the tapes are close together this field must be the same at all points on the surface of the tape and therefore the current density in each tape is constant as in Fig. 5.1, although it can vary from tape to tape. This is in contrast to an isolated tape where the field and current density decrease towards the centre of the tape. This means that if we know the current carried by the tape and the depth of penetration of the critical current we can find the current density carried in the unpenetrated region. Clem assumed a constant J_c and that the depth of penetration of the critical current was the same for all tapes. This penetration depth was treated as a variable parameter and adjusted to make the field in the unpenetrated region parallel to the tapes. He also assumed a single infinite wire.

As can be seen in Fig. 5.1, in the unpenetrated region (shaded) of length $2c$ the field has only one component. Therefore the field is uniform, and so is the current density. In this thesis we retain the approximation of a long wire, which is appropriate for a coil in which the radius is large compared with the cross-section of the turns. However we allow the depth of penetration to vary across the turns, and also use the Kim model to make the local current density in the critical region consistent with the local magnetic field. This latter is quite important as the field varies from zero at the centre to a relatively large value at the surface.

5.2 An Infinitely Long Stack of 2G HTS Tapes

5.2.1 Model Assumptions

Following Clem's assumption, we are still using an infinitely long stack to approximate a circular pancake coil. The difference between the infinitely long stack and circular coil will be discussed in Sect. 5.4

Fig. 5.1 Stack current density distribution. For the two regions of the stack, I is normal to the plane of the paper and B is parallel to the surface in the central region

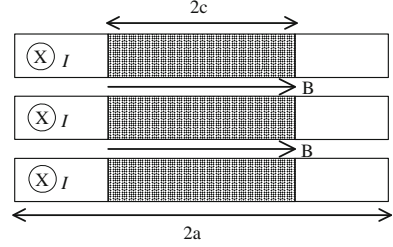


Fig. 5.2 Cross-section view of a stack of infinitely long tapes

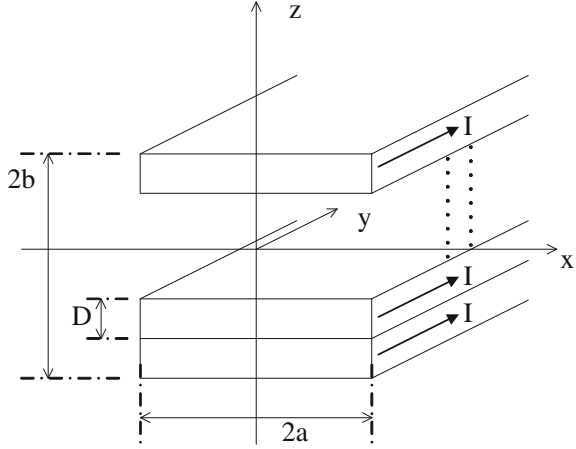


Figure 5.2 shows the cross-section view of a stack of infinitely long tapes carrying the same transport current. The width of the tape is $2a$, the thickness of each tape is D , and the height of the stack is $2b$, therefore there are $2b/D$ tapes in the stack.

Firstly, we assume that in the critical region $J_c(x, z)$ depends on the local $B_z(x, z)$. The perpendicular magnetic field has a much larger effect on the critical current of coated conductors than the parallel magnetic field, and we use Kim's model which gives us [17, 18],

$$J_c(x, z) = J_0 \frac{B_0}{B_0 + |B_z(x, z)|} \quad (5.1)$$

where B_0 is a material constant.

Secondly, the critical region is constrained by a curve rather than a straight line, i.e. we allow the unpenetrated width, $2c$, to vary as a function of z .

Let us assume the current in the middle region (the subcritical region) is $J_m(x, z)$. To make sure each tape in the pancake carries the same transport current I , we need to have $\int_{-a}^a J_y dx = I/D$. Therefore in the subcritical region of the stack:

$$J_m(z) = \frac{I/D - \int_{c(z)}^a J_c(x, z) dx}{2c(z)} \quad (5.2)$$

Fig. 5.3 Transport current density distribution in a stack of superconducting tapes

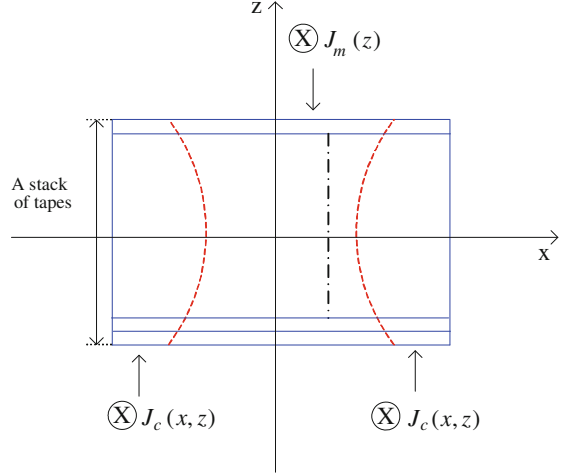


Figure 5.3 presents the current distribution in the stack of tapes.

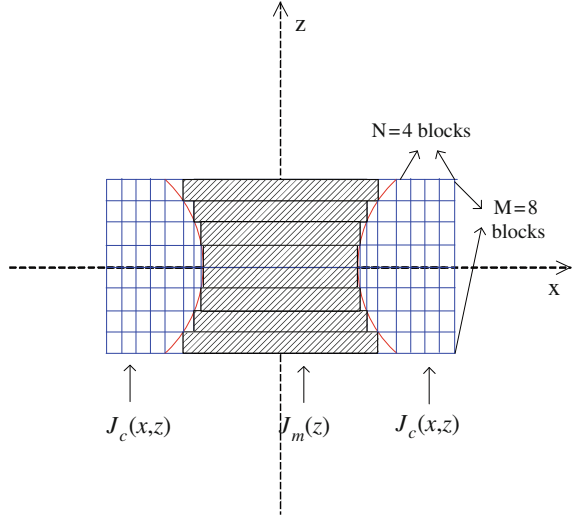
5.2.2 Solution Methodology for Transport Current Only

We assume the red dashed curves $c(z)$ in Fig. 5.3 above can be represented by the function $x = c(z) = \frac{c_2 - c_1}{b^2} z^2 + c_1$, where c_1 and c_2 are the x -coordinate values of the intersection points of the curve with the surfaces and the x -axis, respectively.

There are two numerical methods to solve this model. The first is to dynamically divide the cross section into rectangular blocks as shown in Fig. 5.4, with a uniform current density which varies with x and z in each block. Firstly we divide the stack into M equal sections along the z -axis by drawing $M - 1$ straight lines parallel to the x -axis. Secondly we divide the region from the intersection points of the parabola and the upper/lower boundary of the stack to the right/left boundaries of the stack into N sections. Finally we find the intersection points of the straight lines along the x -axis with the parabola, and plot straight lines parallel to the z -axis between the intersection points to divide the parabola region into blocks. We regard the blocks intersected by the parabola as the critical state boundary. The inner part within the parabola is considered as one block along the x -axis as the current density is uniform in this region. Details of the division are shown in Fig. 5.4 where $M = 8$ and $N = 4$. Since this is a dynamic division of the stack varying with different curves $x = c(z)$, it works very well even when the curvature of the parabola is small.

The second way is to use a fixed division method. Since the locations of the blocks are fixed, we can produce a look-up table for every computation which will save a lot of time, hence we can divide the cross section into smaller blocks and gain computation speed. Firstly we divide the cross section into M equal sections

Fig. 5.4 Dynamic division of a stack of superconducting tapes



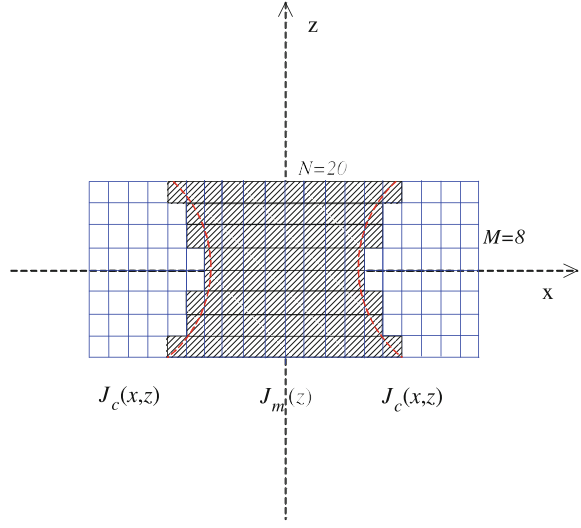
along the z -axis by drawing $M - 1$ equally spaced straight lines parallel to the x -axis. Secondly we divide the region into N equal sections along the z -axis by drawing $N - 1$ equally spaced straight lines parallel to the z -axis. We regard the blocks intersected by the curves as the critical state boundary. The inner part (including the blocks intersected by the red dashed curves) is the unpenetrated region, which is considered as one block along the x -axis since the current density is uniform in this region. However it still has M blocks along the z -axis, thus it has a current density as $J_m(z)$. The shaded area shows the inner blocks. The outer part is the critical region with the critical current density $J_c(x, z)$ varying with each block. A detailed division example is given in Fig. 5.5 with $M = 8$ and $N = 20$.

Although the dynamic division copes with extreme situations very well, i.e. when the penetration depth is too small or too large, generally its accuracy and computation speed is not as good as the fixed division method. Thus in this thesis, we will use the fixed division method.

Each block in Fig. 5.5 can be considered as a long conductor with a rectangular cross-section carrying a uniform current density J_y . The cross-section of the conductor lies in the $x - z$ plane and the conductor extends infinitely along the y axis. The conductor lies in the region $x_1 < x < x_2$ and $z_1 < z < z_2$. The vector potential and magnetic field at (x, z) produced by the current are [15, 19, 20]:

$$A_y = \frac{1}{2} \mu_0 J_y / 2\pi \cdot \left[\begin{aligned} & - (x - x_1)(z - z_1) \ln[(x - x_1)^2 + (z - z_1)^2] \\ & + (x - x_1)(z - z_2) \ln[(x - x_1)^2 + (z - z_2)^2] \\ & + (x - x_2)(z - z_1) \ln[(x - x_2)^2 + (z - z_1)^2] \\ & - (x - x_2)(z - z_2) \ln[(x - x_2)^2 + (z - z_2)^2] \end{aligned} \right]$$

Fig. 5.5 Fixed division of the stack cross section



$$\begin{aligned}
 & - (x - x_1)^2 \arctan\left(\frac{z - z_1}{x - x_1}\right) + (x - x_1)^2 \arctan\left(\frac{z - z_2}{x - x_1}\right) \\
 & + (x - x_2)^2 \arctan\left(\frac{z - z_1}{x - x_2}\right) - (x - x_2)^2 \arctan\left(\frac{z - z_2}{x - x_2}\right) \\
 & - (z - z_1)^2 \arctan\left(\frac{x - x_1}{z - z_1}\right) + (z - z_1)^2 \arctan\left(\frac{x - x_2}{z - z_1}\right) \\
 & + (z - z_2)^2 \arctan\left(\frac{x - x_1}{z - z_2}\right) - (z - z_2)^2 \arctan\left(\frac{x - x_2}{z - z_2}\right) \Big] \quad (5.3)
 \end{aligned}$$

$$\begin{aligned}
 B_x = \mu_0 J_y / 2\pi \cdot & \left[(x - x_1) \ln[(x - x_1)^2 + (z - z_1)^2] - (x - x_1) \ln[(x - x_1)^2 + (z - z_2)^2] \right. \\
 & - (x - x_2) \ln[(x - x_2)^2 + (z - z_1)^2] + (x - x_2) \ln[(x - x_2)^2 + (z - z_2)^2] \\
 & + 2(z - z_1) \arctan\left(\frac{x - x_1}{z - z_1}\right) - 2(z - z_1) \arctan\left(\frac{x - x_2}{z - z_1}\right) \\
 & \left. - 2(z - z_2) \arctan\left(\frac{x - x_1}{z - z_2}\right) + 2(z - z_2) \arctan\left(\frac{x - x_2}{z - z_2}\right) \right] \quad (5.4)
 \end{aligned}$$

$$\begin{aligned}
 B_z = \mu_0 J_y / 2\pi \cdot & \left[(z - z_1) \ln[(x - x_1)^2 + (z - z_1)^2] - (z - z_1) \ln[(x - x_2)^2 + (z - z_1)^2] \right. \\
 & - (z - z_2) \ln[(x - x_1)^2 + (z - z_2)^2] + (z - z_2) \ln[(x - x_2)^2 + (z - z_2)^2]
 \end{aligned}$$

$$\begin{aligned}
& + 2(x - x_1) \arctan\left(\frac{z - z_1}{x - x_1}\right) - 2(x - x_1) \arctan\left(\frac{z - z_2}{x - x_1}\right) \\
& - 2(x - x_2) \arctan\left(\frac{z - z_1}{x - x_2}\right) + 2(x - x_2) \arctan\left(\frac{z - z_2}{x - x_2}\right) \Big] \quad (5.5)
\end{aligned}$$

By summing the contributions from each block we can find A_y , B_x and B_z at every point in terms of the current density in the stack.

Since in Eq. 5.3 the expression A_y is the value relative to the centre of the rectangle, we need to subtract $A_y(0, 0)$ from the contributions from each block to guarantee A_y is zero at $(0, 0)$ in the stack.

To save computation time a grid of $A_y(x_1, x_2, z_1, z_2)$ and $B_z(x_1, x_2, z_1, z_2)$ values of each block as shown in Fig. 5.5 for unit current density was calculated and a look-up table was used to find the values for each computation.

Making J_c consistent with the local value of B_z and the total current in each tape equal to I leads to the following non-linear equations.

$$J_y = f(B_z) = \begin{cases} J_c(x, z) = J_0 \frac{B_0}{B_0 + |B_z(x, z)|}, & c(z) < |x| < a \\ J_m(z) = \frac{I/D - \int_{c(z)}^a J_0 \frac{B_0}{B_0 + |B_z(x, z)|} dx}{2c(z)}, & |x| < c(z) \end{cases} \quad (5.6)$$

$$B_z = f(J_y) = \sum_x \sum_z B_z(J_y) \quad (5.7)$$

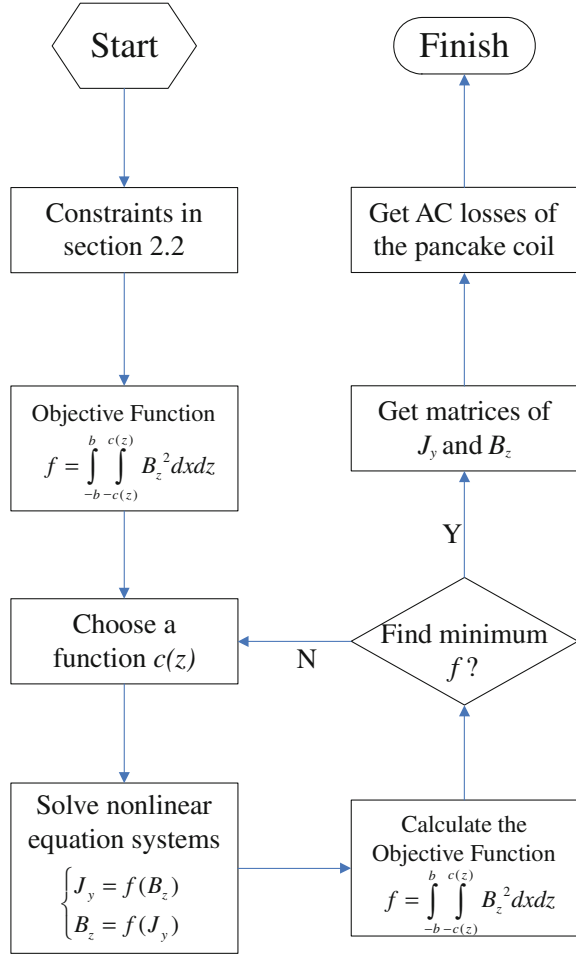
Assuming the critical region boundary is given by the function $x_1 = c(z) = \frac{c_2 - c_1}{b^2} z^2 + c_1$, we can put it into the nonlinear equation system above, solve the equation systems to get matrices of J_y and B_z , and then get the magnetic field and current density distribution of the stack of tapes.

In order to be consistent with the assumption that B_z is 0 in the subcritical region, we define an objective function $f = \int_{-b}^b \int_{-c(z)}^{c(z)} B_z^2 dx dz$. To make B_z approximately zero we minimize this function by varying c_1 and c_2 . Figure 5.6 shows the flow chart of the solution process.

Having found the $c(z)$ which minimises the objective function $\int_{-b}^b \int_{-c(z)}^{c(z)} B_z^2 dx dz$, we can get the magnetic field and current density distribution of the stack of tapes. We have assumed the tapes start from the virgin state, which means that the current is raised from zero to I . We neglect losses due to B_x in the middle sections.

There are several ways to find the loss given the field distribution. The most fundamental is to find the flux between point x and the point where B goes to zero. The change in this due to a change in current is proportional to the electric field, and integrating $E \cdot J_c$ across the sample gives the instantaneous loss. This is then integrated with respect to the current from zero to the maximum current to give the total loss on first charging the magnet. This needs a triple integration which is time consuming.

Fig. 5.6 Solution process flow chart



Since the first two steps involve first an integration and then a differentiation of the same function, albeit with respect to different variables, it is possible to reduce the calculation to two integrations, which is also the effect of using the Poynting vector, although in the case we must subtract the magnetic energy in the system to get the loss.

A much simpler Eq. 5.8 based on the force on the flux lines as they move in was proposed by Claassen [21] and used in references [22, 23].

$$Q_0 = 2J_c \int_{c(z)}^a \int_{-b}^b |B_{z-peak}|(a-x) dx dz \quad (5.8)$$

Claassen's paper shows that when J_c is constant Eq. 5.8 is equivalent to the integration of $E \cdot J_c$ [15, 21]. However we found that the expression is still true even if J_c is a function of B_z provided J_c is moved inside the integral as in Eq. 5.9. The proof for a general $J_c(B)$ for a slab is shown in Appendix A.

$$Q_0 = 2 \int_{c(z)}^a \int_{-b}^b J_{c-peak} |B_{z-peak}| (a - x) dx dz \quad (5.9)$$

Equation 5.9 is a significant improvement since we can get the initial hysteretic loss only using the final state when I is at the maximum and this saves computation time.

When J_c is constant, the AC loss Q per unit length in a full cycle will be four times the initial magnetisation [24], i.e. $Q = 4Q_0$. Unfortunately this is not precisely true when J_c varies with B . However calculation shows that the error is only between 5 and 10% [23], which will also be shown in Sect. 5.3, we still use $Q = 4Q_0$ to approximate the AC loss in a full cycle.

If we multiply Q by the mean circumference of the pancake coil, we can get the AC loss per cycle of the coil.

5.2.3 Extension of Model to Stack in Only Magnetic Field

It is not difficult to adapt this model to simulate the situation of a stack of superconducting tapes magnetised in an applied uniform magnetic field B_z . In the magnetisation process, there will be no transport current in the tapes but only a magnetisation current which has a different sign in the two critical regions. In the middle subcritical region, J_m will be zero since the applied field has not penetrated here. We just need to change the nonlinear equation system to

$$J_y = f(B_z) = \begin{cases} J_c(x, z) = J_0 \frac{B_0}{B_0 + |B_z(x, z)|}, & c(z) < |x| < a \\ 0, & -c(z) < x < c(z) \\ J_m(z) = J_0 \frac{B_0}{B_0 + |B_z(x, z)|}, & -a < |x| < -c(z) \end{cases} \quad (5.10)$$

$$B_z = f(J_y) = \sum_x \sum_z B_z(J_y) \quad (5.11)$$

Again we use Eq. 5.9 to derive the initial magnetisation loss.

Table 5.1 Configuration of an infinitely long stack to approximate the pancake coil

Coil Properties	Quantity
Inner radius	50 mm
Outer radius	80 mm
Coil height	12 mm
Conductor length	100 m
Turns	133
Operation current	514 A
Operation temperature	22 K

5.2.4 Calculation Examples

5.2.4.1 Stack Carrying Transport Current

We plan to operate the pancake coil at 22 K, thus we are using Eq. 4.2 to describe $J_c(B_z)$ function, which is shown here again,

$$J_{c,22K} = J_{0,22K} \times \frac{B_{0,22K}}{B_{0,22K} + |B_z|} \quad (5.12)$$

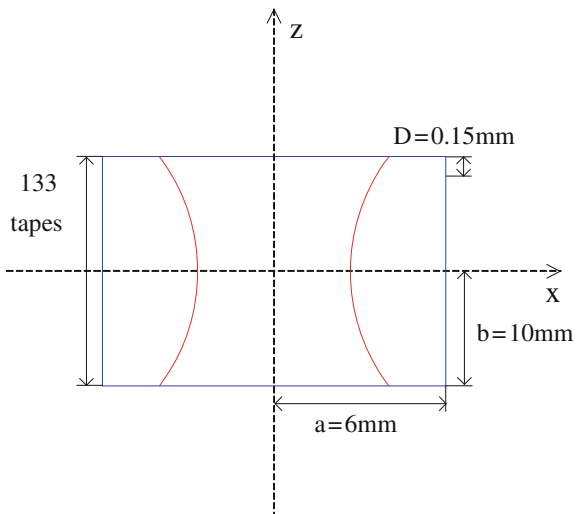
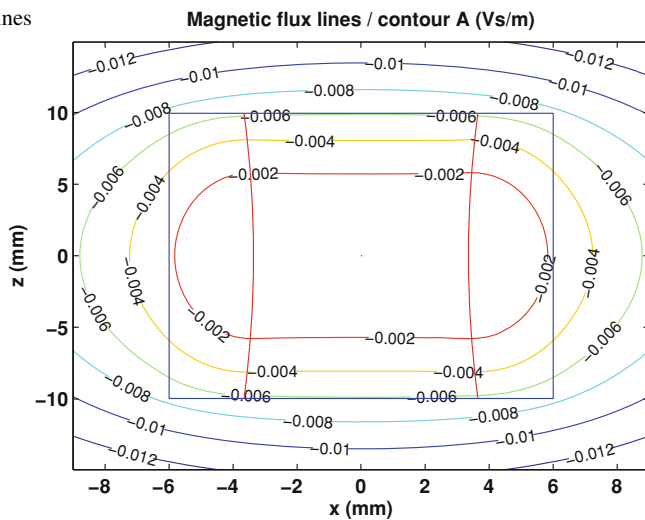
where $J_{0,22K} = 6.58 \times 10^8 \text{ A/m}^2$, $B_{0,22K} = 1.49 \text{ T}$.

The coil configuration is shown in Table 5.1. Tape thickness also includes the insulation layer. The coil size used in this section is slightly different from Table 4.2, but it is still a single layer pancake using super-power's 12 mm-width tape.

All the necessary parameters needed for calculation as well as the configuration is shown in Fig. 5.7.

To gain an accurate solution with an acceptable computation speed, we divide the coil into blocks using the fixed-division method with $M = 10$ and $N = 200$. The calculation results are shown in Figs. 5.8, 5.9, 5.10, 5.11, 5.12:

From Fig. 5.8 we can see that almost all magnetic flux lines are parallel to the tapes in the subcritical region as required. Figure 5.9 shows B_z at different heights of the stack, the values are nearly zero in the whole subcritical region. Figure 5.10 shows the current density across the stack at the same three levels. Figures 5.11 and 5.12 show B_z and J_y in the stack. It is very clear that the further the critical current penetrates into the middle subcritical region, the less is the local B_z , thus the more J_c is flowing. At the boundaries of the critical and subcritical regions, the stack will force the current to drop to a much lower value of J_m as the magnetic flux lines become parallel to the tapes in the middle subcritical region. It is interesting to see that the boundaries of the subcritical regions curve inwards at the centre rather than outwards as in the case of an isotropic bulk super-conductor [25, 26]. This is because B_z in the middle of the stack in the critical region will be higher than that around the top and bottom, the critical current densities will be less, hence the critical region will penetrate more to guarantee each tape carries the same transport current.

Fig. 5.7 Coil configuration**Fig. 5.8** Magnetic flux lines for the stack of tapes

Based on the results above, we can calculate a full cycle AC loss of this stack with a 514 A (the peak value) AC current as 147.2 J/cycle/m.

In order to understand whether the number of subdivisions of the stack has a large influence on the hysteretic losses, we completed two more calculations with a finer division $M = 20$ and $N = 200$. The results are 146.4 J/cycle/m and 144.2 J/cycle/m. The results are similar to those with the coarser division. We conclude that the division $M = 10$ and $N = 200$ is accurate enough for the calculation.

Fig. 5.9 B_z at different levels of the stack

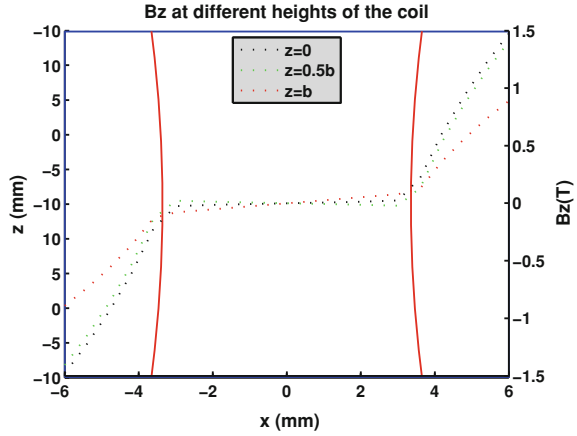
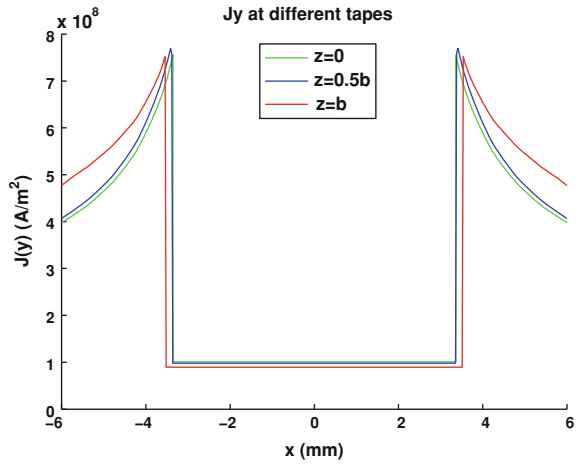


Fig. 5.10 Current density at different levels of the stack



The model fails when critical currents penetrate into the centre of the middle tape of the stack, this marks the critical current of the stack. For this coil the critical current is 803 A. Figures 5.13 and 5.14 give the current distribution of the coil at the critical current.

This can be compared with two cruder methods of estimating the critical current of the coil. Firstly if we assume that the stack behaves as a solid conductor carrying $J_c(B)$ at all points, but with the local J_c consistent with the flux density at that point, the critical current $I_{c_consistent}$ will be 1324 A. Our model shows that the critical current is significantly smaller than this, since the critical current is reached in the central tape while the outer tapes are carrying less than the critical value.

A lower limit to I_c is obtained by assuming a constant and uniform critical current determined by the maximum value of B_z in the coil by Kim model as in Eq. 5.12. This gives a value of 643 A which is 80% of our value. (In the first part

Fig. 5.11 Contour of B_z in the coil

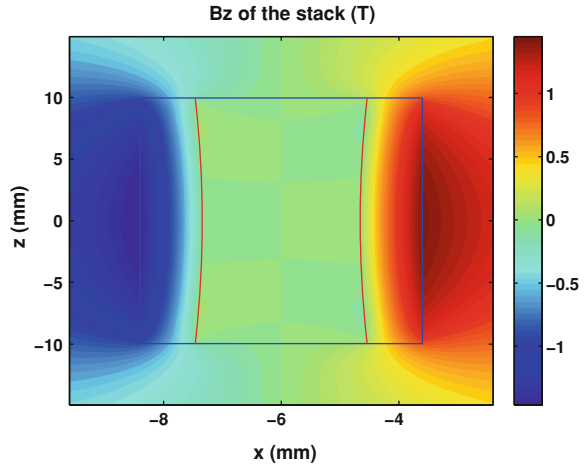
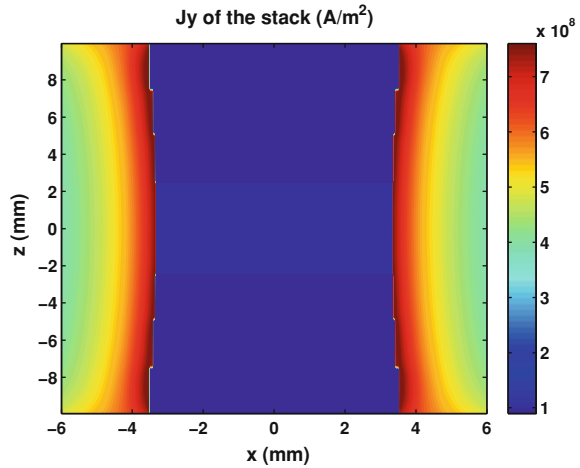


Fig. 5.12 Contour of J_y in the coil



of this paper we used an 80% safety margin on this value as our maximum transport current, i.e. 514 A). We name this critical current as $I_{c_B_{max}}$.

It is also interesting to understand how the AC losses and penetration depth of critical currents will respond to the change of transport currents.

We define the penetration depth $d = 0.5(c_1 + c_2)$, where c_1 and c_2 are x -coordinate values of the intersection points of the curve with the top/bottom lines and the x -axis.

We change the transport currents from 0 to 800 A (peak value), calculate the AC loss in a full cycle, and normalize the penetration depth to half the width of tapes. The results are in Figs. 5.15 and 5.16.

For comparison we also calculated the losses given by the Norris strip model based on different critical currents: $I_c = 803$ A predicted by our model,

Fig. 5.13 Contour of J_y in the stack at critical current

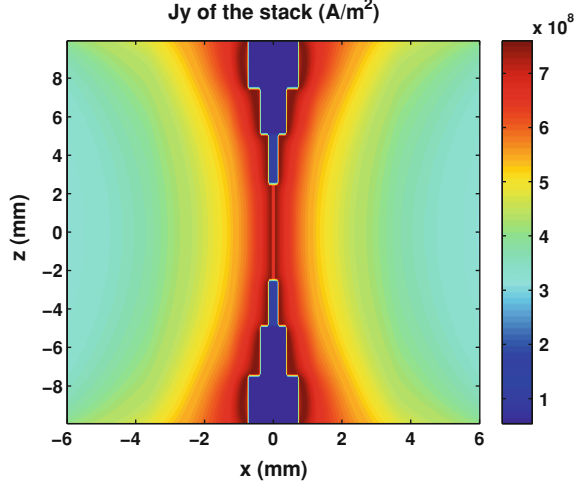
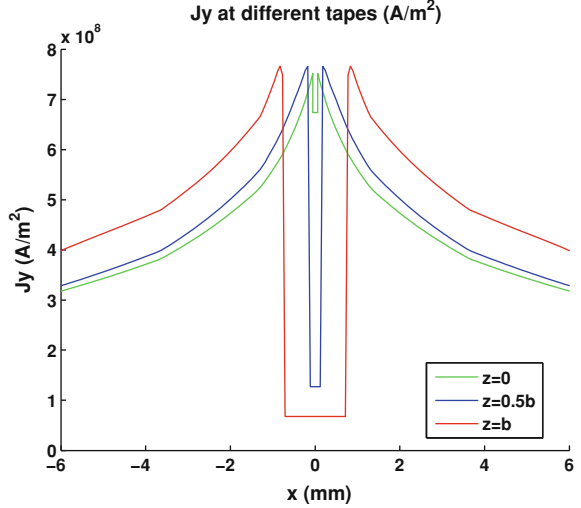


Fig. 5.14 J_y at different levels in the stack at critical current



$I_{c_consistent} = 1324$ A and $I_{c_B_{zmax}} = 643$ A. Figure 5.17 compares the results. We find that Norris predictions based on different critical currents are not close to the values given by our model. Thus it does not seem possible to define a suitable average J_c for a Norris strip to calculate AC losses.

5.2.4.2 Stack in Magnetic Field

We consider the same stack as in Sect. 5.2.4.1, apply a 1 T B_z to it. Then we divide it with $M = 10$ and $N = 200$. After calculation we get following figures. From Figs. 5.18, 5.19, 5.20, 5.21 and 5.22 we can see that the calculated results agree

Fig. 5.15 Full cycle AC loss of stack with different transport currents

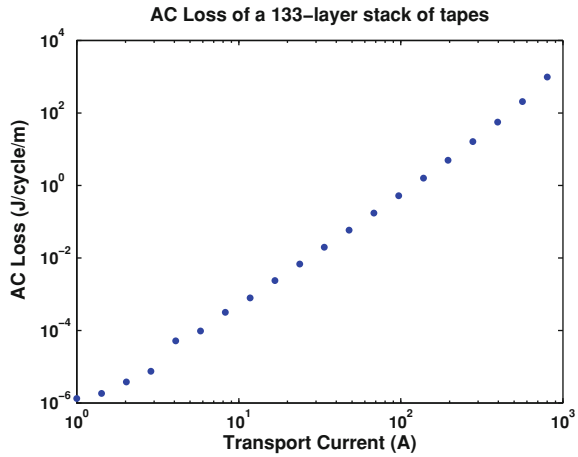
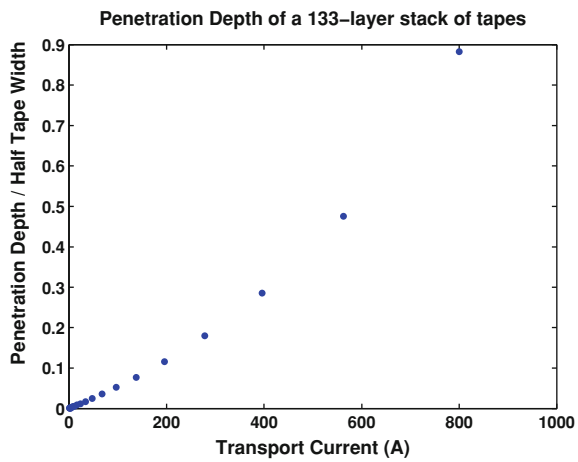


Fig. 5.16 Penetration depth of stack with different transport currents



well with the assumptions: B_z is zero in the middle subcritical region, J_c has a different sign at two critical regions, and J_y is zero in the middle subcritical regions. The initial magnetisation loss of this stack from virgin state is 29.1 J/m.

Again we can change the applied magnetic field and plot the magnetisation losses and penetration depth versus the applied field curves for the same stack of tapes. The magnetisation loss in the figures below is the initial magnetisation loss from virgin state. From Fig. 5.23 we see that the loss increases as the cube of the applied field, and Fig. 5.24 shows that the penetration of the field is approximately linear.

Finally, we present how the initial magnetisation losses and penetration depth changes with the number of tapes in the stack.

This time we will change the geometry of the pancake coil, namely the number of tapes in the stack. All other parameters and configurations are kept the same,

Fig. 5.17 Comparison of AC losses of the stack between our model and Norris strip model

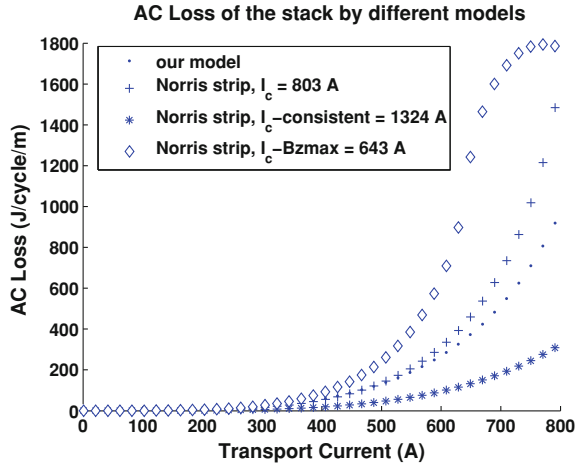
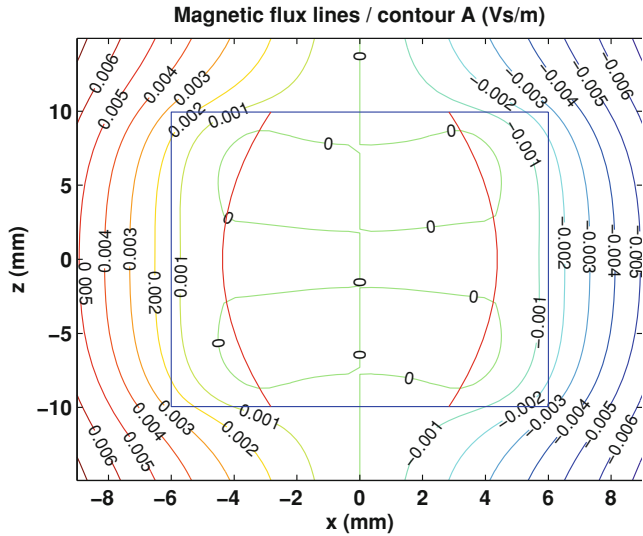
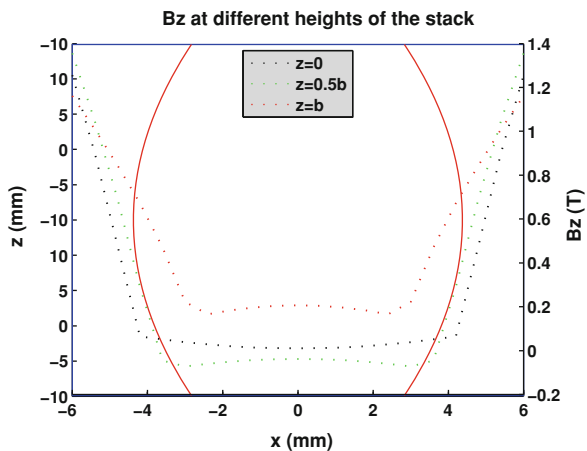
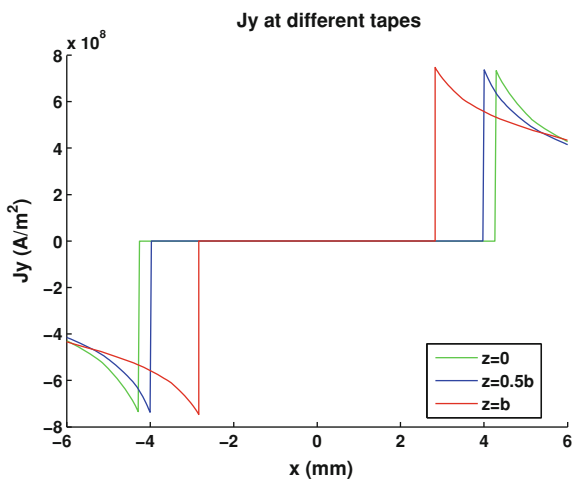


Fig. 5.18 Magnetic flux lines of the stack of tapes



except that since the tape thickness is the same the stack thickness is proportional to the number of tapes. Figure 5.25 gives the initial magnetisation hysteretic loss at a fixed applied field B_z with a different number of tapes, Fig. 5.26 presents how the penetration depth changes.

Since a field of 1 T is considerably more than that required to penetrate a single tape, for small numbers of tapes the loss rises linearly with the number of tapes and the loss per unit volume is large. At around 20 tapes the tapes shield each other so that the shielding on adding more tapes compensates for the extra loss in the added tapes. At 80 tapes the cross section of the stack is square and beyond this it begins

Fig. 5.19 B_z at different levels of the stack**Fig. 5.20** Current density at different levels of the stack

to behave as a slab to which the Bean model can be applied. The loss is proportional to the wide surface area of the slab and therefore again rises linearly with the number of tapes, but at a much slower rate. Our calculation shows that for a very large number of tapes the proportion of the loss in half the slab over the surface area is 203 J/m^2 . Equation A.12 in Appendix A gives a general expression for the loss of a half slab and for the Kim model at 1 T this is 202 J/m^2 for the initial charging. We can see from Fig. 5.25 that our model gives a very close result to the slab model.

Our calculation result shows that if the number of tapes is more than 1000, the normalised penetration depth will stabilise around 0.247. It is interesting to compare the penetration depth given by this model with the Bean model with J_c as a function of B_z . In a slab, if we use Eq. 5.12 for the critical current density, the

Fig. 5.21 Contour of B_z in the coil

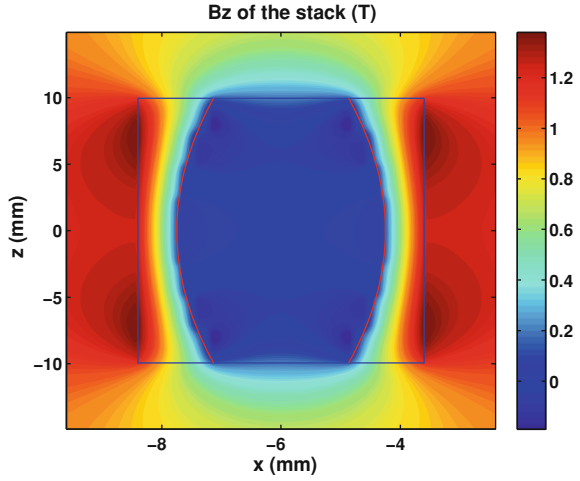
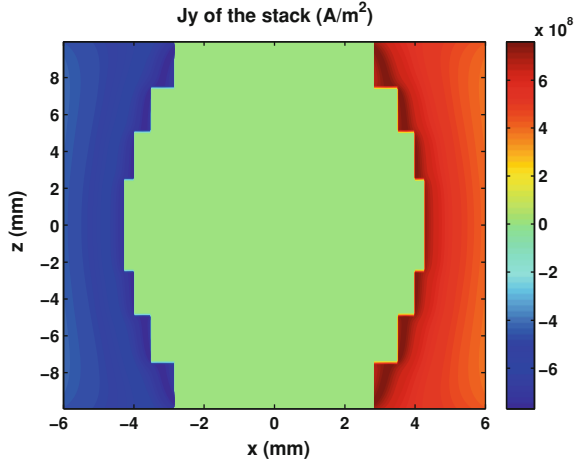


Fig. 5.22 Contour of J_y in the coil



flux density is given by $dB_z/dx = \mu_0 J_c(B_z)$. By integration we find that the penetration depth $d = (B_0 B_{z_applied} + 0.5 B_{z_applied}^2) / \mu_0 J_0 B_0$. At $(B_{z_applied}^2) = 1$ T the ratio to the half width is 0.227, compared to 0.247 given by our model. The difference is because the critical boundary in the Bean model is a straight line as opposed to a curve in our model. The 8% difference between the results is acceptable. Thus if the stack has more than 1,000 tapes, we could use an average critical current density to estimate the penetration depth by the Bean model if we want to take into account the variation of J_c with B_z .

It is worth pointing out that although we did not divide the stack into the number of tapes (i.e. 133 in this section) along the z -axis, the model can still guarantee each tape carries the same current since $\int_{-a}^a J_y dx$ is constant along the width direction of tapes.

Fig. 5.23 Magnetisation loss of the stack for different applied fields B_z

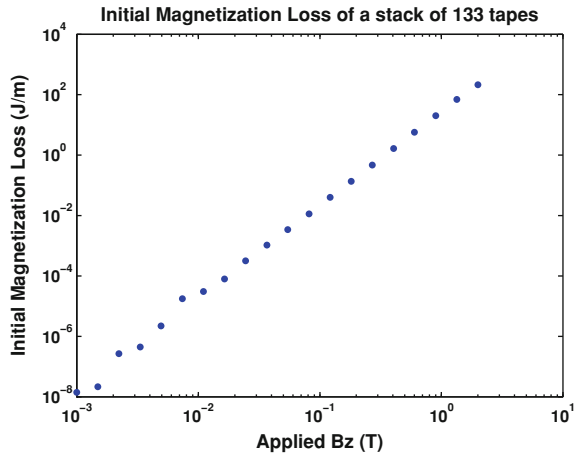
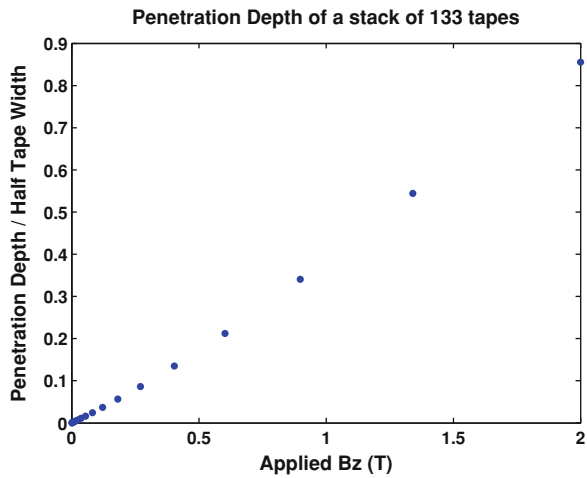


Fig. 5.24 Penetration depth of the stack for different applied fields B_z



5.2.5 Discussion

The calculated results are consistent with the assumptions and also present some interesting features. The magnetic flux lines must be parallel to the wide face of superconducting tapes in the subcritical region, B_z in this region is nearly zero everywhere. The boundaries of the subcritical region curve towards the centre of the stack, since B_z is larger in the centre than that in the top and bottom of the stack, therefore it can penetrate more in the middle. In the critical region, the further the critical current penetrates into the centre, the larger it is due to the lower local B_z . However, it is forced drastically down at the boundaries of the subcritical region. If extended beyond the critical current, one of the tapes will be fully penetrated, when the model fails, but this makes it easy to predict the critical

Fig. 5.25 Magnetisation loss of the stacks with different number of tapes

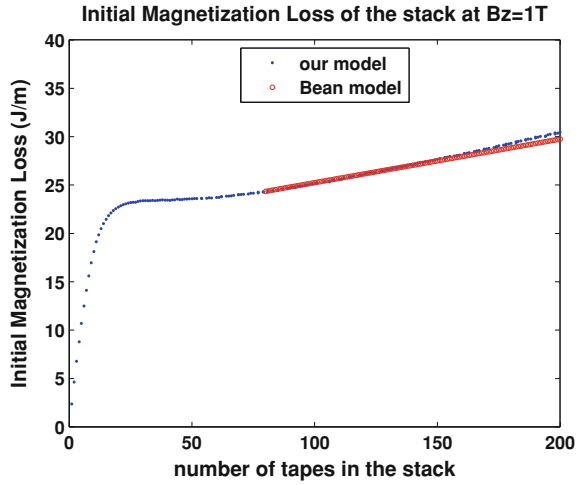
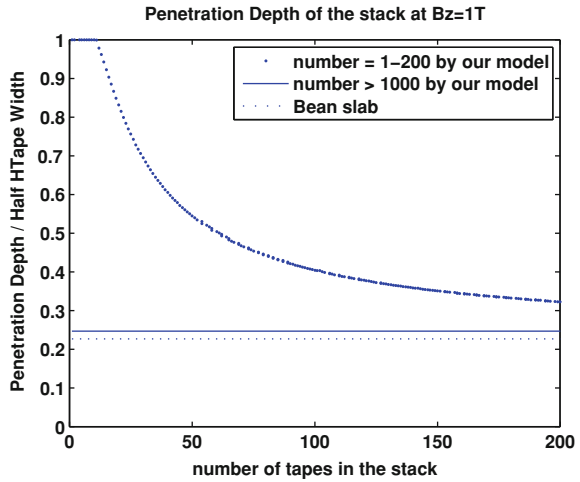


Fig. 5.26 Penetration depth of the stacks with different number of tapes



current which is significantly different from the value predicted assuming full penetration.

Our model predicts a critical current of 803 A, while if we assume there is no subcritical region and the critical current depends on the local magnetic field, the value is 1,324 A. The difference is due to the fact that in our model, when the middle tape is fully penetrated the critical current is reached, while there are current densities much smaller than critical current densities in the top and bottom tapes. However, in the other model the critical current is reached when all the tapes are fully penetrated. This comparison shows that our model is safer as it predicts a more conservative value of the critical current. Another critical current is given if the stack carries a uniform current density determined by the maximum perpendicular field, the value is then 643 A.

For comparison the AC losses was also calculated for the Norris strip model carrying different critical currents. We find that Norris predictions based on different critical currents are not close to values given by our model. Thus it does not seem possible to define a suitable average J_c for a Norris strip to calculate AC losses.

Based on the assumptions above, we calculated the case where the stack carries no transport currents but induced currents in an applied field B_z . In this case the boundaries of the subcritical region curve outward, rather than inward, as in the transport current case. This is partly because the tape in the centre is shielded from surrounding tapes so it is difficult for the applied field B_z to penetrate it. When the applied field B_z is far from large enough to penetrate the whole stack, the initial magnetisation loss goes up as the cube of the applied field as predicted by the simple Bean model.

When the number of tapes is small the applied field is enough to penetrate them, the initial magnetisation loss will increase rapidly with the number. If the field cannot penetrate the stack, which happens for larger numbers of tapes, the shielding effect will compensate for the extra loss in the added tapes. From when the cross section of the stack is square it will begin to behave as a Bean slab. The penetration depth will gradually become stable as the number of tapes increases to a large value. In this case, we can then use the Kim expression to calculate the loss and the penetration depth with the Bean model.

5.3 Magnetic Field and Current Density Distribution Over Full AC Cycle

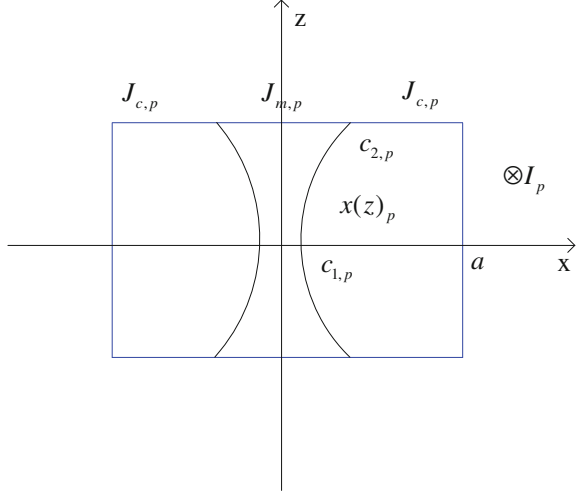
In Sect. 5.2 we only calculated the distribution of magnetic field and current densities in the coil at a specific time point, i.e. when the transport current or applied field is at maximum. This section presents how the distribution of magnetic field and current densities changes in a full AC cycle, which is very important for application. Moreover, this presents results for AC losses calculated by two different methods. In the first method it is calculated step by step over the full cycle, which is based on the analysis in this section. The second method is using Eq. 5.18 which is also discussed in Sect. 5.2.4. In this method only one point is used and this is when the transport current or applied field is at a maximum. This section demonstrates that the second computationally efficient method gives a good approximation.

We are stilling using an infinitely long stack to approximate the coil. The difference between the infinitely long stack and circular coil will be discussed in Sect. 5.4

5.3.1 Stack Over Full Cycle With Only AC Transport Current

We consider the case with only AC transport currents first. Due to symmetry we just need to consider a half cycle, we can take the process from the positive peak transport current to the negative peak transport current, for instance.

Fig. 5.27 Current density distribution of the stack with peak positive current I_p , equal to the integration of the current density across the stack



We can use the assumptions in Sect. 5.2 and compute the current distribution when the positive transport current is at its peak I_p as shown in [22]. Figure 5.27 shows the current distribution when I_p is firstly applied. The critical boundaries $x(z)_p$ are the parabolae with solid lines, $J_{c,p}$ and $J_{m,p}$ flow in the critical and sub-critical regions, respectively. If a transport current I is applied, we regard the decrease amount of the current from the positive peak I_p as a negative transport current $-(I_p - I)$, and assume this new current will also get a similar solution by our model in Sect. 5.2, i.e. negative current densities $-J_c - J_{c,p}$ will be in the new critical region, much lower negative current densities $-J'_m$ will be in the new sub-critical region to make sure the total negative transport current is $-(I_p - I)$ as shown in Fig. 5.28. The new critical boundaries are the dotted parabolae $\pm x(z)$. Thus we can get

$$-J'_m = \frac{(I - I_p)/D - 2 \int_{c(z)}^a (-J_c - J_{c,p}) dx}{2c(z)} \quad (5.13)$$

This new distribution of current densities should also follow the assumption that the perpendicular magnetic field is zero in the sub-critical region.

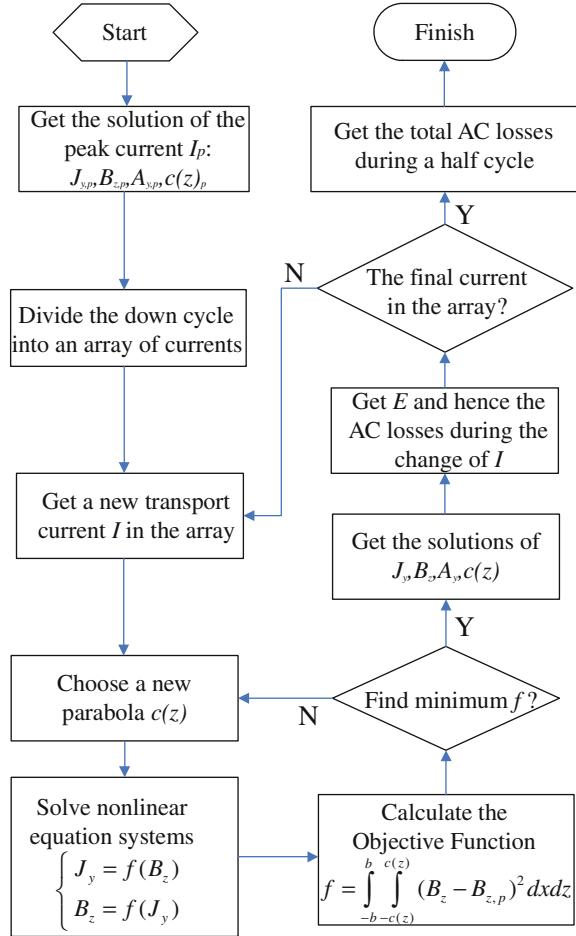
We can compute the current distribution for any current I in the half cycle by adding the solutions shown in Figs. 5.27 and 5.28. This is illustrated in Fig. 5.29. There are three different regions in Fig. 5.29. The most central region within $\pm x(z)_p$ is the sub-critical region. The region $x(z) < |x| < a$ is the new penetrated region when the current is going down. The region $x(z)_p < |x| < x(z)$ is the old penetrated region, this region is penetrated when the current is at maximum, but not yet penetrated by the new critical region after the current is going down. Thus the current distribution over the stack cross-section is as follows:

Figure 1 shows a 2D coordinate system with a horizontal x-axis and a vertical z-axis. A rectangular region is defined by the boundaries $x=0$, $x=a$, $z = -J_c - J_{c,p}$, and $z = -J_c - J_{c,p} - J'_m$. The region is divided into two parts by a dashed curve $x(z)$. The left part is labeled c_1 and the right part is labeled c_2 . A current source I_p is indicated by a circle with a dot at the bottom center.

$$J_y = \begin{cases} -J_c(x, z) & x(z) < |x| < a \\ J_{c,p} - J'_m & x(z)_p < |x| < x(z) \\ J_{m,p} - J'_m & |x| < x(z)_p \end{cases} \quad (5.14)$$

Therefore in the half cycle of a AC transport current, we have the negative critical current densities in the new penetrated region where $x(z) < |x| < a$. Since the negative current $-(I_p - I)$ does not produce a perpendicular magnetic field in old critical and sub-critical region constrained by $\pm x(z)$, the total magnetic field there should be the same as in the solution of the positive peak current. We need to change the solution process in Sect. 5.2.4 and [22] to Fig. 5.30.

Fig. 5.30 Solution process of the coil model over a half cycle



To get the complete solution of a transport current I in the half cycle, first we need to get the solution with the peak positive transport current. Then we use the analysis of the equivalent negative current to get the inter-relation function of J_y and B_z with I in the stack. We search for a particular parabola $c(z)$ to make the change of B_z in the sub-critical and old penetrated regions between $\pm x(z)$ become the minimum. After finding $c(z)$ we can get the distribution of J_y and B_z and thus the final solution.

To get the precise total AC losses during the half cycle we need to divide the AC transport current going from the positive to the negative peak into an array with n elements, $I_1, \dots, I_i, I_{i+1}, \dots, -I_n$, where $I_1 = I_p$ and $I_n = -I_p$. In this array the neighbouring points need to be very close to each other. Then we find and store solutions of all the currents in the array. The AC losses during the change between two neighbouring currents I_i and I_{i+1} will be,

$$\begin{aligned}
\Delta Q_i &= \int_{I_i}^{I_{i+1}} \int E J_i dtdS = J_i \int_{I_i}^{I_{i+1}} \int E dtdS \\
&= J_i \int_{I_i}^{I_{i+1}} (A_{i+1} - A_i) dS
\end{aligned} \tag{5.15}$$

where E is the electric field, J the current density, and A the vector potential.

Thus the total AC losses in a full cycle will be $2 \sum_{i=1}^n \Delta Q$. We call this method the electric field method, and this gives the AC losses in a full cycle computed step by step.

Another method only requires one solution when the current or magnetic field is at a maximum. It is to assume the AC losses in a full cycle will be four times that of the initial quadrant,

$$Q = 4 \times 2J_{c-p} \int_{c(z)_p}^a \int_{-b}^b |B_{z,p}|(a-x) dx dz \tag{5.16}$$

Where J_{c-p} and $B_{z,p}$ represent the critical current density and magnetic field when the applied current or magnetic field is at the peak value.

Equation 5.16 is given in [21]. However, it assumes that J_c is independent of field. We demonstrate in Appendix A that if J_c is field dependent it can be moved into the integral as in Eq. 5.17 to calculate the losses in the initial quadrant. Thus the losses in the initial quadrant are,

$$Q_{\text{quadrant}} = 2 \int_{c(z)_p}^a \int_{-b}^b J_{c,p} |B_{z,p}|(a-x) dx dz \tag{5.17}$$

To get a quick estimation, we can use the value $4Q_{\text{quadrant}}$ as the total AC losses in a full cycle, therefore the total losses in a full cycle is,

$$Q' = 4 \times Q_{\text{quadrant}} = 4 \times 2 \int_{c(z)_p}^a \int_{-b}^b J_{c,p} |B_{z,p}|(a-x) dx dz \tag{5.18}$$

However, the real AC losses in a full cycle will not be simply $4Q_{\text{quadrant}}$, although the error is small. We will quantify this error in the following calculation and demonstrate $4Q_{\text{quadrant}}$ is a pretty good and quick method to give an estimate of AC losses for engineering application. Due to symmetry, we only need to consider a half cycle, for example the half cycle from the positive peak to the negative peak.

Fig. 5.31 Magnetic current density distribution of the stack with peak positive field B_p

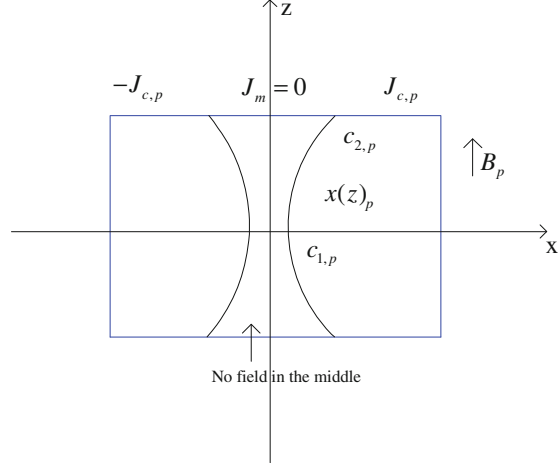
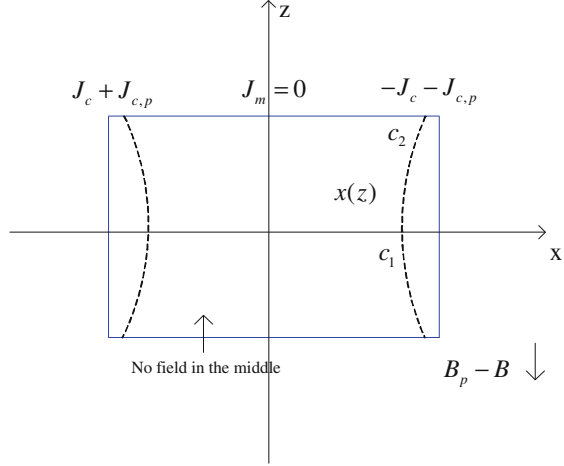


Fig. 5.32 Current density distribution of the stack with negative field $B_p - B$



5.3.2 Stack Over Full Cycle With Only AC Applied Fields

It is not difficult to adapt this model to analyse a stack only in an AC applied field. As in Sect. 5.3.1 we find the solution when the applied field is at maximum B_p as shown in Fig. 5.31. The critical current densities have opposite directions on both sides of the critical region. Due to symmetry, there will be no magnetic field in the sub-critical region. Then we find a second solution for $-(B_p - B)$ as shown in Fig. 5.32. By adding solutions in Figs. 5.31 and 5.32 we can get the complete distribution of current densities for a magnetic field B as in Fig. 5.33. Finally we follow the solution process in Fig. 5.30 to get the AC losses in the half cycle.

Fig. 5.33 Total current density distribution of the stack with applied field B

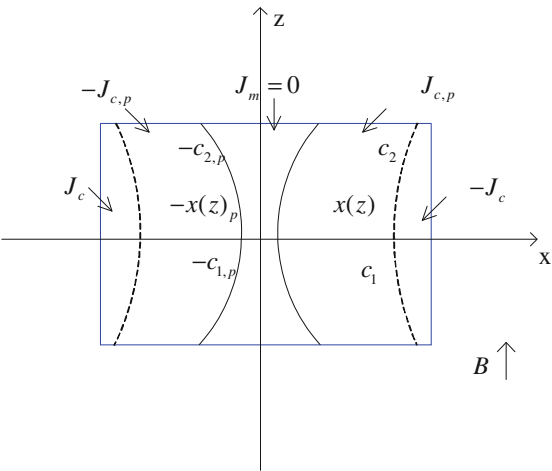


Table 5.2 Pancake coil configuration

Configuration	Quantity
Tape width	12 mm
Tape thickness	0.15 mm
Inner radius	40 mm
Outer radius	80 mm
Number of turns	266

5.3.3 Configuration of the Pancake Coil

We are using the same design as optimised in Table 4.2. For convenience, the configuration of the coils is summarised again in Table 5.2. Tape thickness also includes the insulation layer. Figure 5.34 shows how the coil is approximated as an infinitely long stack of tapes:

5.3.4 Stack With AC Transport Current Only

5.3.4.1 Constant J_c

To validate our model, we begin with a simple case, i.e. we assume J_c has a constant value $4.44 \times 10^8 \text{ A/m}^2$ across the stack but not varies as in Eq. 5.12. Then we put in a transport AC current with the peak value 500 A. The half cycle from the positive peak 500 A to the negative peak -500 A is divided into an 20-element equally spaced array. We present the solutions at four points during the half cycle in Figs. 5.35, 5.36, 5.37, 5.38, 5.39 and 5.40. Since J_c has a constant value in the

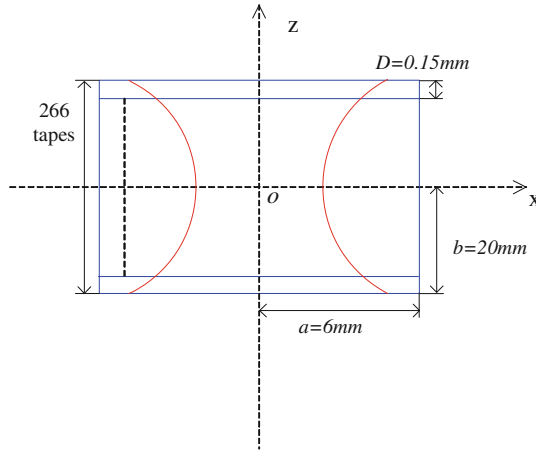


Fig. 5.34 Configuration of an infinitely long stack of tapes to approximate the pancake coil

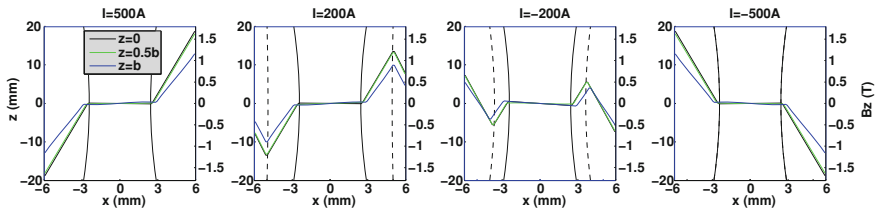


Fig. 5.35 B_z at different levels in the coil during the half cycle (I from 500 to -500 A). The parabola with solid lines are the critical boundaries at the peak current. The parabola with dotted lines are the new critical boundaries in the half cycle. The coloured lines are B_z

penetrated area, the magnetic field will go approximately linearly from the maximum to zero at the critical boundaries across the critical region along the tape width direction when the current is at the positive peak. As the transport current decreases, the magnetic field will also decrease linearly from the surface along the tape width direction, thus the magnetic field distribution is like a sawteeth wave, Fig. 5.35 shows this. Figure 5.36 gives the contour plot of B_z in the stack. The critical region penetrates furthest when the transport current is at maximum. When the current decreases the new critical region will again penetrate from the surface, and it will reach furthest when the current is at minimum. This is illustrated by Fig. 5.36. We can see in Fig. 5.37 that J_y in the new penetrate region is always a constant value $4.44 \times 10^8 \text{ A/m}^2$. J_y in the old penetrated region is the sum of J_y in the solutions of the positive peak and the equivalent negative current. J_y in the sub-critical region has a small value in contrast with the critical current density J_c . Figure 5.38 gives the contour plot of J_y in the stack. Figure 5.39 gives the magnetic flux lines in the stack. In the sub-critical region the flux lines are parallel to the tapes as the model assumptions suggest. Finally Fig. 5.40 gives the contour

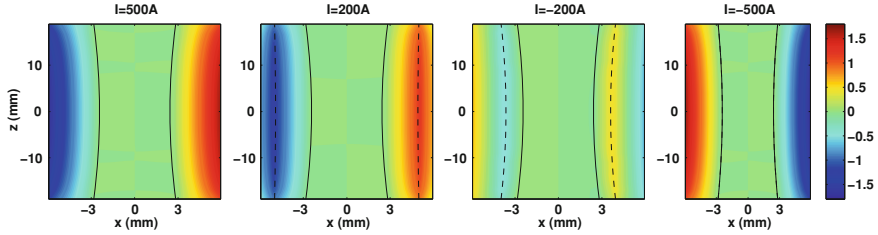


Fig. 5.36 Contour of $B_z(T)$ in the coil during the half cycle (I from 500 to -500 A). The parabolaes with *solid lines* are the critical boundaries at the peak current. The parabolaes with *dotted lines* are the new critical boundaries in the half cycle

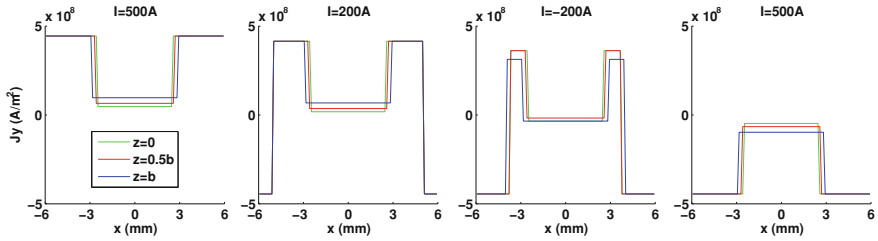


Fig. 5.37 J_y for different tapes at positions $z = 0, 0.5b$ and b in the coil during the half cycle (I from 500 to -500 A)

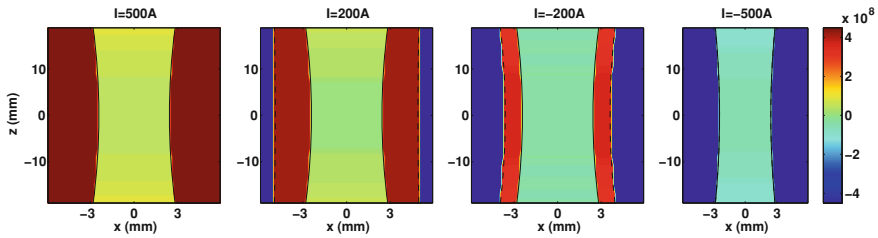


Fig. 5.38 Contour of $J_y(A/m^2)$ in the coil during the half cycle (I from 500 to -500 A)

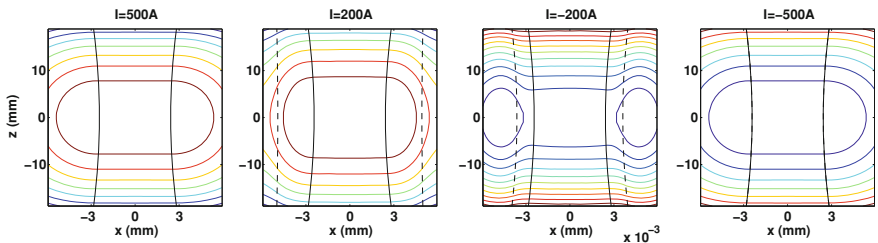


Fig. 5.39 Magnetic flux lines/contour of $A_y(Vs/m)$ in the coil during the half cycle (I from 500 A to -500 A). The parabolaes with *solid lines* are the critical boundaries at the peak current. The parabolaes with *dotted lines* are the new critical boundaries in the half cycle. The *coloured lines* are magnetic flux lines

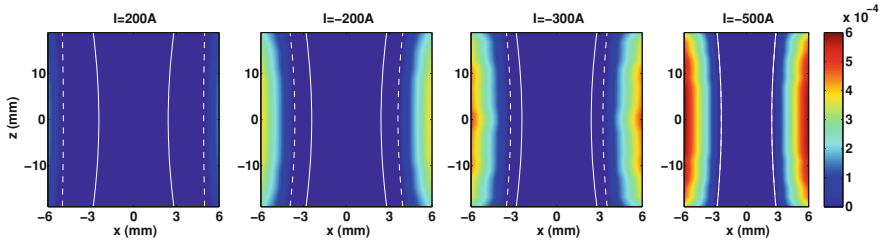
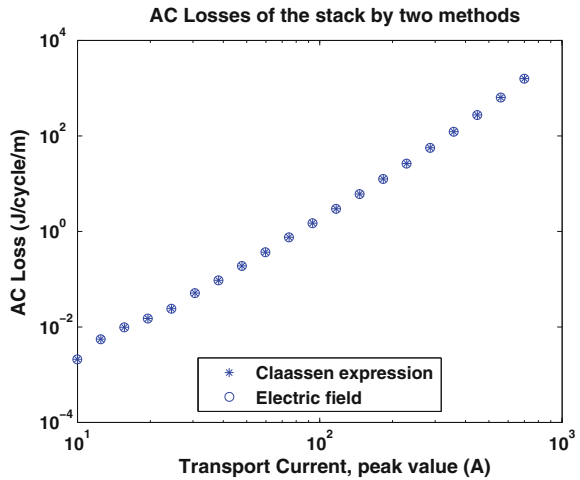


Fig. 5.40 Contour of $\int_{I_i}^{I_{i+1}} E dI$ or $\delta A (V/m)$ in the coil during the half cycle (I from 500 to -500 A). The parabolaes with *solid lines* are the critical boundaries at the peak current. The parabolaes with *dotted lines* are the new critical boundaries in the half cycle

Fig. 5.41 AC losses using the electric field method and the Claassen expression Eq. 5.16 at different transport currents, note the match is perfect



plot of the integration of the electric field between two currents (i.e. the difference of the vector potential of two currents, δA) in the stack, we can see that $\int_{I_i}^{I_{i+1}} E dI$ is getting larger and larger while I is decreasing.

Having found the array of solutions in the half cycle, we can calculate the total AC losses by adding together the AC loss in each change of currents given by Eq. 5.15, i.e. the electrical field method. We computed for a range of AC transport currents with different peak values—from 10 to 800 A. For each transport current, we computed the AC losses with two different methods: the first is to calculate the complete half cycle process, and then calculated the AC losses step by step i.e. the electric field method; the second is only to calculate the solution at the peak current and then calculate the losses using the Claassen expression. The comparison result is given in Fig. 5.41. We can see the total AC losses during the half cycle by the electric field method gives exactly the same result as the Claassen expression (5.16), which validates our model from one aspect.

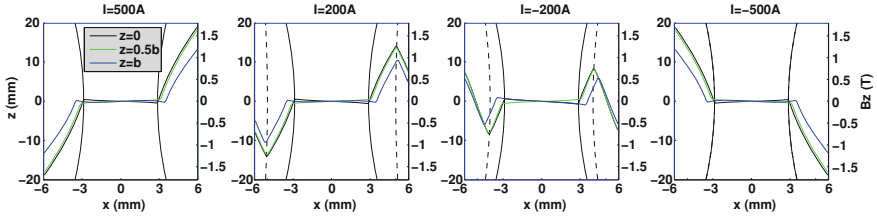


Fig. 5.42 B_z at different levels in the coil during the half cycle (B from 1 T to -1 T). The parabolaes with *solid lines* are the critical boundaries at the peak current. The parabolaes with *dotted lines* are the new critical boundaries in the half cycle. The *coloured lines* are B_z

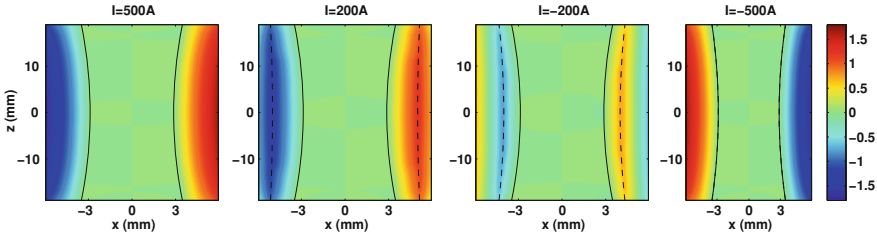


Fig. 5.43 Contour of $B_z(T)$ in the coil during the half cycle (B from 1 T to -1 T). The parabolaes with *solid lines* are the critical boundaries at the peak current. The parabolaes with *dotted lines* are the new critical boundaries in the half cycle

5.3.4.2 J_c depending on local B_z

Now we put in the J_c dependence function as in Eq. 5.12, i.e. in the penetrated region B_z has an impact on the local J_c . This assumption is very important since the magnetic field varies a lot from the surface to the centre of the stack. We retain the transport current and the current array as in Sect. 5.4. The current is decreasing from the positive peak 500 A to the negative peak -500 A. Again we give the solutions at four points during the half cycle from Figs. 5.42, 5.43, 5.44, 5.45, 5.46 and 5.47 in the appendix. Since J_c is no longer a constant value across the critical region, B_z will not change linearly across each tape, Figs. 5.42 and 5.43 shows this. Figures 5.44 and 5.45 present the current densities in the stack. In the sub-critical region the magnetic flux lines are parallel to the tapes in Fig. 5.46. Figure 5.47 illustrates the contour plot of $\int_{I_i}^{I_{i+1}} E dI$ or δA in the stack.

Again, we computed for a range of transport currents with different peak values (from 80 to 800 A) using two different methods: for the electric field method we keep using a 20-point equally spaced array of currents to get the AC losses step by step; for the second method we only calculate one solution at the peak current and then calculate the losses using Eq. 5.18. Figure 5.48 shows the comparison of two different methods. The line with the circle marker is the total AC losses calculated by adding δQ produced by δI , i.e. the electric field method. The line with the asterisk marker is the calculation results given by Eq. 5.18.

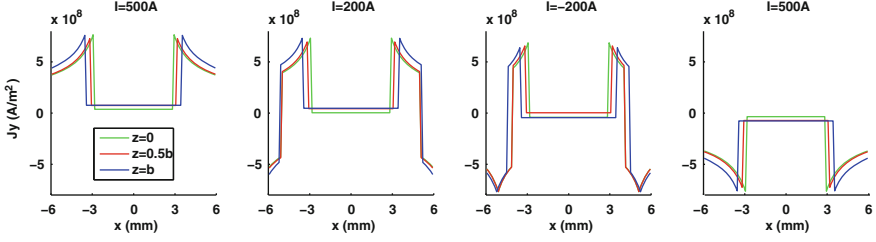


Fig. 5.44 J_y for different tapes at positions $z = 0, 0.5b$ and b in the coil during the half cycle (B from 1 T to -1 T)

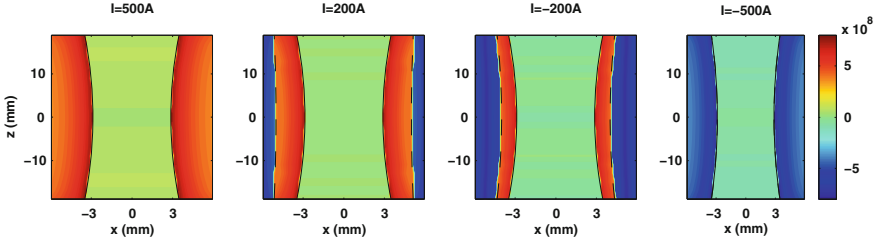


Fig. 5.45 Contour of $J_y(A/m^2)$ in the coil during the half cycle (B from 1 T to -1 T)

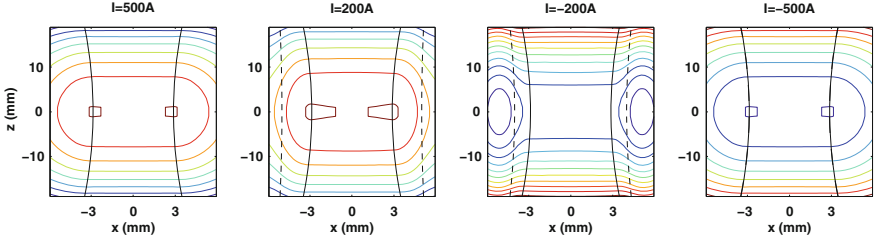


Fig. 5.46 Magnetic flux lines/contour of $A_y(Vs/m)$ in the coil during the half cycle (B from 1 T to -1 T). The parabola with *solid lines* are the critical boundaries at the peak current. The parabola with *dotted lines* are the new critical boundaries in the half cycle. The *coloured lines* are magnetic flux lines

Figure 5.49 gives the comparison of the two methods. The error is given by the expression $error = (loss_E - loss_{formula})/loss_{formula}$, where $loss_E$ means the AC losses by the electric field method, and $loss_{formula}$ means the AC losses by Eq. 5.18. We can see the errors are nearly all below 6%. 6% is a relatively small value in engineering applications. Eq. 5.18 only requires one solution when the current is at maximum, however, the electric field method requires a number of solutions in the whole cycle. Thus to save computation time, we can use Eq. 5.18 to estimate the AC losses.

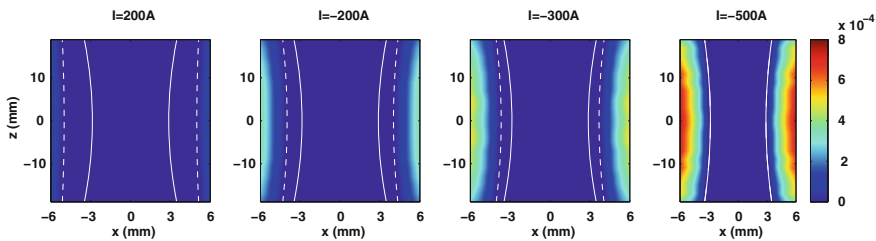
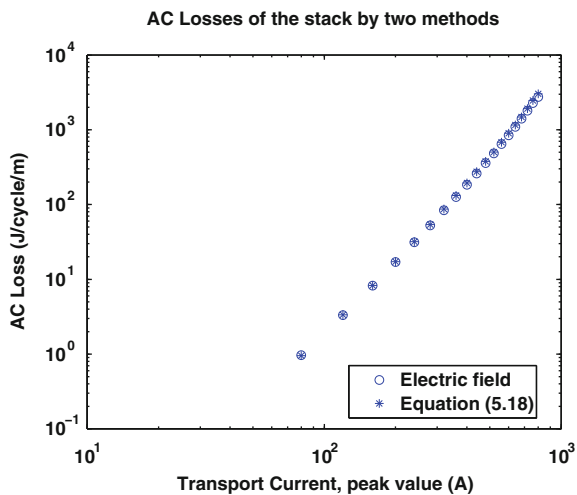


Fig. 5.47 Contour of $\int_{l_i}^{l_{i+1}} E dl$ or $\delta A (V/m)$ in the coil during the half cycle. The parabolaes with *solid lines* are the critical boundaries at the peak current. The parabolaes with *dotted lines* are the new critical boundaries in the half cycle

Fig. 5.48 AC losses using the electric field method and Eq. 5.18 for different transport currents



The error increases sharply when I is approaching 800 A. This is because the critical current of the stack is around 800 A, the stack will be fully penetrated then and this will result in a big error.

5.3.4.3 Instantaneous AC Losses

It is interesting to know how the instantaneous AC losses will change with the time during a AC cycle. In this section we take a half AC cycle from the positive peak 500 A to the negative peak -500 A as an example. Since in our model we directly change the transport current, we need to normalize the current array to a cosine wave to simulate how it changes with the time. To get the instantaneous loss power, we need to divide the losses between two neighbouring currents by the current difference, then normalize them to the cosine wave as well. Although we only calculate half a cycle, we can get the other half by symmetry. Figure 5.50

Fig. 5.49 Error when using Eq. 5.18 to calculate AC losses. Error = $(\text{loss}_E - \text{loss}_{\text{formula}}) / \text{loss}_{\text{formula}}$

Difference of AC losses calculated by electric field method and Equation (5.18)

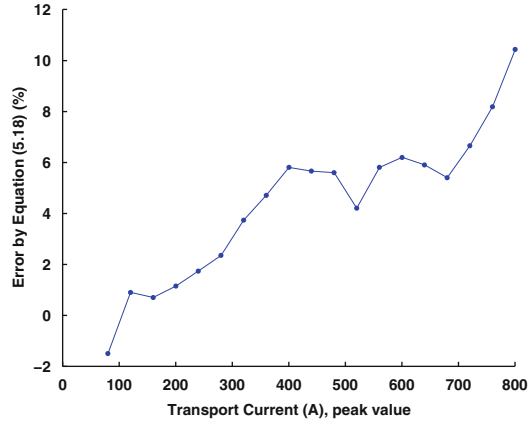
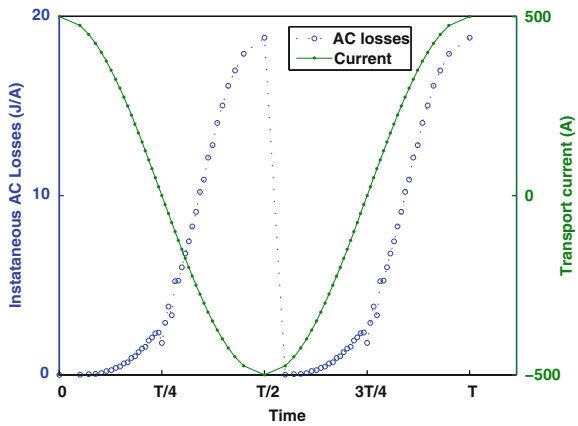


Fig. 5.50 Instantaneous loss power and AC current versus time



shows this. The AC current begins at its maximum value, then changes as a cosine wave. At the beginning the instantaneous loss power is zero because the electric field change rate is zero, then the loss goes up as the electric field increases and reaches the maximum after half a cycle, then it will drop down to zero since the current change rate is zero again, and then increase as same as the first half cycle. We can also get the similar result from a Bean slab.

5.3.5 Stack With AC Applied Field Only

We will now present the result of a stack in an AC applied field. We are assuming J_c depends on the local B_z . Every parameter is retained the same as in Sect. 5.3.4 except that there is no transport current but an AC field decreasing from 1 T to -1 T. Then we follow the solution process presented in Sect. 5.3.2. The

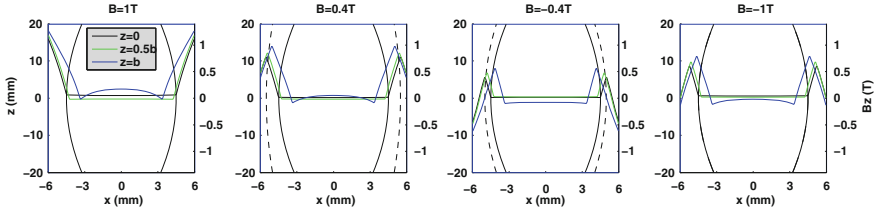


Fig. 5.51 B_z at different levels in the coil during the half cycle. The parabolaes with *solid lines* are the critical boundaries at the peak field. The parabolaes with *dotted lines* are the new critical boundaries in the half cycle. The *coloured lines* are B_z

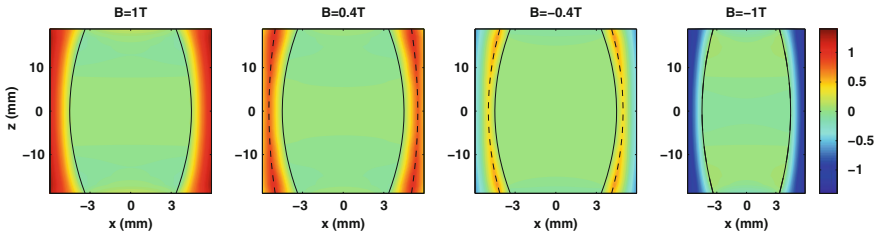


Fig. 5.52 Contour of $B_z(T)$ in the coil during the half cycle. The parabolaes with *solid lines* are the critical boundaries at the peak field. The parabolaes with *dotted lines* are the new critical boundaries in the half cycle

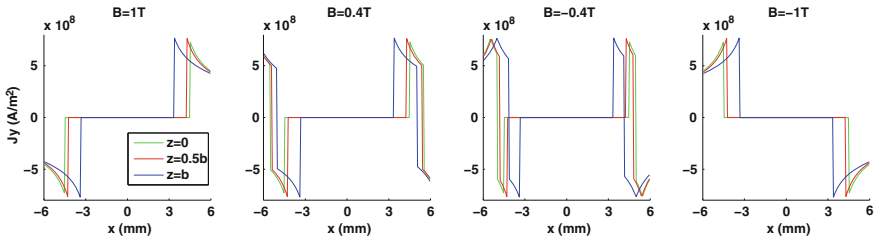


Fig. 5.53 J_y for different tapes at positions $z = 0, 0.5b$ and b in the coil during the half cycle

calculation results are given in Figs. 5.51, 5.52, 5.53, 5.54, 5.55 and 5.56 in the appendix. Figures 5.51 and 5.52 present the magnetic field distribution in the stack. The magnetic field is approximately zero within the central sub-critical region. At the stack surface B_z is slightly higher than the applied 1 T field. Figure 5.53 and 5.54 give the current density distribution. In the sub-critical region there is no current density. On each side of the new and old penetrated region, the critical current density has an opposite sign. We can see from Fig. 5.55 that there is no magnetic field in the sub-critical region. Finally Fig. 5.56 gives the integration of $\int_{I_i}^{I_{i+1}} E dI$ or δA in the stack. All the calculation results are consistent with the model assumptions in Sect. 5.3.2.

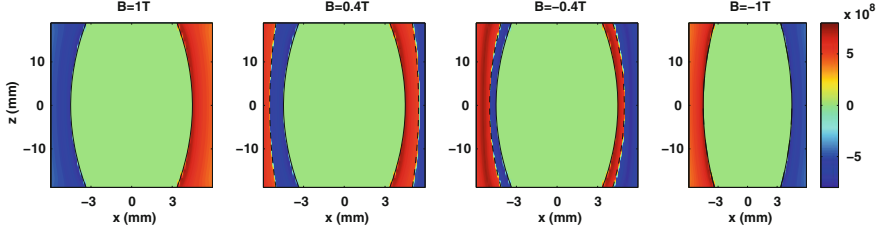


Fig. 5.54 Contour of $J_y(A/m^2)$ in the coil during the half cycle

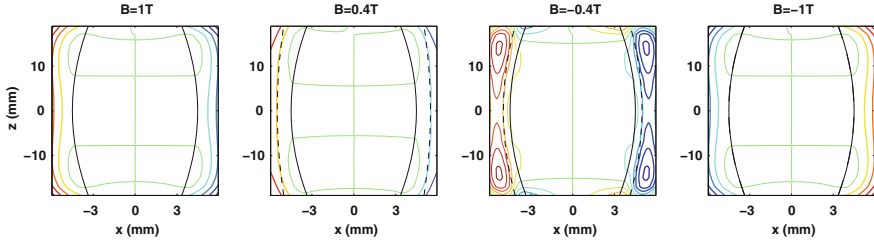


Fig. 5.55 Magnetic flux lines/contour of $A_y(Vs/m)$ in the coil during the half cycle. The parabolaes with *solid lines* are the critical boundaries at the peak field. The parabolaes with *dotted lines* are the new critical boundaries in the half cycle. The *coloured lines* are magnetic flux lines

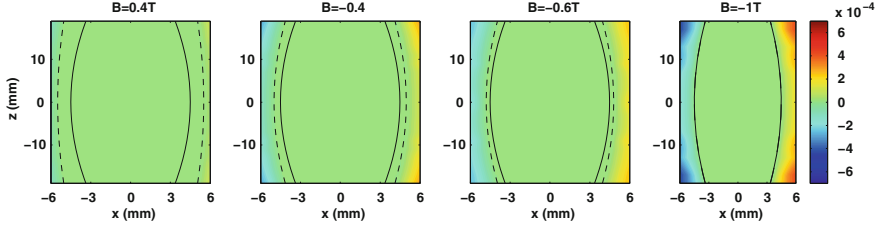


Fig. 5.56 Contour of $\int_{I_i}^{I_{i+1}} E dI$ or $\delta A(V/m)$ in the coil during the half cycle. The parabolaes with *solid lines* are the critical boundaries at the peak field. The parabolaes with *dotted lines* are the new critical boundaries in the half cycle

Then we go on to calculate the total AC losses in a range of magnetic fields with different peak values— from 0 T to 2 T. Again we calculate the AC losses using two different methods: the electric field method and Eq. 5.18. Figure 5.57 shows the comparison result. The line with the circle marker is the total AC losses calculated by adding δQ produced by δI , i.e. the electric field method. The line with the asterisk marker is the calculation results given by Eq. 5.18.

Figure 5.58 shows the difference between the two results. The error is given by the expression $\text{Error} = (\text{loss}_E - \text{loss}_{\text{formula}}) / \text{loss}_{\text{formula}}$, where loss_E means the AC losses by the electric field method, and $\text{Loss}_{\text{formula}}$ means the AC losses by Eq. 5.18. We can see the error is around 10% if we use Eq. 5.18 to calculate the

Fig. 5.57 AC losses by the electric field method and Eq. 5.18

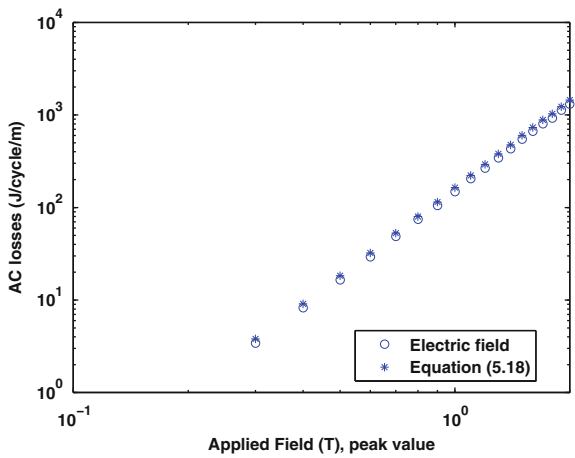
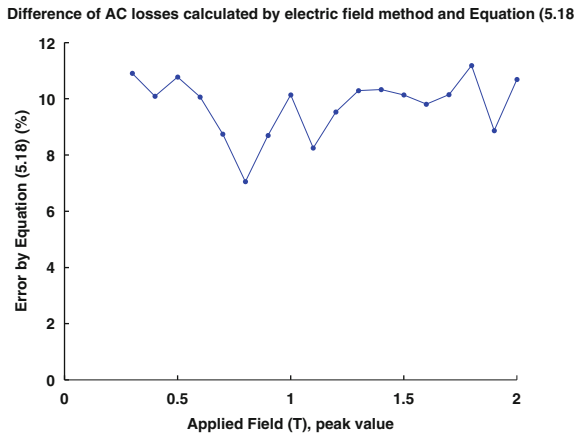


Fig. 5.58 Error when using Eq. 5.18 to calculate AC losses. Error = $(\text{loss}_E - \text{loss}_{\text{formula}}) / \text{loss}_{\text{formula}}$



AC losses. Again, 10% is a relatively small value for engineering estimation, and Eq. 5.18 saves the computation time significantly. Thus we can use Eq. 5.18 to calculate the AC losses.

5.3.6 Discussion

This section assumes the critical region penetrate furthest when the AC current is at the positive peak, then a new critical region will begin to penetrate from the surface again as the AC current starts to decrease. When the AC current reaches the negative peak, the penetrated region will be exactly the same with those at the positive peak, but the magnetic field and the current densities will be opposite. The calculation results are consistent with our model assumptions.

In the case that the stack carries an AC transport current, if we assume J_c is constant in the critical region the AC losses given by our model are equal to the Claassen formula Eq. 5.16 as shown in Fig. 5.41. If we assume J_c depends on the local B_z , Eq. 5.18 will give a result about 6% less than the real value given by the electric field method as shown in Fig. 5.48. Although Eq. 5.18 is not 100% accurate, we could apply a correction factor to it. Moreover, Eq. 5.18 is very convenient to use and saves a lot of computation time since it only requires only one solution at the peak current, while the electric field method normally requires 20 solutions during a full cycle. Thus our method is still preferable and acceptable in engineering application.

For the case that the stack is in an AC applied field, the calculation results are consistent with the assumptions as well. Equation 5.18 gives AC losses about 10% less than the real values as shown in Fig. 5.57.

5.4 Comparison of Infinitely Long Stack and Circular Pancake Coil

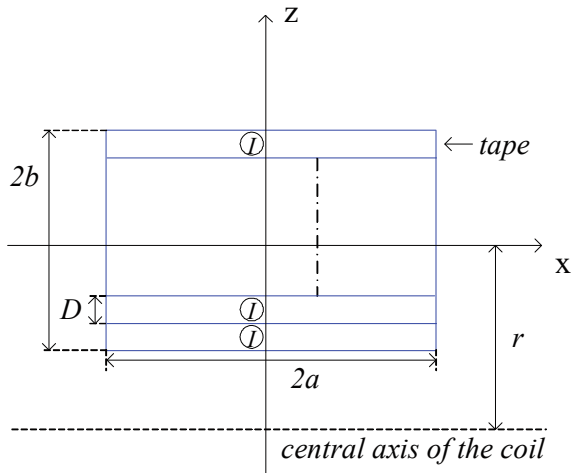
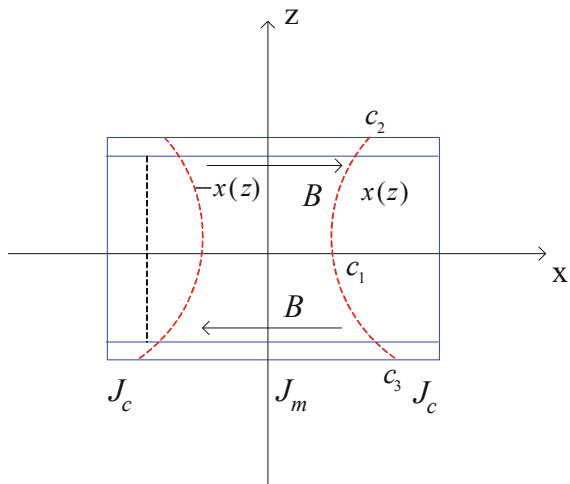
The models in previous sections in this chapter all use an infinitely long stack of tapes to approximate the circular coils. This section presents an exact model of circular coils. For a small value of the coil radius, there is an asymmetry along the coil radius direction. As the coil radius increases, this asymmetry will gradually decrease.

In this section AC losses of the circular coil with a transport current are calculated. A comparison is made between the results of the circular coil and the long straight conductor. We find that if the internal radius is equal to the winding thickness the long conductor approximation overestimates the loss by 10% and even if the internal radius is reduced to zero, the error is still only 60%. The infinitely long stack approximation is therefore adequate for most engineering applications.

5.4.1 Assumptions of the Model

Due to the symmetry, we only need to analyse the cross section of the coil. Figure 5.59 gives the cross section view of a circular coil. These tapes are insulated from each other and are all carrying the same current I . The width and thickness of each tape are $2a$ and D respectively, the thickness of the coil is $2b$, the mean radius of the coil is r . We set the origin at the centre of the cross section.

Following the assumptions in Sect. 5.2, Fig. 5.60 shows the two regions in the coil. The unpenetrated region is the inner part constrained by the red dashed curves, the penetrated region is the outer part. The vertices of the parabola do not lie on the x -axis. In the penetrated area, the current density is the critical current density J_c ; in the unpenetrated area, the current density is J_m , the magnetic field is

Fig. 5.59 Circular coil cross-section**Fig. 5.60** Circular coil critical and subcritical regions

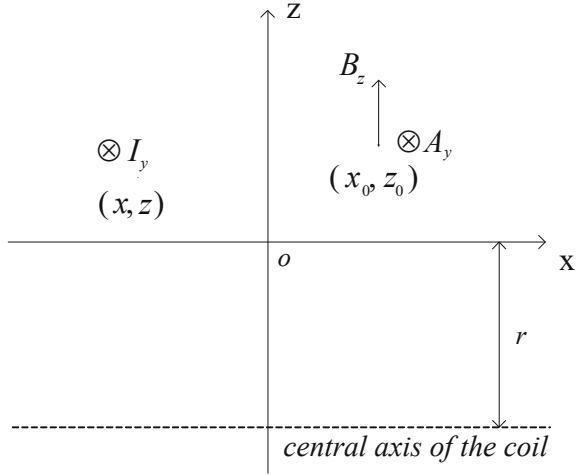
parallel to the tapes. Due to the symmetry along the x -axis we assume the red curves representing critical boundaries can be described by two parabolae,

$$x(z) = \pm \left(c_1 + \frac{c_2 - c_3}{2b} z + \frac{(c_2 + c_3)/2 - c_1}{b^2} z^2 \right) \quad (5.19)$$

where c_1 is the x -coordinate value of the intersection point of the right parabola with the x -axis, c_2 and c_3 are the x -coordinate values of the intersection points of the right parabola with the top and bottom boundaries of the cross section area.

We should notice that unlike Fig. 5.3, in Fig. 5.60 the vertices of the parabolae will not lie on the x -axis because of the asymmetry along the z -axis; however,

Fig. 5.61 Vector potential and magnetic field for a ring current



when the radius is much larger than the thickness of the coil, it will behave like an infinitely long stack of tapes, and the vertices will then lie on the x -axis.

We need to point out that there are other more complicated functions which can describe the critical boundary more accurately. However, a parabola is the simplest three-parameter fit to describe the critical boundary, thus to gain an acceptable computation speed we use the parabola in this section.

5.4.2 Solution Methodology

We consider a ring located at (x, z) as shown in Fig. 5.61 with a current I flowing in it. The vector potential and radial component of the magnetic field at the point (x_0, z_0) due to the ring are [27],

$$A_y = \frac{\mu_0 I}{\pi k} \left(\frac{a}{r_1} \right)^{\frac{1}{2}} \left[\left(1 - \frac{1}{2} k^2 \right) K - E \right] \quad (5.20)$$

$$B_z = \frac{\mu_0 I}{2\pi r_1} \frac{d}{(d^2 + (a + r_1)^2)^{\frac{1}{2}}} \left[-K + \frac{a^2 + r_1^2 + d^2}{(a - r_1)^2 + d^2} E \right] \quad (5.21)$$

$$k^2 = 4ar_1[d^2 + (a + r_1)^2]^{-1} \quad (5.22)$$

$$a = r + z, r_1 = r + z_0, d = x - x_0 \quad (5.23)$$

where K and E are complete elliptic integrals of the first and second kind.

A block in Fig. 5.5 carrying a current density J_y within the area $x_1 < x < x_2$, $z_1 < z < z_2$, produces a vector potential and z direction magnetic field at the point (x_0, z_0) as in Eqs. (5.24) and (5.25),

$$A_y(x_1, x_2, z_1, z_2) = \int_{x_1}^{x_2} \int_{z_1}^{z_2} A_y(x, z) dx dz \quad (5.24)$$

$$B_z(x_1, x_2, z_1, z_2) = \int_{x_1}^{x_2} \int_{z_1}^{z_2} B_z(x, z) dx dz \quad (5.25)$$

where A_y and B_z are give by Eqs. 5.20–5.23, in which I is replaced by J_y .

By summing the contributions from each block we can find the total A_y and B_z at every point of the cross section. Unlike the infinitely long stack model, A_y in Eq. 5.20 is zero on the axis of the coil for all rings in the pancake. Therefore we do not need to subtract the contribution of A_y at $(0, 0)$ from each block.

Following the same solution methodology in Sect. 5.2.2. Again we are using the fixed division method. A detailed division example is already given in Fig. 5.5. For a given transport current I , we firstly need to solve Eqs. 5.6 and 5.7. Then we vary c_1, c_2 and c_3 to search for the minimum $f_c = \int_{-b}^b \int_{-c(z)}^{c(z)} B_z^2 dx dz$ to make it approximately zero. This gives the nearest solution to the ideal which has $B_z = 0$ at all points in the unpenetrated region. Having found c_1, c_2 and c_3 , we can get the distribution of J_y, A_y and B_z in the circular coil.

To get the AC losses of a coil on applying a transport current, we use Eq. 5.18 to calculate the losses Q_0 in the initial quadrant. Then using $Q = 4Q_0$ can approximately calculate the AC losses in a full cycle. In Sect. 5.3 and [23] it was shown that Q is about 7% less than the full cycle AC loss due to the dependence of J_c on B_z and computing the complete cycle adds significantly to the complexity. For most engineering applications, 7% is acceptable and Eq. 5.18 can give a much quicker estimate compared to finding solutions for a full cycle as already demonstrated in Sect. 5.3. Thus we will use $Q = 4Q_0$ to calculate the AC losses in full cycle for this section.

5.4.3 Configuration of the Pancake Coil

We are using the same pancake as shown in Table 5.2. The J_c depending on B_z function is kept the same as Eq. 5.12.

$$J_c = J_0 \frac{B_0}{B_0 + |B_z|} \quad (5.26)$$

Fig. 5.62 Configuration of tape and circular pancake coil

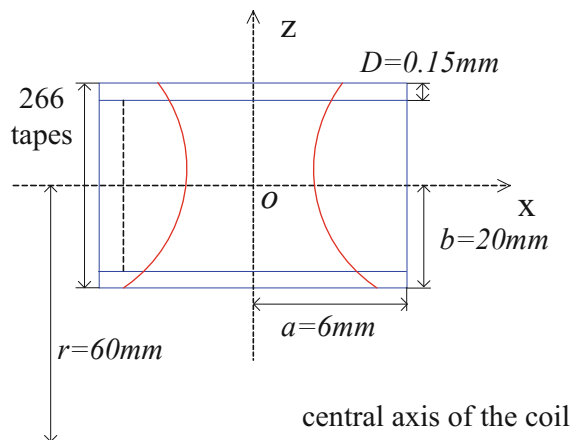
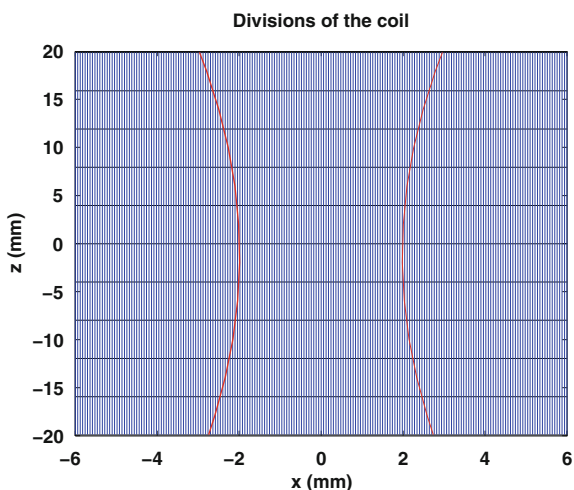


Fig. 5.63 Coil division



The detailed configuration of the circular pancake coil is shown in Fig. 5.62.

5.4.4 Solution for Fixed Transport Current

The computation results are shown in Figs. 5.63, 5.64, 5.65 and 5.66:

Figure 5.63 shows the fixed division method with $M = 10$ and $N = 200$. Figure 5.64 shows in the unpenetrated area the perpendicular magnetic field B_z is approximately zero and the flux lines are parallel to the x -axis. Since the radius r has a relatively large value $3b$, the asymmetry effect is not obvious, c_2 and c_3 are nearly the same. Figures 5.65 and 5.66 present the contour plots of B_z and J_y in the coil. All these results are in good agreement with the model assumption.

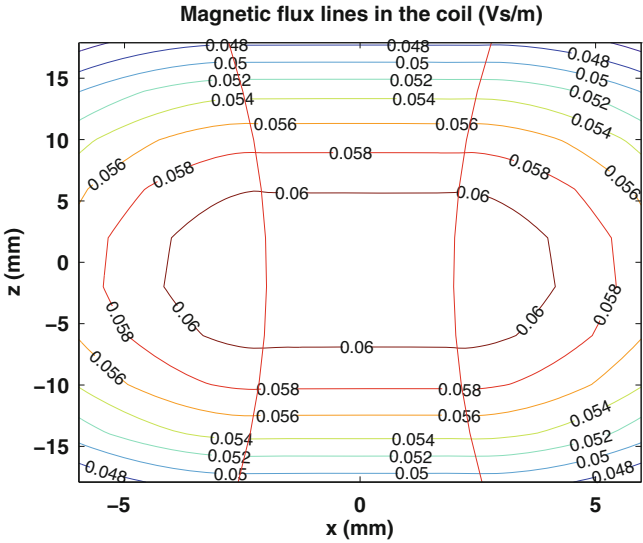
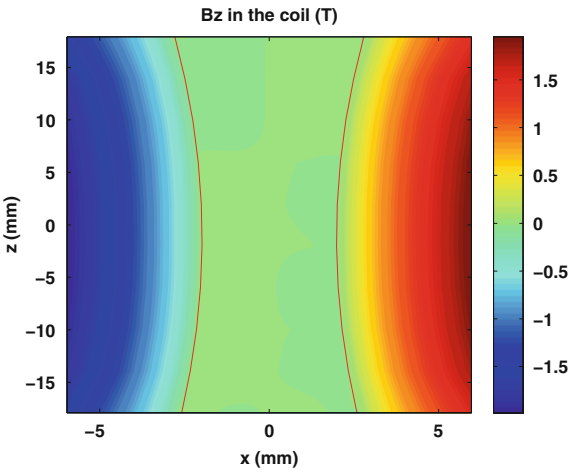


Fig. 5.64 Magnetic flux lines in the coil

Fig. 5.65 Contour of B_z in the coil



The AC losses of the coil on the cross section area in a full cycle would be 792.7 J/cycle/m. The AC losses of the infinitely long stack on the cross section area in a full cycle is 843.3 J/cycle/m. Table 5.3 gives the comparison results of the AC losses and computation time. The z -component magnetic field in the coil will partly be compensated by the other half of the coil, so the modulus of B_z will be smaller than that in an infinitely long stack, the AC loss will thus be smaller. The program was running in a PC with Intel Core2 Duo 2.00 GHz and 3 GB memory. We can see that the AC losses of the circular coil is 94% but the computation time is more than three times of those of an infinitely long stack.

Fig. 5.66 Contour of J_y in the coil

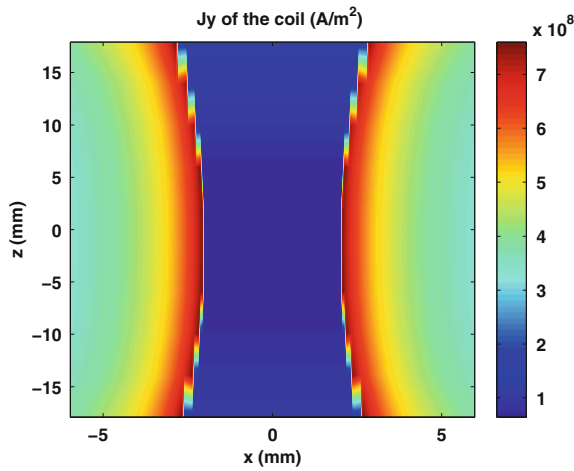


Table 5.3 Comparison of AC losses and computation time between circular coil and infinitely long stack

	AC losses (J/cycle/m)	Computation time (s)
Circular coil	792.7	68.8
Infinitely long stack	843.3	20.5

5.4.5 Solution with Different Transport Currents

Now we apply transport AC currents with different peak values into the coil, find solutions individually, and observe how the penetration depth and AC losses will change with the transport current. We define $d = \frac{1}{3} \frac{(a-c_1)+(a-c_2)+(a-c_3)}{a}$ as the penetration depth. Again we use $M = 10$ and $N = 200$ to divide the cross section area.

For comparison we also computed solutions for the infinitely long stack model, in which the cross section area and tapes are the same as the circular coils. Figures 5.67 and 5.68 present the results:

We find that the AC losses increase approximately with the cube of the current I , the penetration depth increases from 0 to nearly 1 as the transport current increases from 0 to 700 A. We can also find both for AC losses and penetration depth, the circular coil model gives slightly smaller values than the infinitely long stack model. This will be explained in Sect. 5.4.6

5.4.6 Effect of Coil Radius

Although normally there is an asymmetry along the z -axis of the circular model, for a relatively large value of the radius r the coil will rather behave like an

Fig. 5.67 Full cycle AC losses of coil with different currents

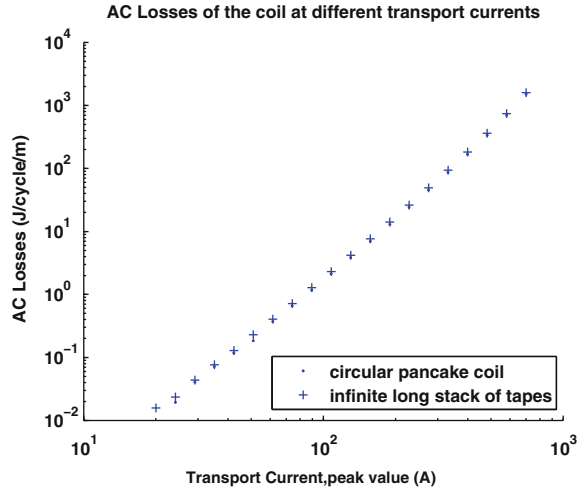
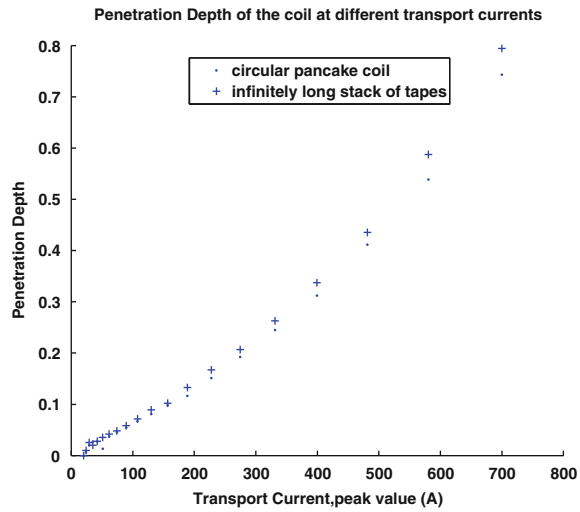


Fig. 5.68 Penetration depth of coil with different currents



infinitely long stack. We now keep all the configurations the same as in Sect. 5.4.3, except for changing the radius r from $3b$ to $100b$. The computation result shows that c_1 , c_2 and c_3 are 1.9, 2.8 and 2.8 mm, respectively. The AC loss is 844.1 J/cycle/m. For an infinitely long stack with the same configuration and transport current, c_1 , c_2 and c_3 will also be 1.9, 2.8 and 2.8 mm, and the AC loss will be 844.4 J/cycle/m. Thus when r is very large, we can use the relatively simple model of an infinitely stack to approximate pancake circular coils.

To understand how the radius of the coil affects the AC losses, penetration depths and critical currents (in Sect. 5.2 and [22]) it was defined that the critical current would be the minimum transport current when the critical regions penetrate into the

Fig. 5.69 AC losses of coil with different radii normalized to those of an infinitely long stack

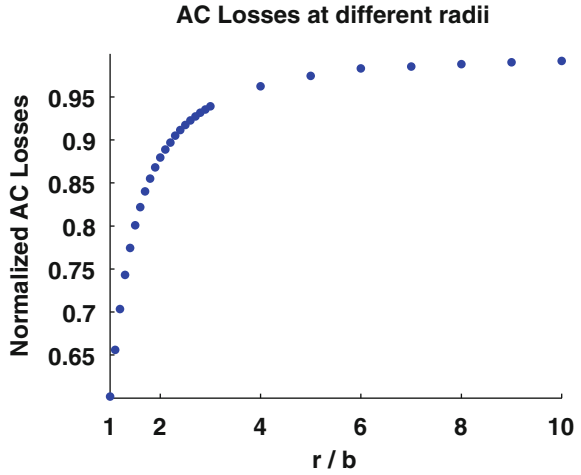
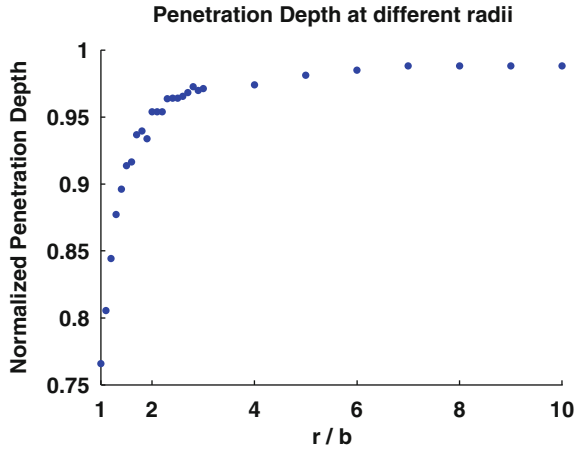


Fig. 5.70 Penetration depth of coil with different radii normalized to those of an infinitely long stack



centre of one of the tapes), we vary r but keep the cross section and transport current the same as in Sect. 5.4.3. Obviously the minimum r is 1, in which case there is no central core. The normalized computation results are given in Figs. 5.69 and 5.70. Also we produced a look-up table for the computation results as in Table 5.4..

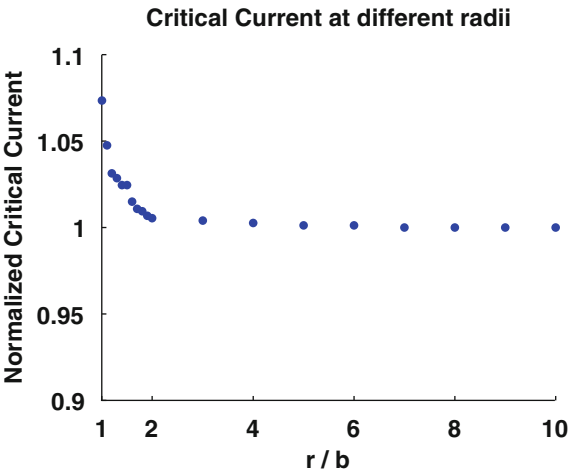
From Fig. 5.69 we can see that the AC losses of the circular coil will be approximately the same as an infinitely long stack when r reaches $10b$. The penetration depth will also equal that of an infinitely long stack since r is larger than $4b$ as shown in Fig. 5.70. The critical current will approach that of an infinitely long stack since r is larger than $3b$ as shown in Fig. 5.71. Since there are some computation errors the curves in Figs. 5.70 and 5.71 are not very smooth when r/b is small.

Table 5.4 Look-up table of corrections factors^a of coil AC losses at different radii

Coil size (r/b)	Correction Factor	Coil size (r/b)	Correction Factor	Coil size (r/b)	Correction Factor	Coil size (r/b)	Correction Factor
1.0	0.60	1.7	0.84	2.4	0.91	4	0.96
1.1	0.66	1.8	0.85	2.5	0.91	5	0.97
1.2	0.70	1.9	0.87	2.6	0.92	6	0.98
1.3	0.74	2.0	0.88	2.7	0.93	7	0.99
1.4	0.77	2.1	0.89	2.8	0.93	8	0.99
1.5	0.80	2.2	0.90	2.9	0.94	9	0.99
1.6	0.82	2.3	0.90	3.0	0.94	10	0.99

^a Correction Factor = the AC losses of the coil/the AC losses of the infinitely long stack.

Fig. 5.71 Critical currents of coil with different radii normalized to those of an infinitely long stack



When the radius is relatively small, the z -component magnetic field will partly be compensated by the other half of the coil, so the modulus of B_z will be smaller than that in an infinitely long stack, the AC loss and penetration depth will thus be reduced. As the radius increases, this impact will decrease until the circular coil behaves like an infinitely long stack. This also explains why in Figs. 5.67 and 5.68 the AC losses and penetration depth of the coil are smaller than those of an infinitely long stack. Even quite small coils can be treated as infinitely long. The error is 10% when $r = 3b$.

To get a better comparison of the circular model and the infinitely long stack model, we present Figs. 5.72, 5.73, 5.74, 5.75, 5.76 and 5.77 showing the graphs of a small circular coil with $r = 1.2b$ (when $r = b$ there is no central core so this is quite a small radius coil) and an infinitely long stack. From the figures it is clear that when the radius r is small, there will be more flux lines in the inner half than the outer half of the coil, while in an infinitely long stack the flux lines are symmetric in each half. We need to point out that since in the circular coil model the zero of the vector potential is along the coil axis, however in the infinitely long

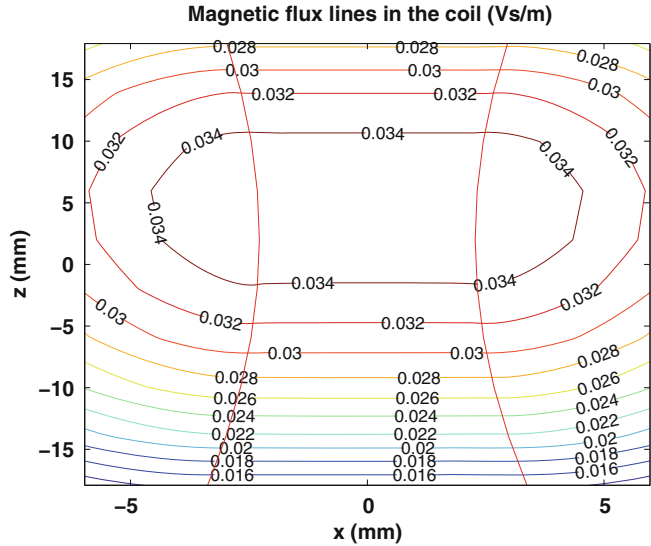


Fig. 5.72 Magnetic flux lines in the coil when $r = 1.2b$

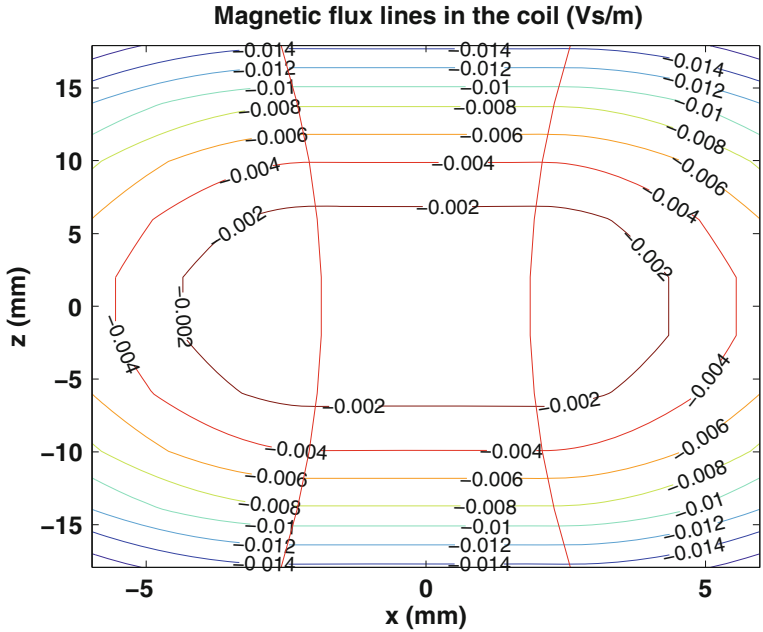


Fig. 5.73 Magnetic flux lines in the infinitely long stack

Fig. 5.74 B_z at different levels in the coil when $r = 1.2b$

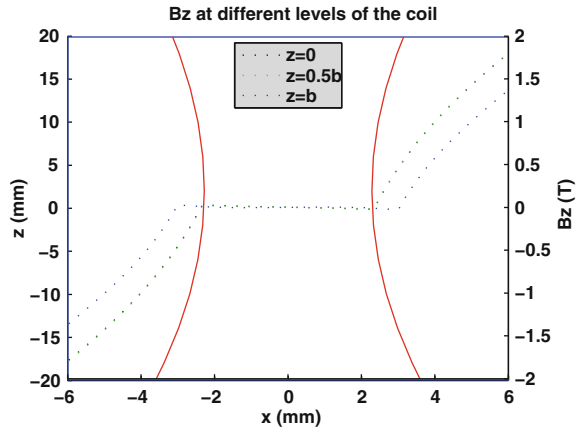


Fig. 5.75 B_z at different levels in the infinitely long stack

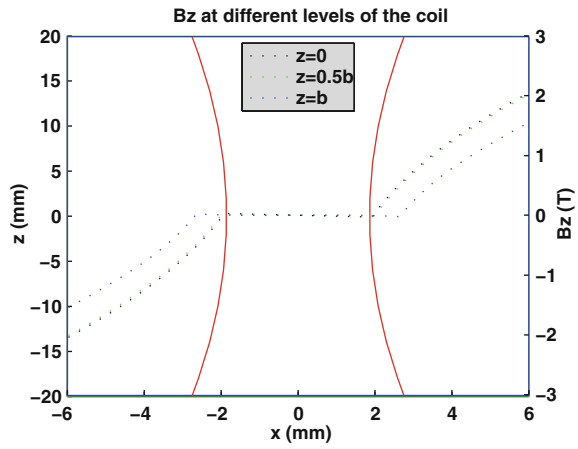


Fig. 5.76 J_y at different levels in the coil when $r = 1.2b$

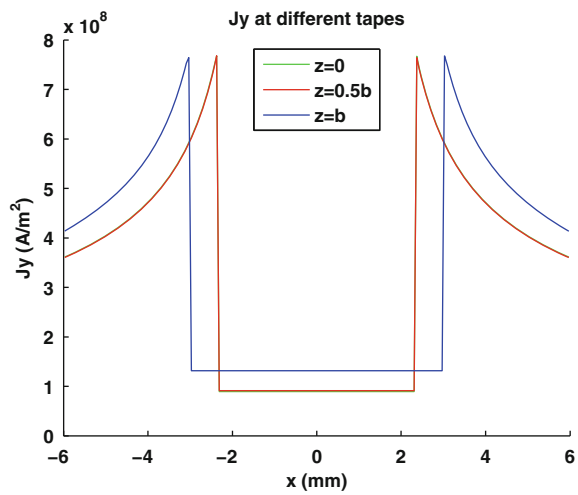
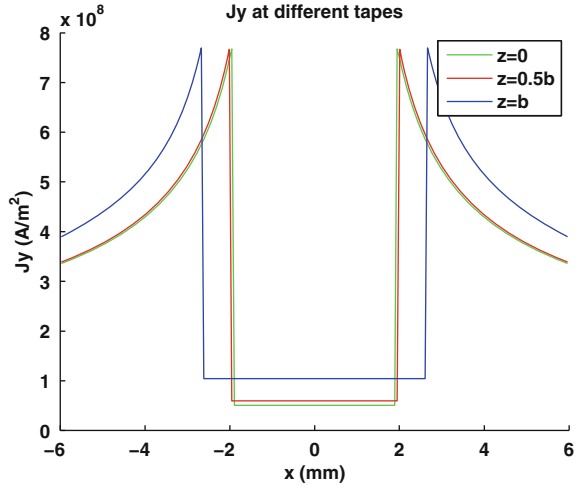


Fig. 5.77 J_y at different levels in the infinitely long stack



stack we define the centre as the origin, the values of the contour of vector potentials are very different between Figs. 5.72 and 5.73. The penetration depth of the circular coil will be smaller. Due to the cancelling effect of the other half of the circular coil, B_z will also be smaller than that in the same place of the infinitely long stack.

5.5 Conclusions

Following the introduction of Clem's anisotropic homogeneous-medium approximation in Sects. 5.1 and 5.2 gives a more detailed model for a pancake coil of 2G HTS tapes, adapts it for a transport current and magnetisation in an applied field, and then calculates the AC losses taking into account the variation of J_c with B_z . The calculations results are consistent with the model assumptions. This model offers a fast numerical method to calculate the critical current and AC losses of the superconducting pancake coils.

Section 5.3 gives how the distribution of the current density and magnetic field in the coil changes during a full AC cycle. Starting from the existing model for a stack of superconducting tapes, we have adapted it to analyze a stack with an AC transport current in a full cycle. We have showed how the current density and magnetic field distribution change during a full AC cycle. This model has also been adapted to calculate the stack in an AC applied field. More importantly, it demonstrates we don't need to analyse a full AC cycle to calculate AC losses, we just need to find the solution at the I_{max} or B_{max} and then use Eq. 5.18 to calculate the losses, and the error will be below 10%, which is acceptable in engineering applications. This saves computation resources significantly.

Section 5.4 gives an exact circular pancake coil model. Compared with the infinitely long stack approximation model, this circular coil model give very similar

calculation results. Therefore the infinitely long stack approximation for a circular pancake coil is therefore adequate for most practical purposes since the error is small and the computation time is saved significantly. We find that if the internal radius is equal to the winding thickness the infinitely long stack approximation overestimates the AC losses by 10% and even if the internal radius is reduced to zero, the error is still only 60%. In addition, the computation time for calculating the infinitely long stack is less than one-third of that for a circular pancake coil.

In conclusion, we have developed a new computationally efficient numerical model to analyse an infinitely long stack of tapes and a circular pancake coil using coated conductors. This model gives a relatively faster computation speed while maintaining the physics background. The critical current and AC losses can be predicted. In addition, the magnetic field and current density distribution in the stack or coil can be calculated during a full AC cycle. After comparison the conclusion is made that the infinitely long stack of tapes are accurate enough for most engineering applications. To calculate AC losses, only the solution when I or B is at maximum is needed.

References

1. Yuan W, Xian W, Ainslie MD, Hong Z, Yan Y, Pei R, Jiang Y, Coombs TA (2010) Design and test of a superconducting magnetic energy storage (SMES) coil. *IEEE Trans Appl Supercond* 20(3):1379–1382
2. Noe M, Steurer M. High-temperature super-conductor fault current limiters: concepts, applications, and development status. *Supercond Sci Technol* 20(3):R15
3. Clem JR (2008) Field and current distributions and AC losses in a bifilar stack of superconducting strips. *Phys Rev B (Condens Matter Mater Phys)* 77(13):134506
4. Jiang Y, Pei R, Xian W, Hong Z, Coombs TA (2008) The design, magnetization and control of a superconducting permanent magnet synchronous motor. *Supercond Sci Technol* 21(6):065011
5. Jiang Y, Pei R, Hong Z, Song J, Fang F, Coombs TA (2007) Design and control of a superconducting permanent magnet synchronous motor. *Supercond Sci Technol* 20(7):585
6. Jiang Y, Pei R, Jiang Q, Hong Z, Coombs TA (2007) Control of a superconducting synchronous motor. *Supercond Sci Technol* 20(4):392
7. Jiang Y, Pei R, Xian W, Hong Z, Yuan W, Marchant R, Coombs TA (2009) Magnetization process of an hts motor and the torque ripple suppression. *Appl Supercond IEEE Trans* 19(3):1644–1647
8. Jiang Q, Majoros M, Hong Z, Campbell AM, Coombs TA (2006) Design and AC loss analysis of a superconducting synchronous motor. *Supercond Sci Technol* 19(11):1164
9. Grilli F, Stephen P, Ashworth SP (2007) Measuring transport AC losses in YBCO-coated conductor coils. *Supercond Sci Technol* 20(8):794–799
10. Grilli F, Ashworth SP (2007) Quantifying AC losses in YBCO-coated conductor coils. *Appl Supercond IEEE Trans* 17(2):3187–3190
11. Brambilla R, Grilli F, Nguyen DN, Martini L, Sirois F (2009) AC losses in thin superconductors: the integral equation method applied to stacks and windings. *Supercond Sci Technol* 22(7):075018
12. Brambilla R, Grilli F, Martini L, Sirois F (2008) Integral equations for the current density in thin conductors and their solution by the finite-element method. *Supercond Sci Technol* 21(10):105008

13. Pardo E (2008) Modeling of coated conductor pancake coils with a large number of turns. *Supercond Sci Technol* 21(6):065014
14. Souc J, Pardo E, Vojenciak M, Gomory F (2009) Theoretical and experimental study of AC loss in high temperature super-conductor single pancake coils. *Supercond Sci Technol* 22(1):015006
15. Clem JR, Claassen JH, Mawatari Y (2007) AC losses in a finite z stack using an anisotropic homogeneous-medium approximation. *Supercond Sci Technol* 20(12):1130–1139
16. Jiang Y, Pei R, Jiang Q, Hong Z, Coombs TA (2007) Control of a superconducting synchronous motor. *Supercond Sci Technol* 20(4):392
17. Kim YB, Hempstead CF, Strnad A (1963) Magnetization and critical supercurrents. *Phys Rev* 129(2):528–535
18. Kim YB, Hempstead CF, Strnad AR (1962) Critical persistent currents in hard superconductors. *Phys Rev Lett* 9(7):306–309
19. Hague B (1929) *Electromagnetic problems in electrical engineering*. Oxford University press, London
20. Weber E (1950) *Electromagnetic fields-theory and applications*, vol 1. Wiley, New York
21. Yuan W, Campbell AM, Coombs TA (2009) A model for calculating the AC losses of second-generation high temperature superconductor pancake coils. *Supercond Sci Technol* 22(7):075028
22. Yuan W, Campbell AM, Coombs TA (2010) AC losses and field and current density distribution during a full cycle of a stack of super-conducting tapes. *J Appl Phys* 107(9):093909
23. Claassen JH (2006) An approximate method to estimate AC loss in tape-wound superconducting coils. *Appl Phys Lett* 88(12):122512
24. Hong Z, Campbell AM, Coombs TA (2006) Numerical solution of critical state in superconductivity by finite element software. *Supercond Sci Technol* 19(12):1246–1252
25. Hong Z, Campbell AM, Coombs TA (2007) Computer modeling of magnetisation in high temperature bulk super-conductors. *Appl Supercond IEEE Trans* 17(2):3761–3764
26. Norris WT (1970) Calculation of hysteresis losses in hard superconductors carrying AC: isolated conductors and edges of thin sheets. *J Phys D Appl Phys* 3(4):489–507
27. Smythe WR (1989) *Static and dynamic electricity*. Hemisphere, New York , p 290

Chapter 6

Coil Tests and Applications for SMES

This chapter¹ introduces the superconducting coils and their experimental tests. [Section 6.1](#) introduces the configuration and winding techniques of the coils. [Sections 6.2](#) and [6.3](#) present the critical current and AC loss measurement results. The experimental set-up for the critical current measurement at 77 K includes a cryogenic container, a power supply, instrumentation and a measurement system. The experimental set-up for AC losses measurement at 77 K includes a cryogenic container, a power supply, an inductive voltage compensation circuit and a measurement system. The critical current and AC losses of the coils are measured at 77 K. An experiment rig using cryocooler which can cool down to 20 K is also introduced.

[Sections 6.4](#), [6.5](#) and [6.6](#) introduce the control circuit for the superconducting coils to be used as a SMES unit. This control circuit can quickly charge and discharge the superconducting coils, and it has been both simulated and experimentally tested to validate the control strategy.

Part of the experiment in [Sects 6.2](#), [6.3](#) and [6.5](#) was carried out by the author at Cryogenic Ltd and China Electric Power Research Institute. Cryogenic Ltd provided the winding machines, the critical current measurement set-up and the background magnet. Part of the control strategy in [Sect. 6.6](#) is advised by Dr. Jiahui Zhu from China Electric Power Research Institute.

¹ Parts of this chapter are reprinted with permission from Yuan et al. [[18](#)] ©2010 IEEE.
Parts of this chapter are reprinted with permission from Zhu et al. [[19](#)] ©2011 Elsevier.

6.1 Superconducting Coils

6.1.1 Coil Configurations

Three superconducting coils have been made. One is a relatively large single pancake coil, and the other two coils are two small double-pancake coils. Table 6.1 presents the configurations of the coils.

6.1.2 Coil Windings

Two different techniques are used in winding the superconducting coils.

During the winding process of Coil 1, the whole length of the superconducting tape and an insulation tape were firstly wound on an aluminium former simultaneously. The copper substrate in the tape was facing outward in the winding to guarantee a good thermal conduction from outside to inside since the copper has a good thermal conductivity. Following this, two current terminals made of copper bars were soldered to the internal and external ends of the coil by a low temperature solder. The dimension of each copper bar is 1.5×2 cm. Next the coil was vacuum pressure impregnated with epoxy. The impregnation process took about one day. After the resin was cured, the aluminium former in the middle was removed. Figure 6.1 shows how the voltage taps and current terminals are connected with the coil. Figure 6.2 shows the picture of the coil.

Coils 2 and 3 used some different winding techniques compared to Coil 1. The whole length of the superconducting tape and the same length of the Kapton insulation tape were wound on a tufnol former first. The tufnol former was used instead of the aluminium former is because tufnol is more suitable for low-temperature physics applications. It is soft, easy to machine and has good electrical/thermal insulation. The tufnol plates are used not only as a former but also to inject resin inside the windings. Special grooves are made to allow casting resin to penetrate the windings. An HTS joint is used to connect the two pancake coils. A laminated copper layer was soldered to the tufnol plate, and both ends of the coils gradually overlapped with the copper layer to make the current lead. The connection area between the superconducting tape and the copper layer is 25 mm long to guarantee a good joint of the current lead as shown in Fig. 6.5. The current wire can be screwed into the coil to connect with the coil current lead. Different from Coil 1, after the winding process was finished and the coils became dry, the formers were not removed to make sure there were no displacement in the windings or connections. Figure 6.3 presents the structure of Coils 2 and 3. Figures 6.6 and 6.7 give the pictures of the two small double-pancake coils (Fig. 6.4).

The differences between the winding techniques for Coil 1 and Coils 2/3 are summarised below:

Table 6.1 Configurations of superconducting coils

Coil configurations	Coil 1	Coil 2	Coil 3
Inner radius	50 mm	22 mm	22 mm
Outer radius	80 mm	24 mm	24 mm
Coil height	13 mm	10 mm	10 mm
Conductor length	100 mm	5 mm	5 mm
Turns	133	16 × 2	17 × 2
Layers	1	2	2
Coil constant	28.9 G/A	8.6 G/A	9.1 G/A
Tape width	12 mm	4.5 mm	4.5 mm
Tape	SCS12050	SCS4050	SCS4050

Fig. 6.1 Schematic drawings of coil

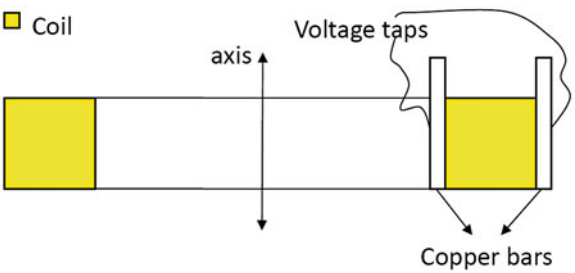
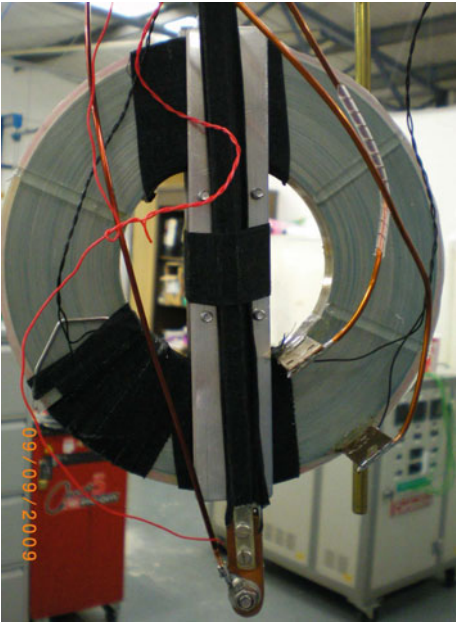


Fig. 6.2 Coil picture



- An aluminium former was used during the winding process of Coil 1 and removed afterwards. Tufnol formers were used during the winding process of Coils 2/3 and remained there after the process to guarantee there are no potential damage to the coils or displacement in the windings.

Fig. 6.3 Structure of Coils 2 and 3

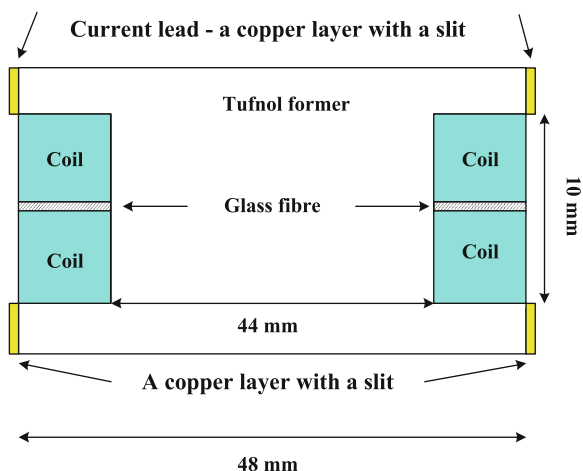


Fig. 6.4 Side view of current lead connections

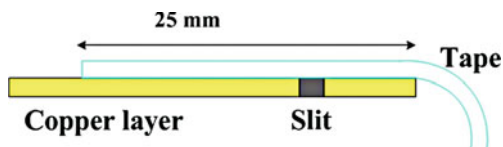
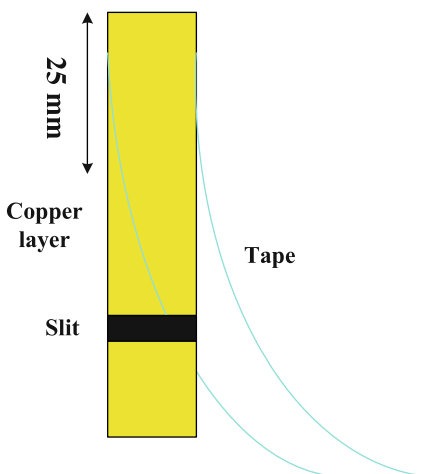
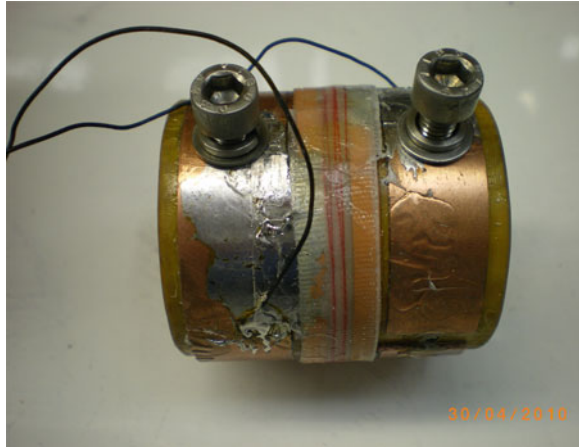


Fig. 6.5 Top view of current lead connections



- For Coil 1, two $1.5\text{ cm} \times 2\text{ cm}$ copper bar were soldered to both ends of the superconducting coil. During the soldering process the copper bar were hanging there and not fixed. For Coils 2/3, the ends of the superconducting coil were soldered to the copper layers gradually through a 25 mm long joint region. During the soldering process, both the coils and the copper layer were fixed.

Fig. 6.6 Coil 2**Fig. 6.7** Coil 3

- The connection between the current lead and the external power supply is to solder the wires together for Coil 1. However, for Coils 2/3 the wires are screwed into the current lead.

6.2 Experimental Rigs and Critical Current Measurements

6.2.1 Experimental Rig

An experiment rig using liquid nitrogen has been set up to measure this superconducting coil. This experiment rig includes a instrumented dewar, current supply, nano-voltmeter and a PC monitoring system.

Fig. 6.8 Experimental rig structure

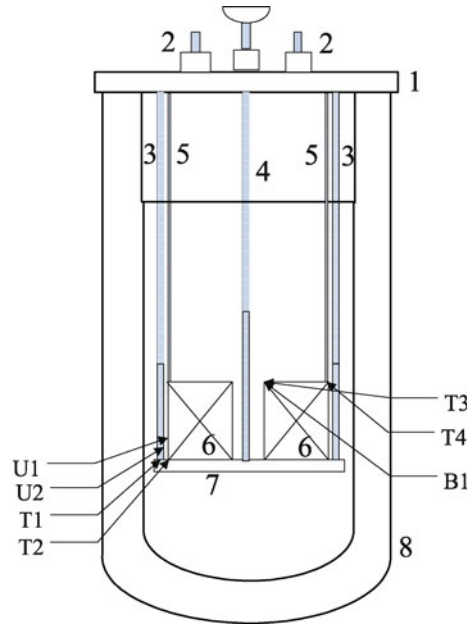


Figure 6.8 presents the structure of the dewar and its instrumentation, which includes: (1) Dewar flange, (2) Current leads, (3) Internal hanger, (4) Signal feedthrough, (5) Current leads, (6) Superconducting coil, (7) Coil supporter, (8) Dewar, Temperature sensors T1/T2/T3/T4, Voltage contact U1/U2, and Hall probe B1. Two temperature sensors are placed on the inner and outer surface, respectively. The other two temperature sensors are placed on both sides of the current lead. Two sets of voltage contacts are soldered to the coil. The hall probe is attached on the top of the inner tube, facing towards the radial direction.

Figure 6.9 shows the instrumentation on the coil. Figure 6.10 gives the connection of different components of this experiment rig.

In Fig. 6.11 we can see the picture showing the four nano-voltmeters, power supply and the PC monitoring system. A DC power supply (up to 120 A) manufactured by Cryogenic Ltd. is used as the power source.

Figure 6.12 shows the dewar already filled with liquid nitrogen and the instrumented Coil 1 was placed in it. Figure 6.13 presents how the signal feedthrough go through the dewar cover. The coil is attached on a square plastic supporter. The coil terminals are soldered to the current leads.

6.2.2 Experimental Tests of Coil 1

Coil 1 was tested at liquid nitrogen temperature. By gradually increasing the DC current in the coil, the DC voltage across the coil was measured. Figure 6.14 shows the measurement results.

Fig. 6.9 Coil with instrumentation connections

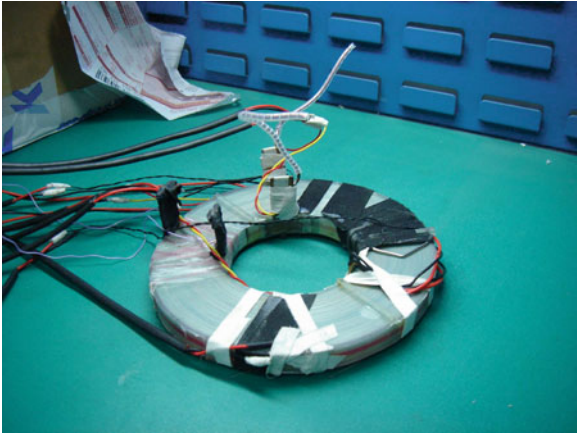


Fig. 6.10 Experimental rig structure

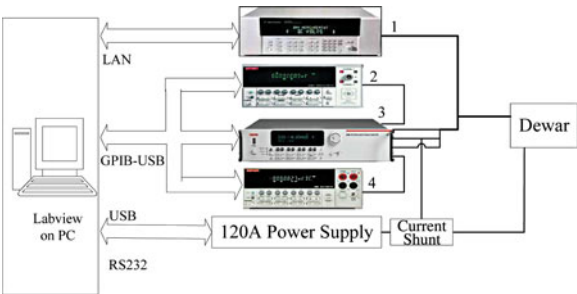


Fig. 6.11 Control and monitoring system



There are two different ways to determine the critical current of the superconducting coils by the measurement results. One method is to use the standard criterion $1\text{ }\mu\text{V}/\text{cm}$, thus the critical current of a coil would correspond to $1\text{ }\mu\text{V}/\text{cm} \times L$, where L is the total length of tapes in the coil. By this criterion the

Fig. 6.12 Dewar containing coil with instrumentation connections



critical current of Coil 1 would be the minimum transport current when the coil voltage is larger than 10 mV. The other way to determine the critical current is to observe the changing point where the $I - V$ curves becomes extremely non-linear.

From Fig. 6.14 we can see that the critical currents of the coil at 77 K in the first test is around 40 A if we use the $1 \mu\text{V}/\text{cm}$ criterion. Then the coil critical current is keeping decreasing at each test. The non-linearity of $I - V$ curves is keeping decreasing in each test, and we can see that during the fourth test the $I - V$ curve is almost a straight line.

The theoretical model which was introduced in Chap. 5 predicts the coil critical current as 80 A. Figures 6.15 and 6.16 present the current density and magnetic flux lines of the coil at the critical current. We can see the critical current is reached when the critical region just penetrates into the middle of one tape.

Clearly there are some problems with Coil 1 as suggested the measurement results. There are several possible reasons explaining the poor performance and the difference between the theoretical and experimental results of Coil 1, and they are itemised as followings:

- During the winding process, particularly when the aluminium former was removed from Coil 1, there were some displacement between the layers of the winding and a certain amount of cracks might have developed inside the tape.

Fig. 6.13 Coil with dewar cover and instrumentation connections

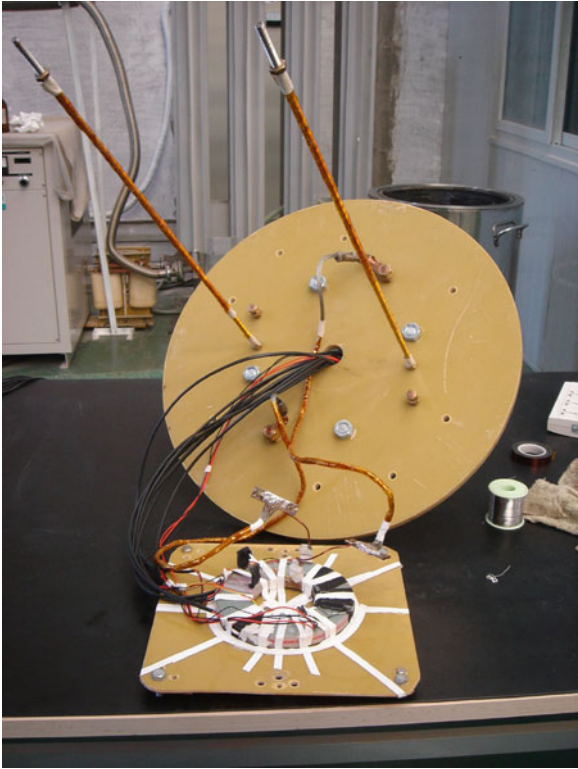


Fig. 6.14 $I - V$ curve of Coil 1 at 77 K

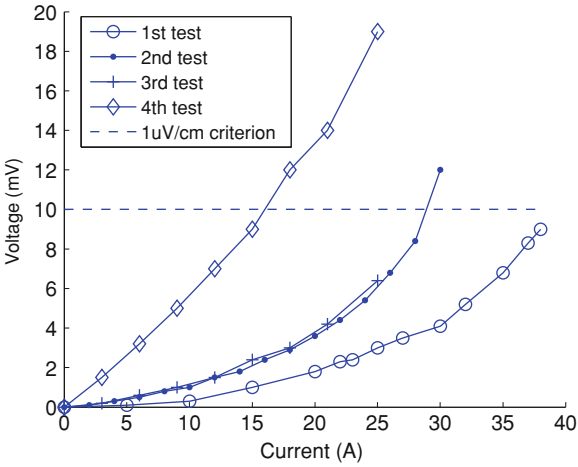


Fig. 6.15 Current density distribution of Coil 1 at 80 A, 77 K

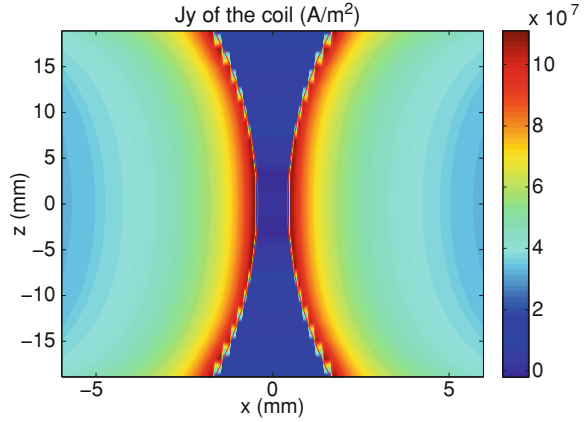
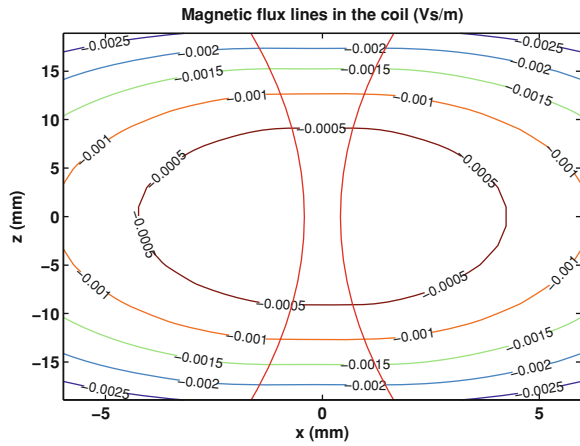


Fig. 6.16 Magnetic flux lines of Coil 1 at 80 A, 77 K



Every time a current is applied into the coil and increases, the produced heat will enlarge the cracks which would decrease the coil critical current.

- The joint between the coil ends and the copper layer was not soldered solidly since during the soldering process the copper bar were hanging there and not fixed. This poor contact would result in a large resistance and thus decrease of the critical current.

During the experiment, we also measured the temperature and the magnetic field of the coil using the temperature sensors and hall probe. Figure 6.17 gives the measured temperatures by the four temperature sensors. Since the whole coil is covered by liquid nitrogen, the coil temperature is around 77 K. The small difference between the sensors is due to the measurement error. Figure 6.18 gives the comparison of the theoretical and measured magnetic field where the hall probe is attached. We can see the two groups of values are very close to each other.

Fig. 6.17 Coil 1 temperature

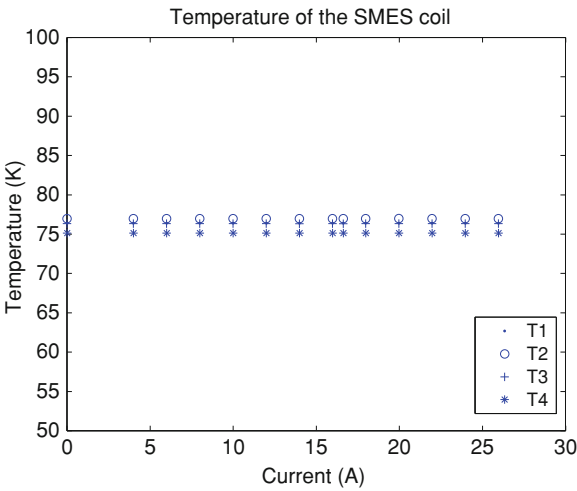
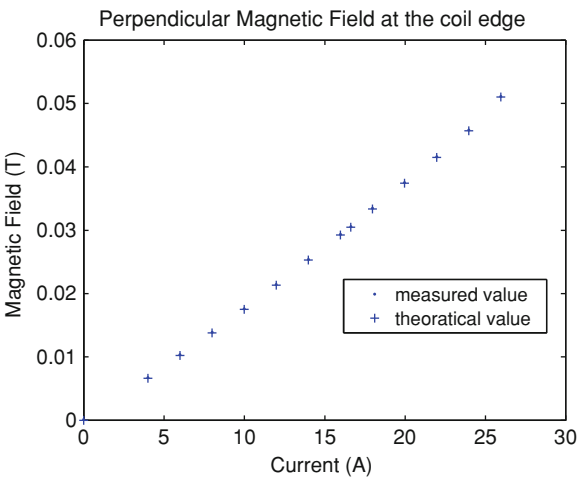


Fig. 6.18 Magnetic field at edge of Coil 1



6.2.3 Experimental Tests of Coils 2 and 3

To validate the new winding techniques, the small double-pancake Coils 2 and 3 were tested at liquid nitrogen. Also a 10 cm long tape using the same material from Superpower with an HTS joint was tested. The HTS joint in the 10 cm long tape is using the same jointing technique as those in the double-pancake coils. Figure 6.19 present the measurement results of the critical currents.

As introduced before there are two different ways to determine the critical current of the superconducting coils by the measurement results. One method is to use the $1 \mu\text{V}/\text{cm}$ criterion and the other is to observe the changing point where the

Fig. 6.19 $I - V$ curves of Coils 2/3 and HTS tape at 77 K

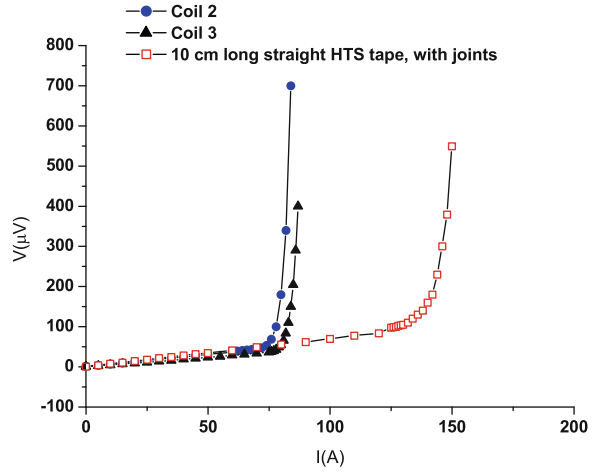
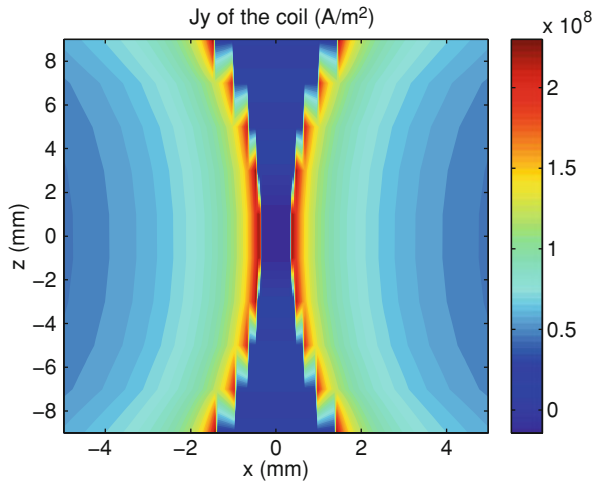


Fig. 6.20 Current density distribution of Coils 2/3 at the critical current, 77 K



$I - V$ curves becomes extremely non-linear. Since there are always some unavoidable resistance in the circuit, e.g. the joint in the current lead and between the coils. The more practical way to decide the critical current is to observe the changing point where the $I - V$ curve becomes extremely non-linear. For Coils 2/3 this sharp transition happens when the coil voltage is between $60 \mu\text{V}$ and $100 \mu\text{V}$. Thus by the second criterion the critical currents of Coils 2 and 3 are 75 and 78 A.

Coils 2 and 3 are also analysed theoretically. The calculation results predict a critical current 72 A for Coils 2 and 3. Figures 6.20 and 6.21 present the current density and magnetic flux line in and around the coil at the critical current 72 A.

Fig. 6.21 Magnetic flux lines of Coils 2/3 at critical current, 77 K

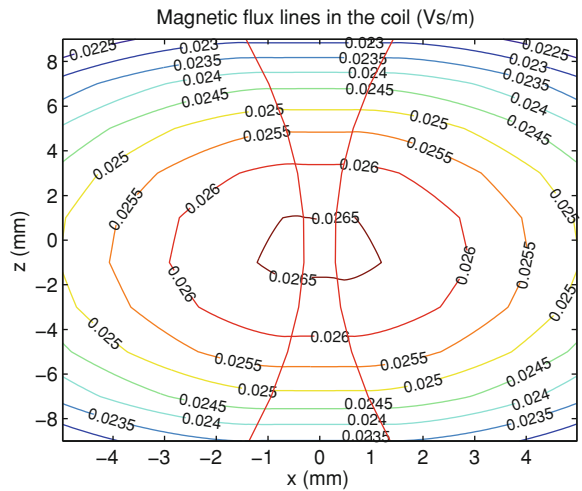


Table 6.2 Comparison of theoretical and experimental critical currents for Coils 2 and 3

	Coil 2 (A)	Coil 3 (A)
Simulation	75	78
Experiment	72	72

From the results we can see the measurement result is consistent with the theoretical result. Table 6.2 presents the comparison results. The data of $J_c(B)$ function we used in the theoretical calculation is provided by Superpower Inc. The result has validated that our simulation model is able to predict critical currents of HTS pancake coils.

To investigate the coil performance in a background field, we applied different external magnetic fields to Coil 2 and measured the critical currents accordingly. The magnetic field was applied in parallel with the z -axis of the coil, which also meant the field was in parallel with the tapes in the coil. Figure 6.22 presents the experimental set-up that was used to test Coils 2/3 in a background magnet field. It is a cryogen free system. Coils 2 and 3 are inserted through the hole 5 as showed in Fig. 6.22 in the experiment.

Figure 6.23 gives the experimental results. As discussed before, the $I - V$ curves become very non-linear when the coil voltage is between 60 and 100 μV , this is also true for the coils in a background field. Thus we use these two different values, 60 and 100 μV , to define the coil critical currents. Figure 6.24 present the critical currents of Coil 2 in different background fields. We can see that the critical current is keeping decreasing. This is because the critical current of the superconducting tapes would decrease when the applied field is increasing. When there is no external magnetic field, the critical current of Coil 2 is higher than 75 A. When the applied field is 5 T, the critical current decreases to only 8 A.

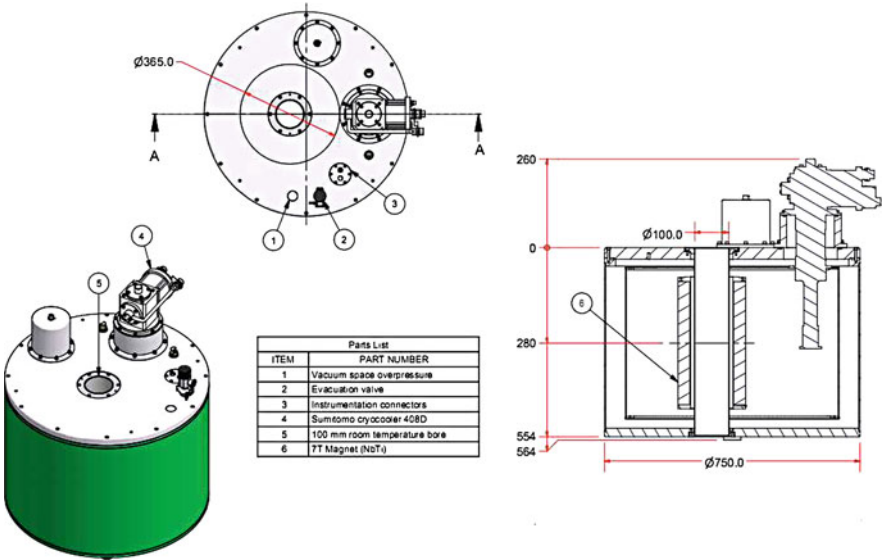
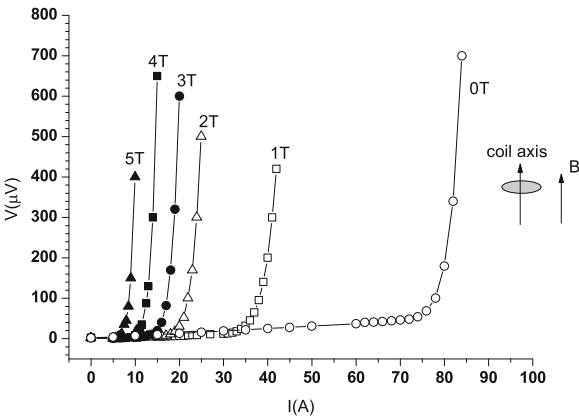


Fig. 6.22 Experimental set-up for testing superconducting coils in background field

Fig. 6.23 *I* – *V* curve of Coil 2 at 77 K in different background fields applied parallel to axis of coil



6.2.4 Experimental Rig Using a Cryocooler

This SMES coil is aiming to work between 20 and 30 K eventually, thus a cryostat working with a cryocooler is designed and built up.

The coil will be cooled down by a cold head in a cryogen-free cryostat. We are using a two-stage M-350 CP cold head from CTI-Cryogenics. This cold head can provide a heat lift of 4 W at 20 K and 20 W at 77 K simultaneously. Figure 6.25 gives the cooling capacity of the two stages at different temperatures.

Fig. 6.24 Critical currents of Coil 2 at 77 K in different backgrounds by two different voltage criteria

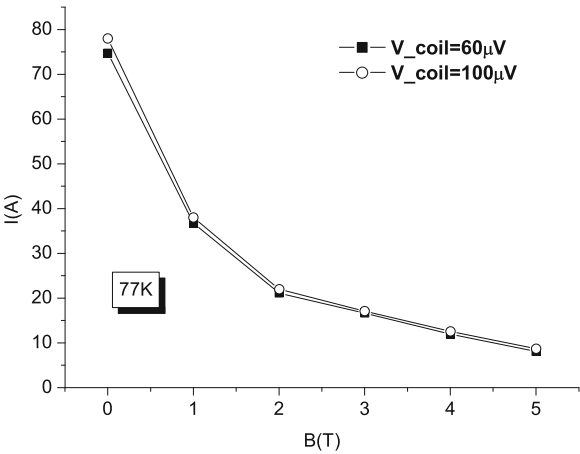


Fig. 6.25 Typical refrigeration capacity of cryocooler at 50 Hz

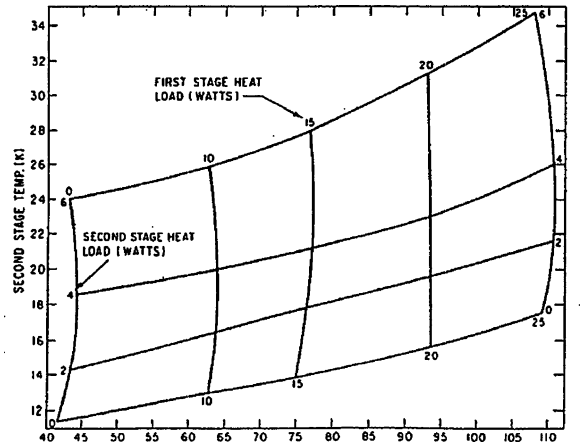


Figure 6.26 gives the view of the cold head structure. Figure 6.26 presents the photo of the cold head lying on top of a compressor (Fig. 6.27).

Figure 6.28 gives the picture of the pump that will be used to vacume the cryostat. Figure 6.29 presents the compressor which is working with the coldhead.

Figure 6.30 gives a typical vacuum process of the cryostat. A forevacuum pump is firstly switched on. When the vacuum pressure reaches around 1 mbar a turbo pump is switched on to achieve a much better vacuum. Usually after 30 min the vacuum level can go down to the same order of magnitude with 10^{-4} mbar. Figure 6.31 gives a typical cooling process of the cold head without any heat load. It normally takes around 30 min to reach the minimum temperature which is about 30 K.

Fig. 6.26 Cold head structure

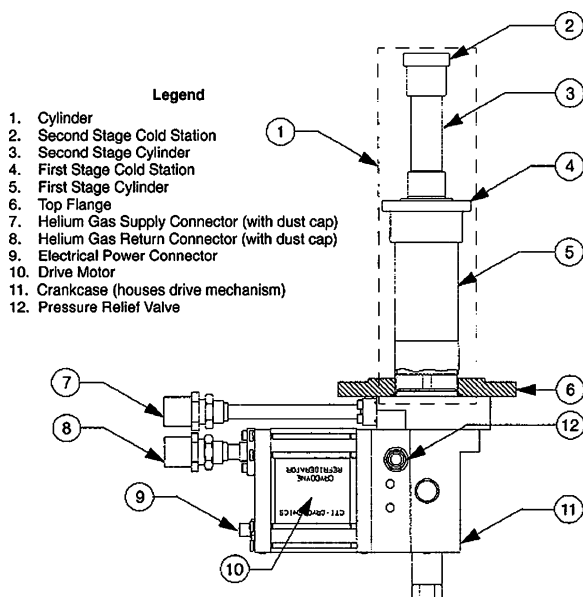
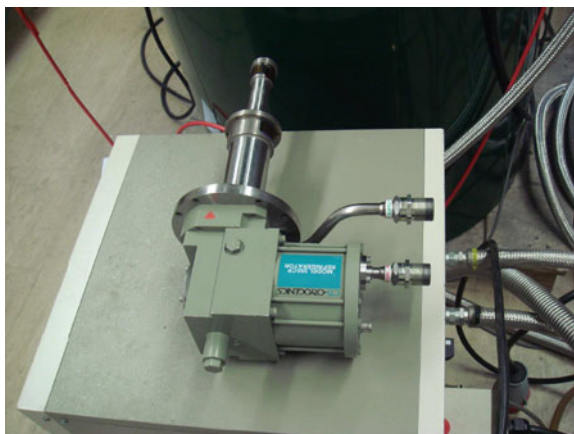


Fig. 6.27 Cold head photo



6.3 AC Losses of the Coil

6.3.1 Theory and Experiment of AC Losses in Literature

The AC losses of the type II superconductor are coming from the non-linear $M - H$ loop of the superconductor. During the magnetisation and demagnetisation process of superconductors, the hysteresis losses of the $M - H$ loop will behave like a 'resistance' of the superconductors.

Fig. 6.28 M-350 CP cryocooler

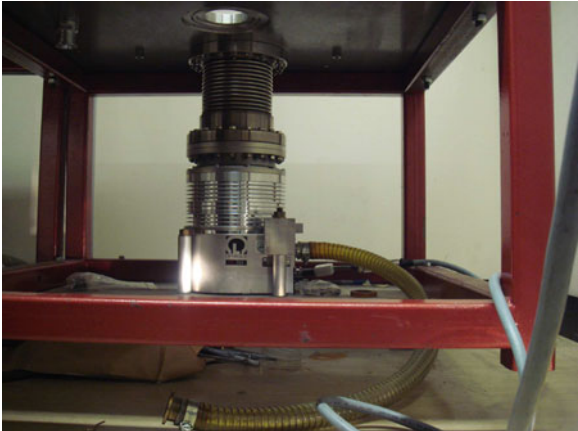


Fig. 6.29 Compressor for the cold head



Fig. 6.30 Cryostat vacuum pressure

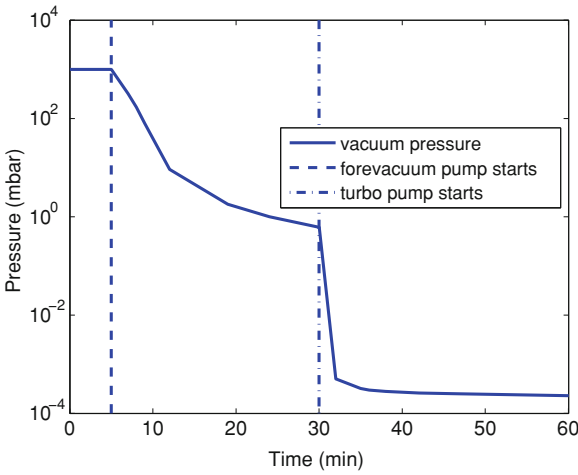
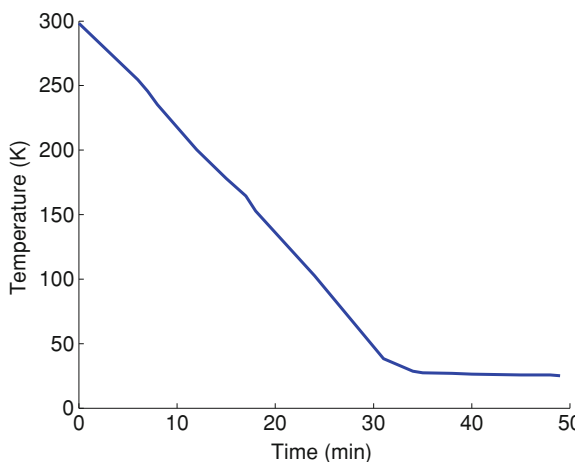


Fig. 6.31 Cool down process of cold head without heat load



Norris has analysed the AC losses in a superconductor with different shapes using the critical state model [1, 2]. In his paper, he analysed the superconductor with different configurations such as round, elliptic, rectangular, cruciform-sectioned and a thin strip with a finite width. Analytic formulas have been given to calculate the AC losses quickly.

However, Norris' method cannot cope with HTS materials very well due to its high anisotropic characteristics. Brandt et al. have given a different analytic method to calculate the AC losses in superconducting strips [3, 4]. Their calculations have been validated by experimental results.

There are two ways to measure the AC losses in the superconductor, the calorimetric method and electrical method. A calorimetric method to measure the AC losses in superconducting tapes were introduced in [5–7]. Figure 6.32 presents the measurement system. This system can measure AC losses when the superconductors are carrying transport AC currents in external AC magnetic fields at variable temperatures. The variable temperature is achieved by a thermal connection between the sample and a cooling machine. The AC losses can be calculated by comparing the temperature rise of the sample to the temperature rise caused by a reference heater. The other way is to calculate the increase in power dissipation of the sample which is compensated for by a reduction of the power dissipation in the heater.

The other method to measure AC losses in superconductors is using electrical methods. Figure 6.33 gives an example circuit [8–11]. When measuring AC loss in a short superconducting sample, a compensation coil is used to eliminate the inductive part of the voltage, so that only the in-phase component remains, i.e. the purely resistive voltage. A lock-in amplifier is used to detect voltage signals in-phase with the operating current, as well as serving as a signal source for the AC power supply. Therefore the resistive part in the sample can be collected and the AC losses can be calculated.

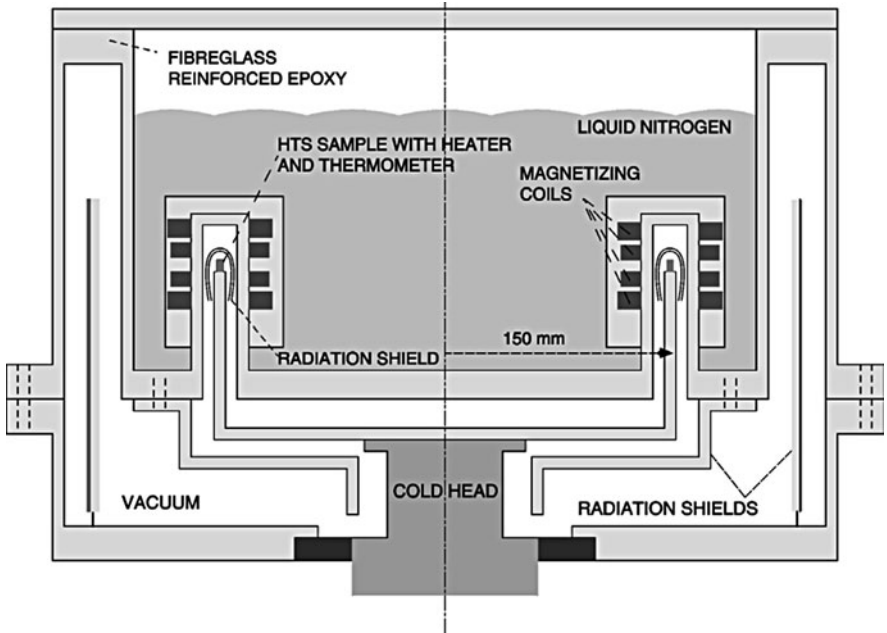


Fig. 6.32 AC loss measurement system using a calorimetric method

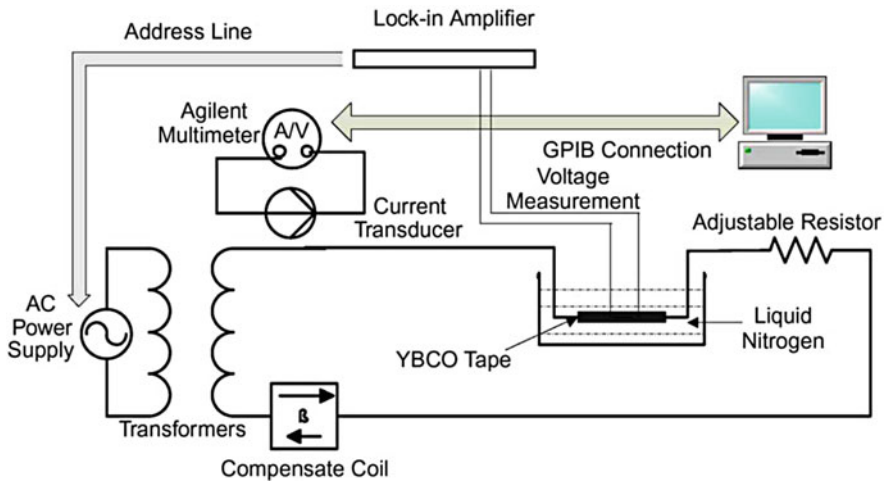


Fig. 6.33 AC loss measurement system using a electrical method

The techniques for measuring AC losses of superconducting tapes have already been tested and validated as introduced above. However, measuring AC losses of superconducting coils are much more difficult, since their large inductance will produce a large inductive voltage which makes it difficult to pick up the resistive voltage.

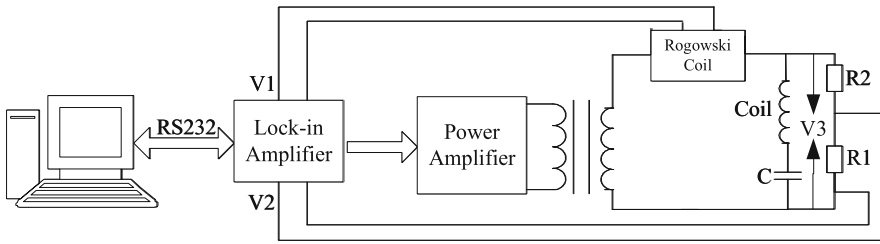


Fig. 6.34 Circuit to measure coil AC losses

6.3.2 Experimental Rig of AC Losses Measurement at 77 K

One way to measure AC losses is to cancel the large inductive voltage by a capacitor. Figure 6.34 shows the circuit we used to measure the AC losses of the coil. The lock-in amplifier sends out a standard AC signal, which is amplified by the power amplifier. Then it is sent to the transformer which increases the AC current. When an AC current goes through the coil and capacitor, the capacitor compensates the inductive voltage on the coil. When L and C have the relation $\omega_0 = \frac{1}{\sqrt{LC}}$, the circuit is at resonance. This means the inductive voltage is fully compensated, and the coil and capacitor will behave together like a pure resistance. The resistance is exactly coming from the AC losses of the coil.

Rogowski coil picks up the amplitude and phase of the current in this coil, transfer it to the voltage signal and finally send it to the lock-in amplifier. The voltage signal V1 picked up by Rogowski coil is 90° ahead of the coil current, we need to use the lock-in amplifier to lock the voltage signal V2 which is 90° behind V1, and this represents the resistive voltage. We can get the resistive voltage by measuring V1. The reason why we don't measure V3 directly is that it is large enough to damage the lock-in amplifier, thus we use a voltage divider consisted of R1 and R2. The resistance of R1 and R2 together is much larger than the impedance of the coil and capacitor, thus R1 and 2 will behave like an open circuit and not affect the circuit. The resistance of R2 is ten thousand times of R1, therefore by measuring V2, i.e. the voltage of R1, we can calculate the voltage V3.

During the measurement, we firstly choose a frequency, then calculate how much capacitance we need to fully compensate the inductive voltage. We monitor the coil current and V3 together using an oscilloscope while we are slightly tuning the frequency sent out from the lock-in amplifier. When the current and voltage are in the same phase, the circuit is at resonance. Then we use the lock-in amplifier to lock and measure the resistive voltage V2. At the same time we measure the Rogowski coil voltage V1, from which we can calculate the coil current. By timing the coil current and the resistive voltage $V2 \times \frac{R2}{R1}$, we can calculate the AC losses of the coil.

An experiment rig to measure the coil AC losses has been set up. Figure 6.35 presents the experiment circuit. This circuit was built based on Fig. 6.34

Fig. 6.35 Experimental set-up for measuring coil AC losses

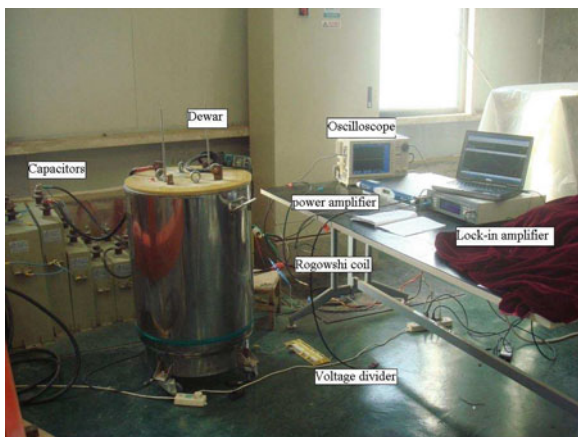
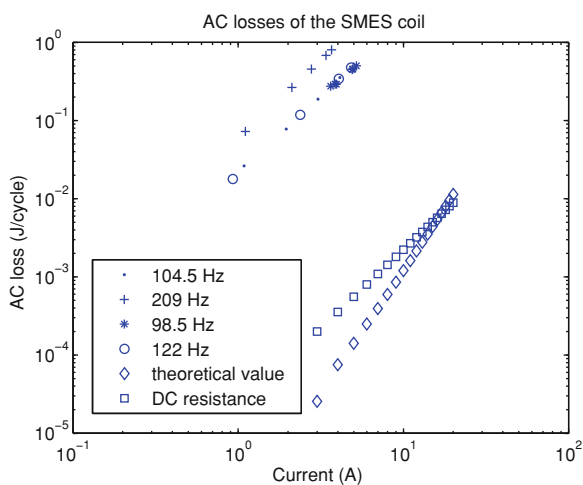


Fig. 6.36 AC loss comparison between measurement and numerical modelling

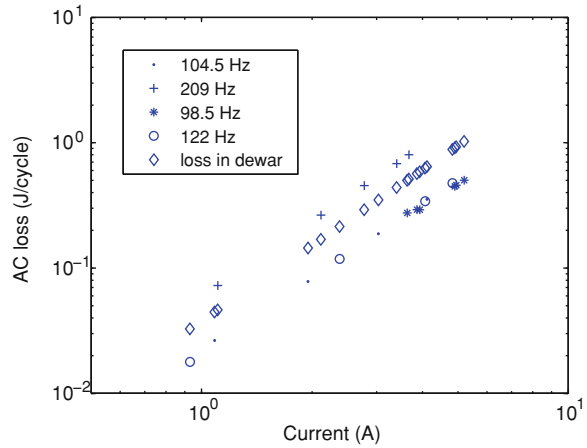


6.3.3 Measurement Results and Analysis

Figure 6.36 presents the comparison of the measured AC losses of the coil at different frequencies with the theoretical calculation. We can see that there is a large discrepancy between the theoretical values and experimental values.

The initial thought about this discrepancy is that the measured losses might be due to the DC resistance in the coil. Figure 6.14 shows that there might be some crack, which would result in a relatively large DC resistance, in the pancake coil 1. Thus we calculated the DC resistance according to Fig. 6.14 and then calculated the AC losses. The result is also included in Fig. 6.36. We can see that the electrical losses due to the coil DC resistance is still much lower than the measured values. Thus the measured losses are not caused by the coil DC resistance.

Fig. 6.37 AC loss comparison between measurement results and calculated losses in dewar



The discrepancy of the experimental results between 209 Hz and lower frequencies is because the rated working frequency of the capacitor is below 200 Hz. If the frequency is higher than 200 Hz, there will be a certain amount of error.

From Figs. 6.12 and 6.13 we can see that when the coil is placed in the dewar, it is co-axial with the dewar which is made of stainless steel. When an AC current is applied into the coil, the changing magnetic field will induce a voltage potential and thus a current in the dewar and vice versa. Thus the measured AC losses are actually the electrical losses in the dewar. The electrical losses in the dewar can be predicted by calculating the changing magnetic field and considering the electrical resistivity of the stainless steel. The calculation results are presented by Fig. 6.37. We can see the measured values are in the same order of magnitude with the losses in the dewar.

6.4 Control Circuit for SMES Applications

The control circuit is an essential component of a SMES system [12, 13]. The control circuit needs to discharge the SMES system quickly when its energy is needed and charge it when its stored energy is less than the rated value.

For traditional LTS SMES, there is a persistent model in which the superconducting current is flowing in the closed circuit and never decreases since there is no resistance in the SMES coil [14]. However, for HTS SMES, a persistent mode cannot be achieved since there is still little resistance in the SMES coil due to $E - J$ power law, and also the HTS superconducting joint resistance is around $10^{-7} \Omega$ which is not small enough as a persistent switch. Additionally there is resistance in the diodes that is used in the control circuit. Therefore there are only two operation modes for HTS SMES, the charge and discharge modes.

Fig. 6.38 SMES coil charging circuit

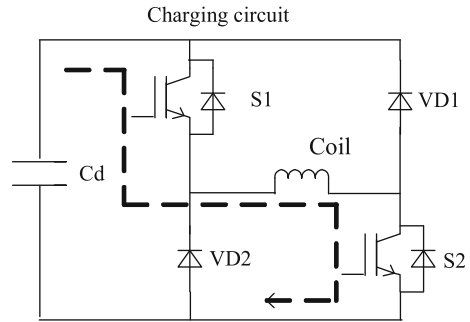
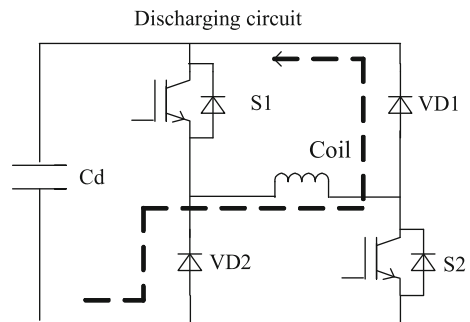


Fig. 6.39 SMES coil discharging circuit



Since a SMES system stored the energy in the form of a DC current, power electronics converters are needed to convert the DC current into AC current so that a SMES system can have energy transfer with the external circuit.

6.4.1 Chopper Circuit to Charge and Discharge the Coil

A charge and discharge circuit for a SMES coil can also be called as a chopper. A chopper is needed to control the energy flow direction between the SMES system and the external circuit. Figures 6.38 and 6.39 present the circuit of a typical chopper for a SMES.

The chopper consists of a capacitor C_d , two IGBTs S1 and S2, and two diodes VD1 and VD2. The chopper manages the conversion between the SMES coil current and the H-bridge converter voltage. It increases operation safety by isolating the SMES magnet from the power system. It also controls the current flow of the SMES by switching S1/S2 on and off. During the charge process the current will go through S1 and S2, and during the discharge process the current will go through VD1 and VD2.

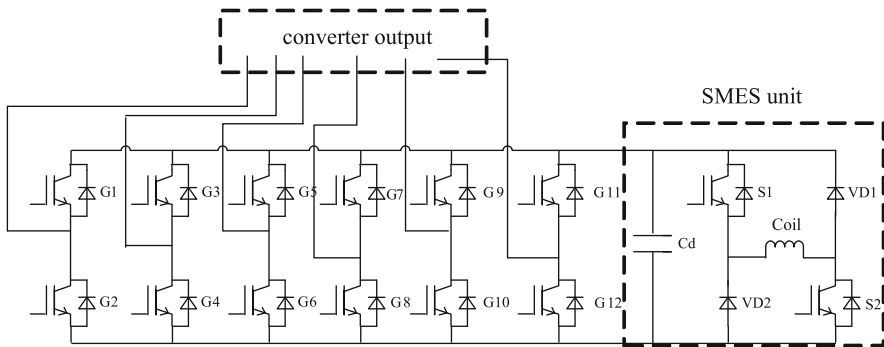


Fig. 6.40 Power electronics converters and SMES unit

6.4.2 Power Electronics Converter

Figure 6.40 shows the converters and the SMES unit. The converters include three single-phase H-bridge converters. Each H-bridge converter consists of four power electronics transistors (insulated-gate bipolar transistor, IGBT). These converters are able to convert DC voltage from the SMES coil to AC voltage in the power system. Three independent converters for three phases are used to decouple the influence between each phase, thus the SMES system can supply unsymmetrical three-phase power as well as symmetrical three-phase power. This kind of converter is superior to the traditional voltage-source converter since it uses a DC voltage more efficiently and control the voltage more flexibly [15–17].

6.5 Experiment of Chopper Circuit

To validate the control strategy for charging and discharging the coil, we have built up and tested a chopper circuit.

Figure 6.41 presents the chopper circuit for charging and discharging the SMES coil. During the charge mode, the capacitor is charged by the power source. S7 is always turned on, S8 is turned on and off by PWM with a certain duty ratio. Thus the coil is charged. During the discharge mode, S7 and S8 are turned off. The current flows through the diodes in S9 and S10. The coil discharges the energy back to the capacitor. A $100\ \Omega$ is connected in parallel with the capacitor as a dump resistor.

Although there is no literally persistent mode, we can still operate in a ‘persistent’ mode that the current would quickly decrease due to the coil resistance. S8 is turned off in a ‘persistent’ mode and the current is flowing in loop 1.

Figures 6.42 and 6.43 present the photos for the chopper and the experimental set-up.

Coil 1 was used in the experiment. During the experiment, initially a square wave signal was sent to S8 to control its on and off, thus the circuit is switched between the

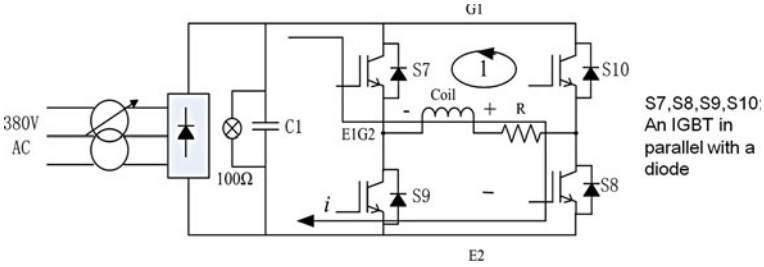


Fig. 6.41 SMES coil chopper circuit

Fig. 6.42 SMES coil chopper circuit

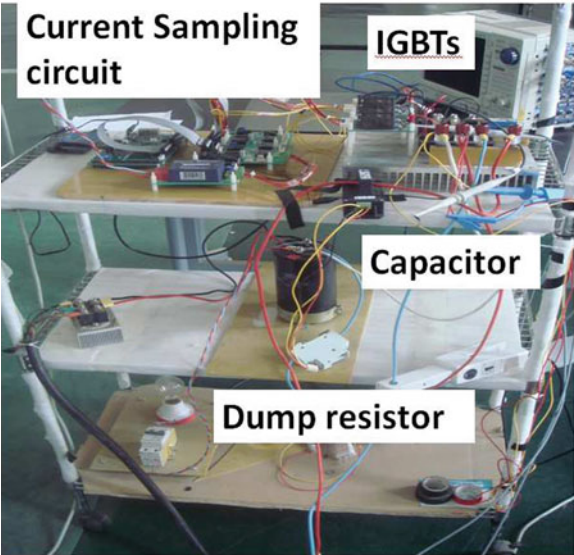


Fig. 6.43 Experimental set-up for testing chopper circuit

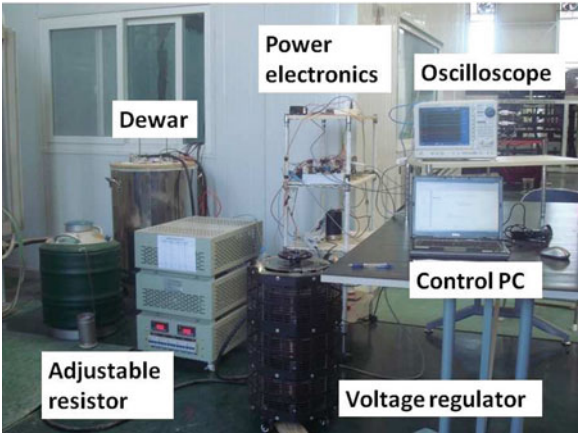


Fig. 6.44 Coil voltage and current during discharge mode

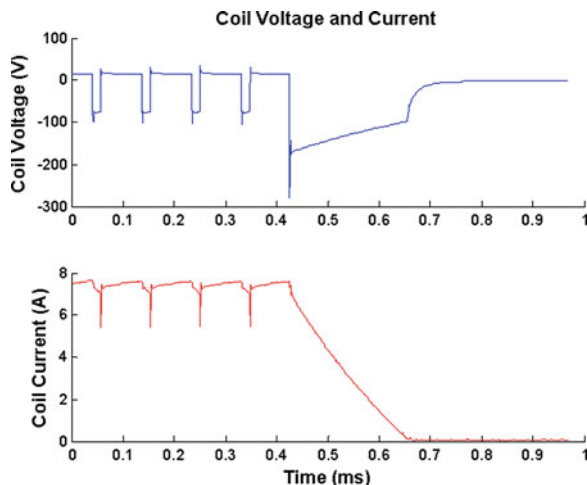
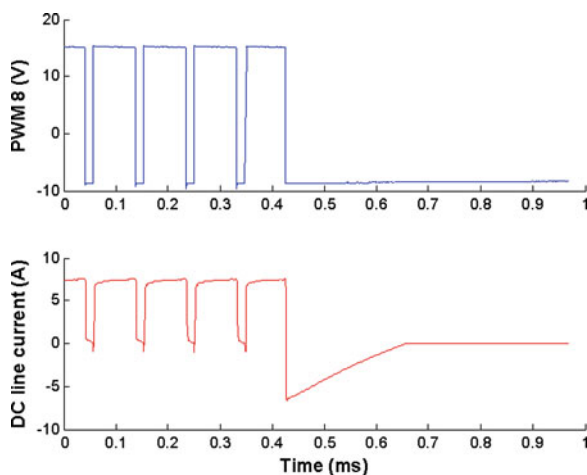


Fig. 6.45 S8 signal and DC line current during discharge mode



charge and open-circuit mode, the current was charged into the SMES coil. In the discharge experiment as shown in Figs. 6.44 and 6.45, at $t = 0.45$ s the circuit was switched into the discharge mode, we can see that within 0.3 ms the current in the coil was completely discharged, the coil voltage also reduced to zero. Figure 6.45 gives the duty ratio of the initial square wave. The DC line current direction was opposite in the discharge mode as opposed to the charge mode.

Figures 6.46 and 6.47 present the coil performance in the ‘persistent’ mode. A square wave signal was also sent to S8 to control the charge of the SMES coil at the beginning. At $t = 1.2$ ms the coil was turned into the ‘persistent’ mode, i.e. S8 was turned off and thus the current was forced to flow in loop 1. We can see that within 2 ms the current and voltage completely decreased to zero after the coil was turned into the ‘persistent mode’. Figure 6.47 gives the duty ratio of the initial

Fig. 6.46 Coil voltage and current during 'persistent' mode

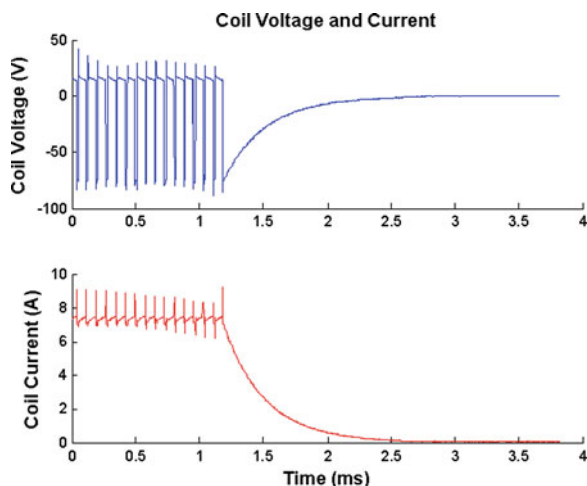
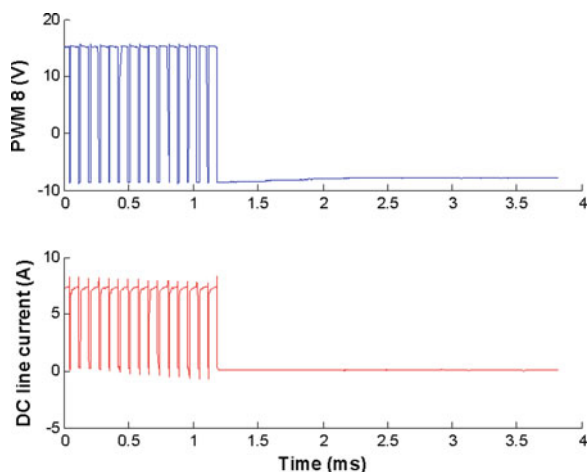


Fig. 6.47 S8 signal and DC line current during 'persistent' mode



square wave. The DC line current direction was zero in the 'persistent' mode which validated the 'persistent' mode since all the current was flowing in loop 1.

6.6 Simulation and Experiment of Voltage Sag Compensation

6.6.1 System Circuit and Control Strategy

One important application of SMES systems is to compensate a voltage sag in a power system. A voltage sag in a power system will damage the sensitive electrical load and equipment. Connected to a power system through a power electronics

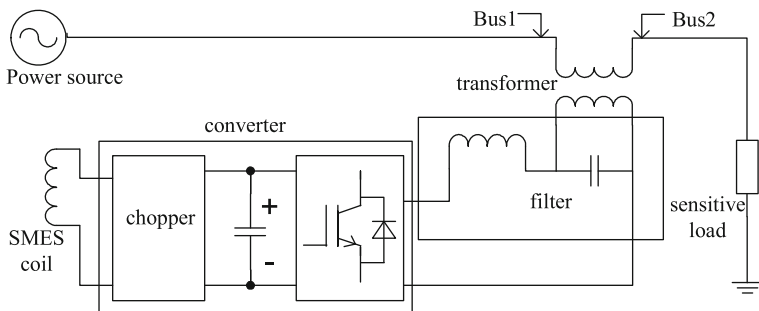
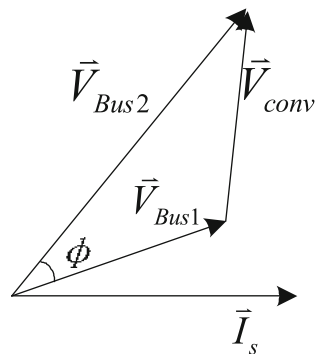


Fig. 6.48 Connection of SMES unit with power system

Fig. 6.49 Voltage sag compensation



control circuit, a SMES system can release its energy within several milli-seconds with a high cyclic efficiency to recover the voltage.

The connection of the SMES system with the power system is shown in Fig. 6.48, it includes a SMES unit, a chopper, a voltage-source power electronics converter and a low-pass filter. The SMES system is connected to the power system with an isolation transformer. During the operation, if a voltage sag at Bus1 is detected, the SMES system will release its energy to compensate the voltage sag and maintain the Bus2 voltage at a constant value. Therefore, the important sensitive load is protected.

Figure 6.49 shows the compensation process. In the normal condition the sensitive load requires a voltage V_{Bus2} . During a voltage sag, the voltage at Bus1 will drop to V_{Bus1} . The voltage value decreases and the phase shifts compared to the normal condition. The control circuit will release the SMES energy to produce a compensation voltage V_{conv} , and this V_{conv} will keep the load voltage V_{Bus2} the same as the normal condition.

Figure 6.50 shows the algorithm to calculate the compensation voltage. Since it is difficult to analyse the control model in Cartesian coordinates, firstly we need to

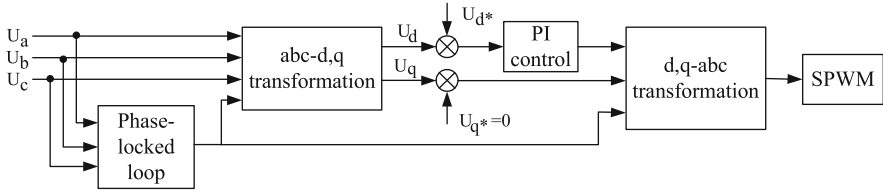


Fig. 6.50 Control algorithm to calculate compensation voltage

transform the symmetric three phase voltages to d, q -axis voltage components with phase-lock technique to decouple the three phase power system. Equations 6.1–6.3 shows the transformation. U_i ($i = a, b, c$) is the phase voltage in Cartesian coordinates, U_d and U_q are the d, q -axis voltage components, $T_{abc/dq}$ is a coordinate transformation matrix, V is the virtual value of phase voltage U_i .

$$[U_d, U_q]^T = T_{abc/dq}[U_a, U_b, U_c]^T \quad (6.1)$$

$$T_{abc/dq} = \sqrt{\frac{2}{3}} \begin{bmatrix} \sin \omega t & \sin(\omega t - \frac{2}{3}\pi) & \sin(\omega t + \frac{2}{3}\pi) \\ \cos \omega t & \cos(\omega t - \frac{2}{3}\pi) & \cos(\omega t + \frac{2}{3}\pi) \end{bmatrix} \quad (6.2)$$

$$\begin{bmatrix} U_d \\ U_q \end{bmatrix} = \begin{bmatrix} \sqrt{3}V \\ 0 \end{bmatrix} \quad (6.3)$$

Secondly, considering the voltage U_q is a constant 0 for a symmetric three phase voltages in Eq. 6.3, we only need to compensate the voltage U_d . Then we compare the monitored U_d with the normal reference voltage U_d^* and we can get the compensation voltage ΔU_d given by Eq. 6.4.

$$\Delta U_d = U_d^* - U_d \quad (6.4)$$

After proportional integral (PI) control and transferring the d, q -axis voltage back to the normal three phase voltage system, we can send it as sinusoidal pulse width modulation (SPWM) signal to the converter, which will produce the compensation voltage needed in power system. The compensation voltage U_{i-conv} ($i = a, b, c$) are as following:

$$[U_{a_conv}, U_{b_conv}, U_{c_conv}]^T = T_{dq/abc}[\Delta u_d, u_q]^T \quad (6.5)$$

where $T_{dq/abc}$ is the inverse matrix of $T_{abc/dq}$.

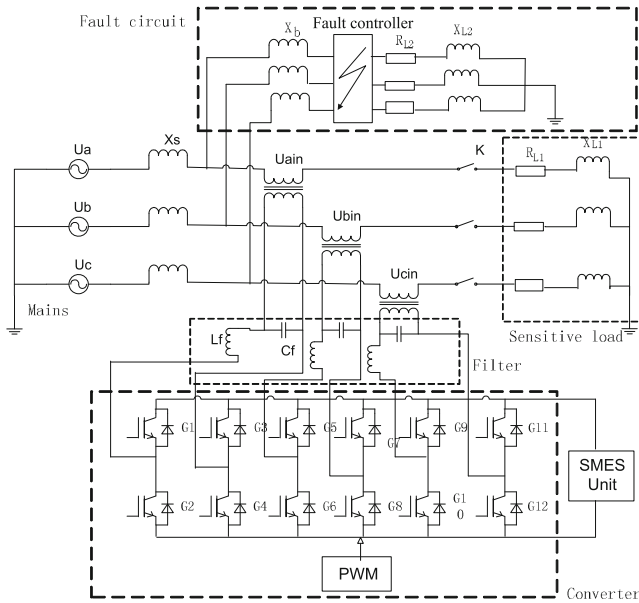


Fig. 6.51 Experiment circuit

Figure 6.51 shows the whole system circuit. It includes the SMES unit, a voltage-source converter, a low-pass filter, an isolation transformer, a power source, a fault circuit and a sensitive load.

The Bus1 voltage is monitored and sent into a digital-signal processor DSP2812 by the sampling circuit at 5 K sampling rate. The processor compares the sampling voltage with the reference normal voltage. If a voltage sag happens, the processor will calculate the difference, send the driving PWM signal to the converter and produce the compensation voltage needed. Then the voltage is filtered by the filter circuit and sent to the power system through the transformer. By the process above, the load voltage is maintained at a normal value during a voltage sag.

The filter circuit consists of a capacitor and an inductance. The output voltage of the converter includes the normal 50 Hz component and high-frequency harmonics. The filter circuit will filter the harmonics and pass the normal 50 Hz component through.

There are three transformers U_{ain} , U_{bin} and U_{cin} in three phases to transform the converter output voltage to the power system voltage.

In the main system circuit, U_a , U_b and U_c are a three-phase power source. X_s is the impedance of the transmission lines. R_{L1} and X_{L1} are the important sensitive load which requires a constant voltage. Fault circuit consists of X_b , X_{L2} , R_{L2} and a fault controller. This fault circuit is able to produce a voltage sag on Bus1.

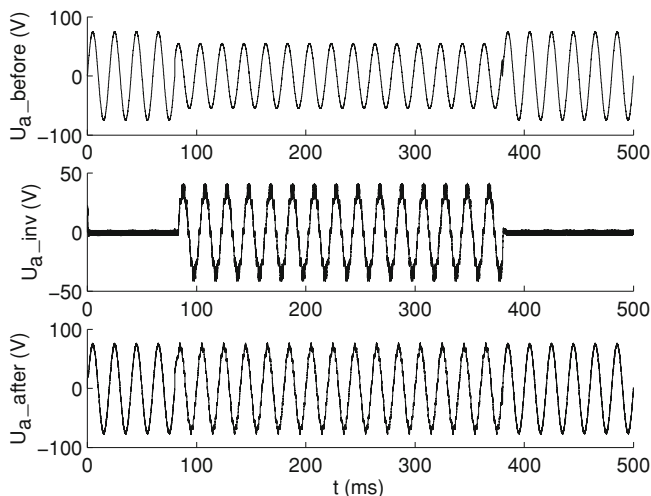


Fig. 6.52 Simulation results of U_a before compensation, converter voltage and U_a after compensation

6.6.2 Simulation Results

To demonstrate the performance of the SMES in a voltage sag, we first built the whole system in Matlab/Simulink. The whole system was modelled according to Fig. 6.51. Since the three-phase voltages are symmetrical, we just take phase A for example. The Phase A voltage will be dropped for about 300 ms. Figure 6.52 gives the simulation result. We used a 50 Hz voltage. The peak value of the normal voltage before compensation was 75 V. A voltage sag happened at $t = 75$ ms. Immediately after the voltage sag happened, the converter released the SMES energy and produce a compensation voltage. The total voltage after compensation is maintained at 75 V. The simulation result validates the control strategy of the SMES system.

6.6.3 Experiment Results

An experimental rig was set up to test the SMES system as well. This experiment system was also built up according to Fig. 6.51. Figure 6.53 presents the picture of the power electronic converter and the chopper for the SMES coil. Figure 6.54 shows the components of the experimental set-up. A voltage source was used instead of superconducting coils to guarantee a stable energy supply since the inductance of Coil 1 is not big enough. However, the control strategy is still the same and this experiment would also be able to validate the control circuit.

Fig. 6.53 Power electronic converter and chopper

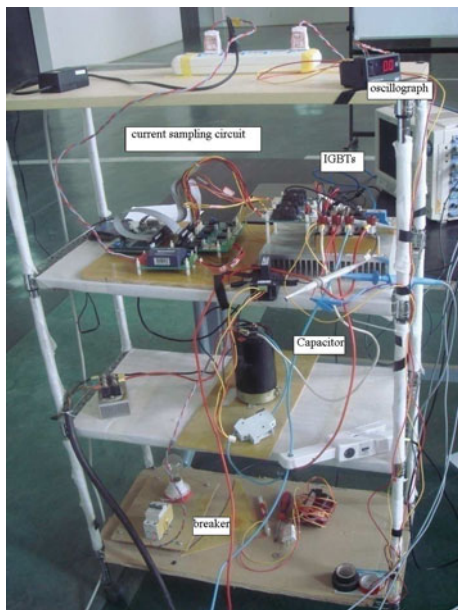
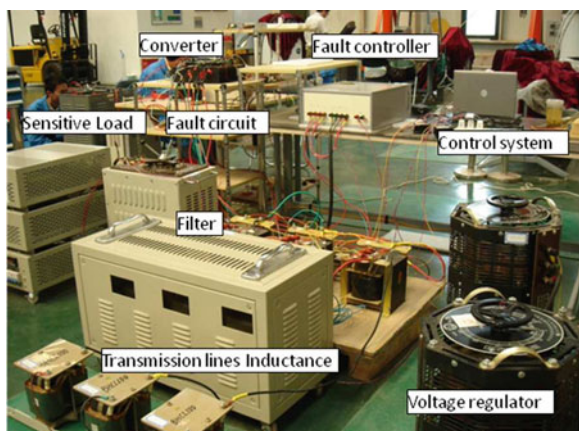


Fig. 6.54 Experimental set-up of complete voltage sag compensation system



Again, we are using a 50 Hz 75 V(peak value) voltage. At $t = 75$ ms a voltage sag happened, the converter produced a compensation voltage. Figure 6.55 presents the experiment result. We can see that there are a few spikes in the compensation voltage since the high-frequency harmonics cannot be completely filtered by the filter in the real experimental set-up. However, the SMES system still compensated the voltage sag successfully. The voltage after compensation is kept at the normal value.

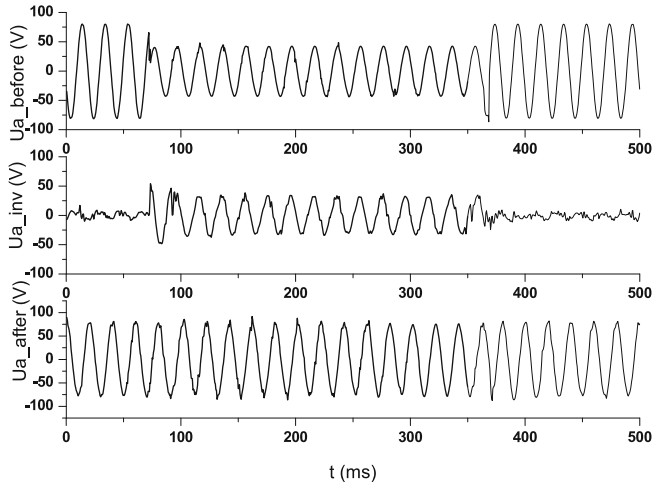


Fig. 6.55 Experiment of U_a before compensation, converter voltage and U_a after compensation

In conclusion, [Sect. 6.4](#) introduces the control circuit for the SMES system. [Section 6.5](#) presents the experiment for a chopper circuit which can charge and discharge the superconducting coils. In [Sect. 6.6](#) the simulation and experimental results both validated the control strategy for the SMES system as shown. The energy in the SMES system can be quickly dumped into an electric power system to compensate a voltage sag.

References

1. Norris WT (1970) Calculation of hysteresis losses in hard superconductors carrying AC: isolated conductors and edges of thin sheets. *J Phys D: Appl Phys* 3(4):489–507
2. Campbell AM, Evetts JE (1972) Flux vortices and transport currents in type II superconductors. *Adv Phys* 21(90):199–429
3. Helmut Brandt E, Indenbom M (1993) Type-II-superconductor strip with current in a perpendicular magnetic field. *Phys Rev B* 48(17):12893–12906
4. Zeldov E, Clem JR, McElfresh M, Darwin M (1994) Magnetization and transport currents in thin superconducting films. *Phys Rev B* 49(14):9802–9822
5. Magnusson N, Hornfeldt S, Rabbers JJ, ten Haken B, ten Kate HHJ (2000) Comparison between calorimetric and electromagnetic total AC loss measurement results on a BSCCO/Ag tape. *Supercond Sci Tech* 13(3):291
6. Magnusson N, Schonborg N, Wolfbrandt A, Hornfeldt S (2001) Improved experimental set-up for calorimetric AC loss measurements on HTSs carrying transport currents in applied magnetic fields at variable temperatures. *Phys C Supercond* 354(1–4):197–201
7. Magnusson N, Hornfeldt S (1998) Calorimetric apparatus for alternating current loss measurements on high-temperature superconductors. *Rev Sci Instrum* 69(9):3320–3325
8. Pei R, Velichko A, Jiang Y, Hong Z, Katayama M, Coombs T (2008) High-precision digital lock-in measurements of critical current and AC loss in HTS 2G-tapes. 3147–3150

9. Pei R, Velichko A, Hong Z, Jiang Y, Yuan W, Campbell AM, Coombs TA (2009) Numerical and experimental analysis of IC and AC loss for bent 2G HTS wires used in an electric machine. *Appl Supercond IEEE Trans* 19(3):3356–3360
10. Pei R, Velichko A, Majoros M, Jiang Y, Viznichenko R, Hong Z, Marchant R, Campbell AM, Coombs TA (2008) IC and AC loss of 2G YBCO tape measurement for designing and fabrication of an HTS motor. *Appl Supercond IEEE Trans* 18(2):1236–1239
11. Ghoshal PK, Coombs TA, Fair R, Campbell AM (2007) Experimental set up to measure AC losses of HTS in rotating magnetic field. *Appl Supercond, IEEE Trans* 17(2):3199–3202
12. Shao-rong W (2007) Apparatus and experiment of high temperature superconducting magnetic energy storage used for power system stability enhancement. *Proc Chin Soc Electr Eng* 27:44–50
13. Xun L (2004) Voltage sag compensation by SMES. *Chin Autom Elect Power Syst* 28:44–50
14. Wilson MN (1983) *Superconducting Magnets*. Oxford University Press, Oxford
15. Iglesias JJ, Acero J, Bautista A (1995) Comparative study and simulation of optimal converter topologies for SMES systems. *Appl Supercond IEEE Trans* 5(2):254–257
16. Choi SS, Li BH, Vilathgamuwa DM (2000) Dynamic voltage restoration with minimum energy injection. *Power Syst IEEE Trans* 15(1):51–57
17. Yu J, Duan X, Tang Y, Yuan P (2002) Control scheme studies of voltage source type superconducting magnetic energy storage (SMES) under asymmetrical voltage. *Appl Supercond IEEE Trans* 12(1):750–753
18. Yuan W et al. (2010) Design and test of a superconducting magnetic energy storage (SMES) coil. *IEEE Trans Appl Supercond* 20(3):1379–1382
19. Zhu J et al. (2011) Simulation and experiment of a YBCO SMES prototype in voltage sag compensation. *Physica C*, 471(3):199–204

Chapter 7

Conclusions

7.1 Summary

This thesis has given an introduction to the background of the development of superconducting materials and their physical theory. It has also outlined SMES technology, including its history and the current status of research.

A complete optimisation algorithm was presented. This algorithm can calculate the design to achieve the maximum stored energy in a SMES system using the finite length of conductor available. This algorithm can be of assistance in the design of other SMES projects.

A new numerical model was investigated to predict the electromagnetic behaviour of a 2 G HTS pancake coil. This model is easy to compute without reducing its complexity in terms of the physical theory underlying the coil's properties. Important parameters such as the critical current and AC loss can be calculated by this model. More importantly, this model is also applicable to other 2 G HTS pancake coils. This will help the study of other devices, such as superconducting machines, transformers and fault current limiters.

Three superconducting coils were wound and comprehensive experiments of the basic coil characteristics were accomplished. Two different winding techniques are presented and compared. The experiments at 77 K have measured the critical current and AC losses of the coil. The experimental results are consistent with the numerical modelling results.

Finally, the control circuit of this prototype SMES system was studied. This control circuit managed to control the charge and discharge process of this SMES system. The simulation validated the control strategy. The prototype SMES system successfully compensated a voltage sag in a power system in the experiment.

7.2 Possible Improvements

This project can be potentially improved on the following aspects.

The SMES coil discussed in Chap. 4 can only store a small amount of energy, thus before the optimum design strategy is applied to a large SMES system, other issues such as the mechanical stability, leakage field and so on need to be considered.

The numerical model introduced in Chap. 5 only considered the perpendicular field to the superconducting tapes. For most engineering applications, this approximation will be accurate enough. However, there might be some new superconducting material without anisotropy appearing in market in future. In addition, top/bottom AC losses might be worth studying [1]. Therefore this model is worth being improved by considering the parallel magnetic field. Moreover, by introducing the parallel magnetic field into the model, the critical currents of the coils in the external field as shown in Chap. 6 can be calculated and compared with the experimental results.

Chapter 6 presented a poorly wound and jointed superconducting pancake coil. In comparison, several coils using a different winding and joining technique presented better performances. Thus the first winding and joining technique is not encouraged for making superconducting pancake coils in future. In addition, the AC loss measurement experimental set-up for coils cannot give the correct results since the signal is disturbed by the coupling effect between the coil and the dewar. To improve the set-up, the coil axis needs to be placed perpendicular to the dewar axis to maximumly reduce the coupling effect. Another AC loss measurement system using a compensation coil is designed and being built. The coils will be tested in the new system and compared with the numerical calculations.

This thesis only gave a relatively simple control strategy for SMES in Chap. 6, since this is not the major concern of this thesis. However, more delicated control strategy can be achieved by improving the converter design and circuit.

7.3 Future Look of SMES

Although the concept of 2 G HTS SMES systems has been validated and a laboratory prototype has been built, there is still much research to be carried out before they can be widely used in industrial applications. Several crucial problems need to be solved:

- The current price of 2 G HTS tapes is still cost prohibitive for the industrial application of SMES systems. A large SMES system has significantly more advantages than a small SMES system. The larger a SMES system is, the higher energy and power density it has compared to other energy storage systems. Among the large-scale energy storage systems, the response of a SMES is the

fastest. However, a large SMES system requires a significant amount of superconductors and the cost is too expensive based on the market price today.

- Joining methods of 2 G HTS tapes need to be improved. The 2 G HTS tapes' joint still has a comparatively large resistance. This resistance has caused great difficulties in building large SMES systems consisting of several superconducting coils. Moreover, it has significantly limited the maximum current a SMES system can carry and dissipates remarkable energy losses. Ideally the joint resistance of 2 G HTS tapes need to be reduced to $10^{-10} \Omega$ which is comparable to that of LTS conductors.
- The experiment results have showed that the relatively big coil, Coil 1, has a poor performance. However, small coils, Coils 2 and 3, have a much better performance. Although the difference can be explained by different winding techniques, whether the winding technique can be applied to large coils to achieve a good performance still needs to be studied.
- The capacity of the power electronic transistors, which are used within a SMES system, need to improve. The power electronic transistors are essential components in the control circuit of a SMES system since they have a fast response time and are able to carry large currents. However, future SMES systems for industrial applications require even larger power electronic transistors to sustain the operating current.

The most important advantages of a SMES system are, in comparison with other energy storage systems, the fast response time and large power density. Therefore the most promising industrial application of a SMES system is as an emergency power supply to protect critical loads of a power system, such as assembly lines in semiconductor factories, international media broadcasting centers or PC server clusters which cannot afford the loss of power supply or even a small voltage sag. Additionally, SMES systems are preferable candidates to provide a large pulse power for transportation and defence weapon systems.

Improving SMES design by reducing the impact of the aforementioned problems, SMES will become a crucial device in the protection of power systems and achieving a more secure energy supply. Furthermore, SMES technology will also open the door to new applications such as the delivery of large scale pulsed power. SMES systems, as a smart power grid-compatible technology, are set to become an integral part of the twenty first century power system.

Reference

1. Clem JR (2008) Field and current distributions and AC losses in a bifilar stack of strips. *Phys Rev B (Condensed Matter and Materials Physics)* 77(13):134506

Appendix A

Here we show that Eq. 5.9 of calculating losses can be used even if J_c is a function of B . We consider an external field B_0 applied to the face of a slab and first use the method of calculating the electric field from the change in flux.

First define a function $f(B)$ such that $\frac{1}{\mu_0}J_c = 1/f'(B)$, i.e. for the Kim model with $J_c = J_0/(1 + B/B_k)$, then,

$$f(B) = (B + 0.5B^2/B_k)J_0^{-1} \quad (\text{A.1})$$

B is given by the solution of

$$dx = f'(B)dB \quad (\text{A.2})$$

Also define f^{-1} , the inverse of f such that $f^{-1}f(B) = B$.

Then for a slab starting at $x = 0$ and extending to infinity in the positive direction, the critical state is given by $f(B) = f(B_0) - x$ where B_0 is the field at the surface. B is given by $B = f^{-1}(f(B_0) - x)$. The penetration of the field is to a distance x_0 where $x_0 = f(B_0) - f(0)$. Figure A.1 illustrates this.

The flux beyond a point x is

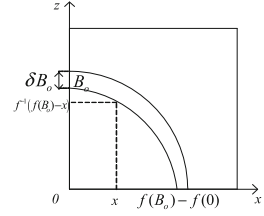
$$\phi(x) = \int_x^{x_0} f^{-1}(f(B_0) - y)dy \quad (\text{A.3})$$

To find the electric field we need the change in this with a change in B_0 . This is

$$\delta\phi(x) = \int_x^{x_0} f^{-1}(f(B_0) - y)dy f'(B_0)\delta B_0 \quad (\text{A.4})$$

where the dashes denote differentiation.

Fig. A.1 Critical state in a slab



Integrating with respect to y

$$\delta\phi(x) = -[f^{-1}(f(B_0) - y)]_x^{x_0} f'(B_0) \delta B_0 \quad (\text{A.5})$$

This is equal to

$$\delta\phi(x) = f^{-1}(f(B_0) - x) f'(B_0) \delta B_0 \quad (\text{A.6})$$

since at x_0 the integrand, B , is zero.

The local E is $d\phi/dt$ and the power loss is $E \cdot J_c$, so the local loss density in joules per unit volume is

$$\delta Q(x) = \frac{f^{-1}(f(B_0) - y) f'(B_0) \delta B_0}{\mu_0 f'(f^{-1}(f(B_0) - x))}. \quad (\text{A.7})$$

The total loss per unit area on the $y - z$ face of the slab at a field B_0 is

$$\delta Q(B_0) = f'(B_0) \int_0^{x_0} \frac{f^{-1}(f(B_0) - y) f'(B_0) \delta B_0}{\mu_0 f'(f^{-1}(f(B_0) - x))} dx \delta B_0 \quad (\text{A.8})$$

$$\delta Q(B_0) = f'(B_0) \int_0^{x_0} \frac{f^{-1}(f(B_0) - y) f'(B_0) \delta B_0}{\mu_0 f'(f^{-1}(f(B_0) - x))} dx \delta B_0. \quad (\text{A.9})$$

Now put $z = f(B_0) - x$,

$$\delta Q(B_0) = -f'(B_0) \int_{f(B_0)}^{f(0)} \frac{f^{-1}z}{\mu_0 f'(f^{-1}z)} dz \delta B_0 \quad (\text{A.10})$$

and then put $B = f^{-1}(z)$ so $z = f(B)$ and $dz = f'(B)dB = f'(f^{-1}(z))dz$. Then

$$\delta Q(B_0) = \mu_0^{-1} f'(B_0) \times 0.5 B_0^2 \delta B_0. \quad (\text{A.11})$$

Hence the total loss in joules per unit area on the $y - z$ face of the slab on raising the external field from zero to B_m can be written

$$Loss = \frac{1}{2\mu_0^2} \int_0^{B_m} \frac{B^2}{J_c(B)} dB \quad (\text{A.12})$$

50 We now show that Eq. 5.9 gives the same result.

52 The loss based on the flux line force is:

$$\int_0^{f(B_m)-f(0)} \frac{x f^{-1}(f(B_m) - x)}{\mu_0 f'(f^{-1}(f(B_m) - x))} dx \quad (\text{A.13})$$

54 Put $z = f(B_m) - x$,

$$Loss = \int_{f(0)}^{f(B_m)} \frac{(f(B_m) - z) f^{-1}(z)}{\mu_0 f'(f^{-1}(z))} dz \quad (\text{A.14})$$

58 as before put $B = f^{-1}(z)$ so $z = f(B)$ and $dz = f'(B)dB = f'(f^{-1}(z))dB$.

$$Loss = \mu_0^{-1} \int_0^{B_m} (f(B_m) - f(B)) B dB \quad (\text{A.15})$$

60 On the other hand,

$$\begin{aligned} Loss &= \frac{1}{2\mu_0} \int_0^{B_m} B^2 f'(B) dB \\ &= \frac{1}{2\mu_0} \int_0^{B_m} B^2 df(B) \\ &= \frac{1}{2\mu_0} \left(B_m^2 f(B_m) - \int_0^{B_m} f(B) 2B dB \right) \end{aligned} \quad (\text{A.16})$$

$$= 0.5 \mu_0^{-1} B_m^2 f(B_m) - \mu_0^{-1} \int_0^{B_m} B f(B) dB \quad (\text{A.17})$$

66 The last step in Eq. A.17 can be shown to be true if the last line is integrated by
67 parts, leading to the third line in Eq. A.16.

68